DRYOUT LIMITS IN HORIZONTAL ANNULAR FLOW

by

Aaron G. Flores

B. S. M. E., MIT (1991)

Submitted to the Department of

Mechanical Engineering

in Partial Fulfillment of the Requirements for the

Degree of Master of Science

at the

MASSACHUSETTS INSTITUTE OF TECHNOLOGY

June, 1992

Signature of Author.....

Department of Mechanical Engineering May 1992

Certified by..... .....

Peter Griffith

Professor

Thesis Supervisor

Accepted by.....

Ain Sonin

Chairman, Departmental Committee on Graduate Students

DRYOUT LIMITS IN HORIZONTAL ANNULAR FLOW

by

Aaron G. Flores

Submitted to the Department of Mechanical Engineering
in Partial Fulfillment of the Requirements for
the Degree of Master of Science in
Mechanical Engineering

Abstract

Experiments were performed and semi-empirical correlations were derived in order to investigate the film dryout limits in horizontal annular two-phase flow. As a result of this research, secondary flow, consisting of two counter-rotating vortices, was discovered to be the major factor controlling dryout. Through experiments, the dominant parameter determining the strength of the secondary flow in this system was found to be the difference in effective roughness between the upper and lower portions of the tube. The secondary flow phenomenon was reproduced in an experimental, single phase system consisting of a 2" diameter tube with a smooth upper and sand roughened lower half. Secondary flow measurements were made for several roughnesses as a function of throughput velocities. A single phase model of the film was combined with the secondary flow correlations, and dryout boundaries were formulated and compared to experimental data.

Thesis Supervisor: Dr. Peter Griffith
Title: Professor of Mechanical Engineering

Acknowledgments:

Many have given technical advice and support in the duration of this project. I would like to offer my appreciation to the following individuals, my thesis advisor Prof. Peter Griffith, Keith Crowe, and "Tiny" Caloggero. For their constant personal support and encouragement, I would like to thank Valerie, my mother and my father.

Table of Contents

Table of Contents (cont.)

List of Figures

List of Figures (cont.)

List of Figures (cont.)

List of Symbols

C_f = Friction Factor

D = Tube Diameter (m)

δ = Film Thickness in the Tube's Top Half (m)

δ_{av} = Circumferentially Averaged Film Thickness (m)

ε = Roughness Height (m)

f = Friction Factor

g = Gravity (m / s^2)

h_{fg} = Latent Heat (kJ / kg)

P = Pressure (Pa)

ΔP = Differential Pressure between Tube's Top and Bottom (Pa)

ρ = Density (kg / m^3)

ρ_f = Density of Liquid (kg / m^3)

ρ_g = Density of Gas (kg / m^3)

q" = Heat Flux (kW / m^2)

Q' = Vertical Film Flux Up Tube's Walls (m^2 / s)

σ = Surface Tension (N / m)

θ = Angle (degrees)

R = Tube's Radius (m)

τ = Shear (Pa)

τ_s = Secondary Shear of Gas on Liquid (Pa)

τ_w = Axial Shear at the Tube's Wall (Pa)

u * = Turbulent Friction Velocity (m / s)

$\bar{u}(y)$ = Mean Velocity Distribution (m / s)

μ_f = Fluid Viscosity (kg - m / s)

List of Symbols (cont.)

V = Velocity (m / s)

V_g = Gas Velocity ≈ Gas Superficial Velocity (m / s)

V_f = Fluid Superficial Velocity (m / s)

V_s = Secondary Velocity in the Gas Core (m / s)

ω = Angular Velocity of Rotors (rad / s)

y^* = Turbulent Viscous Layer (m)

$1 - \alpha$ = Liquid Void Fraction

Chapter 1

Introduction

Two-phase fluid flows appear in a number of forms including gas-solid, liquid-liquid, solid-liquid, and gas-liquid flows. These flows exist in applications varying from waste treatment facilities to nuclear power plants. The understanding of the two-phase flow phenomena is, thus, extraordinarily important when considering the number of applications and capital involved when these flows are present. However, in contrast to the needs, the large amount of work, and the effort in these areas, the current models and correlations for two-phase flows lend themselves to only a limited number of design applications. More specifically, in many gas-liquid flow situations, designers must employ costly experimental methods instead of analytical models. The reason for the lack of a reliable theory emerges when one considers the complexity of two-phase and in many cases, turbulent flows. Some would argue that satisfactory single-phase turbulent flow models have not been developed, let alone two-phase turbulence (Hewitt & Taylor p.1). With regard to the problem under consideration, both theoretical and experimental investigations must be performed to understand this two-phase flow.

In each type of two-phase flow, several different regimes or flow patterns exist. Flow patterns represent the distribution of the two phases in a given cross-section of tubing. More specifically, in horizontal gas-liquid flows, six different regimes exist: bubbly, plug, stratified, wavy, slug, and annular (see Figure 1-1). Bubbly flow can be identified by gas bubbles in the upper half of the tube immersed in a moving liquid. Plug flow contains larger gas bubbles, or plugs, which have an asymmetric head traveling on

the upper half of the tube between areas of total liquid flow. Stratified flow occurs when the gas travels on the upper portion of the tube and liquid on the bottom portion with no mixing between the two phases. When the gas velocity is increased past a certain value in a stratified flow, large surface waves appear on the liquid interface and the pattern becomes a wavy, stratified flow. As the gas velocity is further increased, the flow pattern shifts to slug flow where the liquid waves enlarge so much that the entire cross-section can be wet due to passing waves. Lastly, as the gas velocity is further increased, the slug pattern gives way to an annular flow. Annular flow is characterized by a gas core surrounded by a liquid film on the walls of the tube. Due to gravity, the liquid film is thicker on the lower portion of the tube. The location of a particular regime is usually defined on a map in which the coordinates are the superficial gas and liquid velocities (Hewitt & Taylor pp.6-7).

Although several analytical models exist for predicting gas-liquid flow regimes in vertical tubes, few exist for horizontal flow. The asymmetry caused by gravity makes theoretical models in horizontal flows much more complex than the symmetric vertical flows. Each regime also contains different characteristics such as friction factors, heat transfer coefficients, and pressure gradients. Annular flow is perhaps the most complex pattern to predict but is also one of the most important. For instance, annular flow has a much higher heat transfer coefficient than does the surrounding wavy regime (Pitts & Donald p.221). For many two-phase flow applications, it is important to stay within certain regimes in order to avoid overheating, material fatigue, and equipment failure. At the present time, very few reliable models exist to aid the designer in predicting the various flow regimes and dryout boundaries in horizontal, two-phase flows.

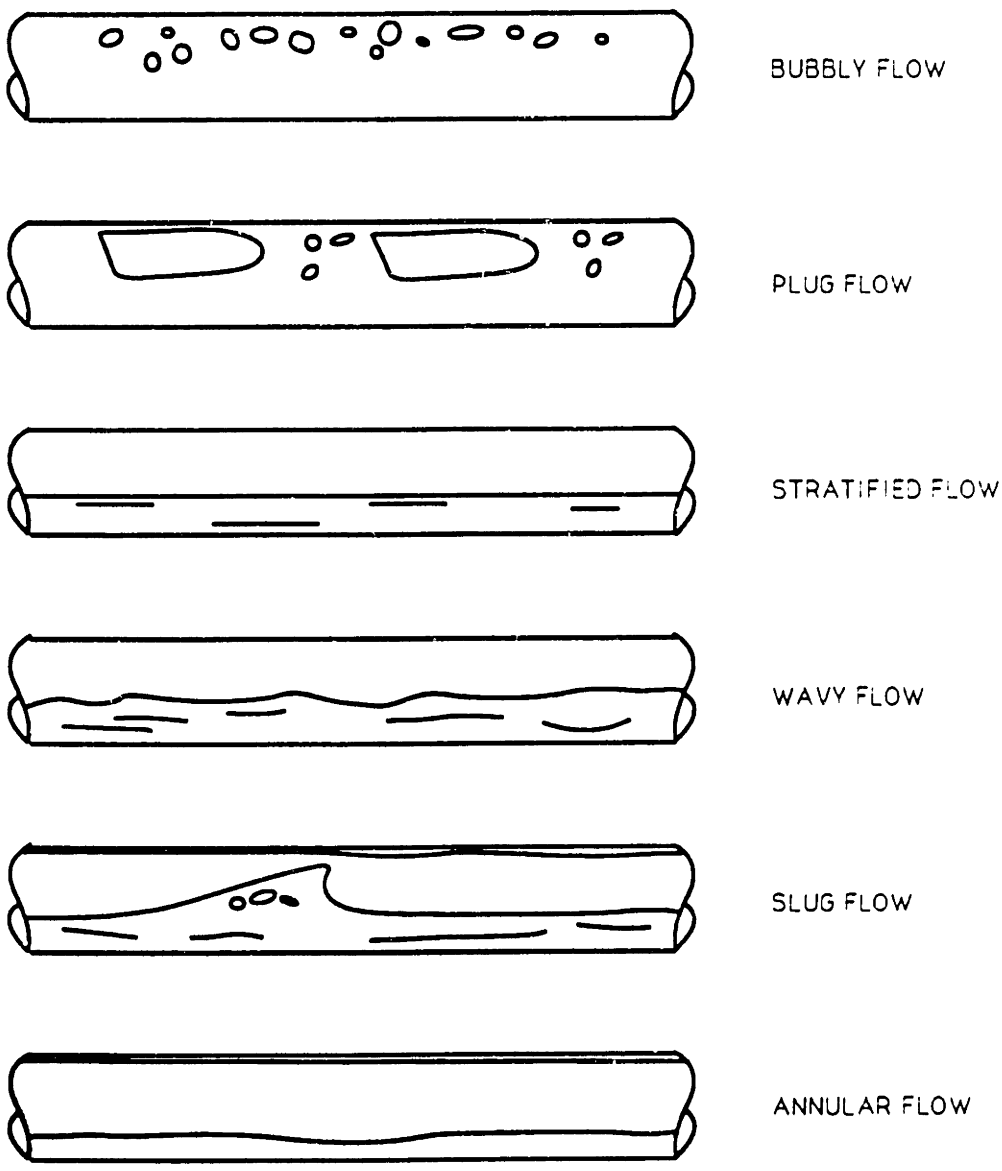

Figure 1-1: Flow Patterns in Horizontal Gas-Liquid Flow

Horizontal annular flow is extremely important in many applications including those of the energy industry where critical design specifications are required. Horizontal or approximately horizontal tubes are essential components of fluidized bed combusters and many kinds of waste heat, heat exchangers. One major design limitation is the high quality tube dryout which occurs in annular flow. It starts at the top of the tube and gradually propagates around it until most of the top half of the tube is dry. This leads to overheating, thermal cycling, tube erosion, and ultimately, tube failure(Butterworth p.235).

The goal of this project is to improve our understanding of dryout in horizontal tubes so that the effects of pressure, diameter, and non-uniform heat flux around the tube can be considered. Several air-water experiments were performed in both two-phase and single phase flows in a 2 in. pipe. The methods and configurations that were employed, in order to better understand the physical mechanism of high quality annular dryout, are described in this thesis.

Chapter 2

Dryout

The high quality dryout limit in horizontal annular flow is defined as the point where the liquid annulus is no longer maintained on the top of the tube's cross-section. On a flow regime map these points fall near the stratified/annular flow regime boundary. At this boundary, the tube's walls no longer maintain a liquid film and the flow falls into the stratified-wavy regime where the liquid and gas are distinctly separated in the bottom and upper portions of the tube. This limit can be reached from an initially wet tube wall by decreasing the gas or liquid flowrate below a critical value. In a heated environment, a high heat flux may also evaporate a portion of the film, inducing an earlier dryout limit than would be seen in an adiabatic system. In the following investigation, adiabatic experiments were executed to separate the purely fluid dynamic mechanisms of dryout from those also affected by heat transfer.

At very high qualities within the annular flow regime another dryout boundary exists. This boundary represents the point at which the shear of the gas on the liquid causes the liquid film to break up and travel on the tube's walls in rivulets. This type of flow also denotes a high quality dryout boundary in horizontal tubes. However, this investigation focuses on the stratified/annular dryout boundary and should not be confused with the dryout boundary of rivulet flow.

Dryout Experiment

With these considerations, an atmospheric pressure, air-water, horizontal test rig was designed and constructed (see Figure 2-1). Two inch tubing was specified because of its closeness in size to the average boiler tube. The test section consisted of a 10' length of clear PVC tubing discharging into a drain at atmospheric pressure. The inlet configuration was designed to create an initial annular flow in the two-phase system (see Figure 2-2). Tap water was fed into system via a calibrated, variable area Brooks Instrument liquid flowmeter. Water entered from both the top and bottom of the tube and was forced through a circumferential gap. Air entered the inlet through the center of the tube's cross-section from a near atmospheric compressor and was immediately surrounded by the liquid annulus. The air's inlet tube was tapered outwards at approximately six degrees to avoid separation at its entrance into the system. Air flow rates were measured in the absence of the water by a pitot probe and manometer which were located at the exit of the tube.

Dryout limits were then observed in a range of liquid and air flowrates. A two foot tube section located one foot from the exit was selected as the observation region. This location was chosen to help insure the flow was fully-developed in the system while also minimizing any exit phenomena that might affect the flow pattern. The system's superficial air and water velocities ranged from 0 - 30 m/s and .01 to 1 m/s respectively. Dryout measurements were made by first putting the system into an annular flow where the entire tube's cross-section maintained a liquid film and then slowly decreasing the liquid flowrate until the top of the wall went dry in the observation area. Thus, for each air flowrate a liquid flowrate at which dryout appeared was found.

In the previously described experimental scheme, dryout points were found in the full range of possible flow rates. The dryout limits were plotted on air - water superficial

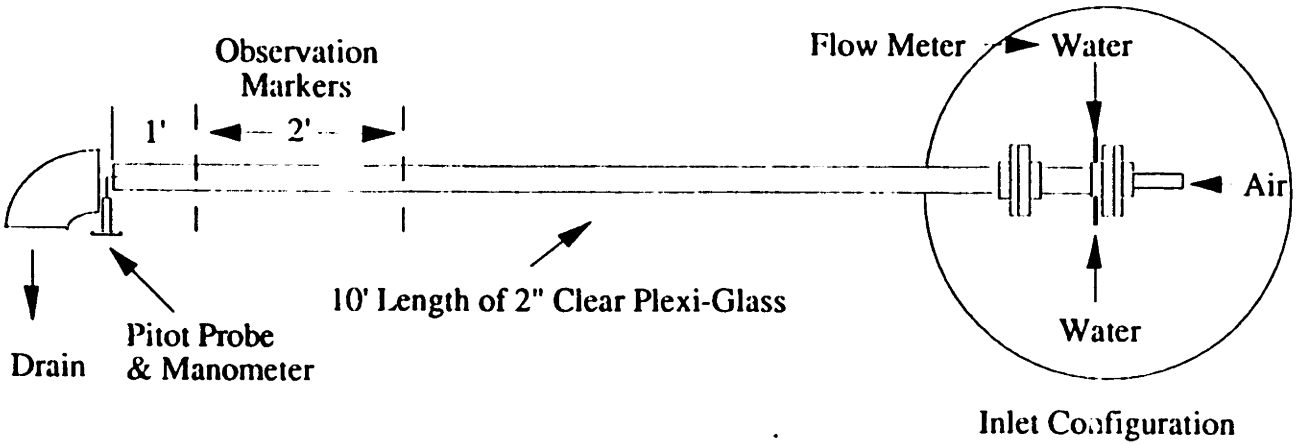

Figure 2-1: Experimental Set-Up

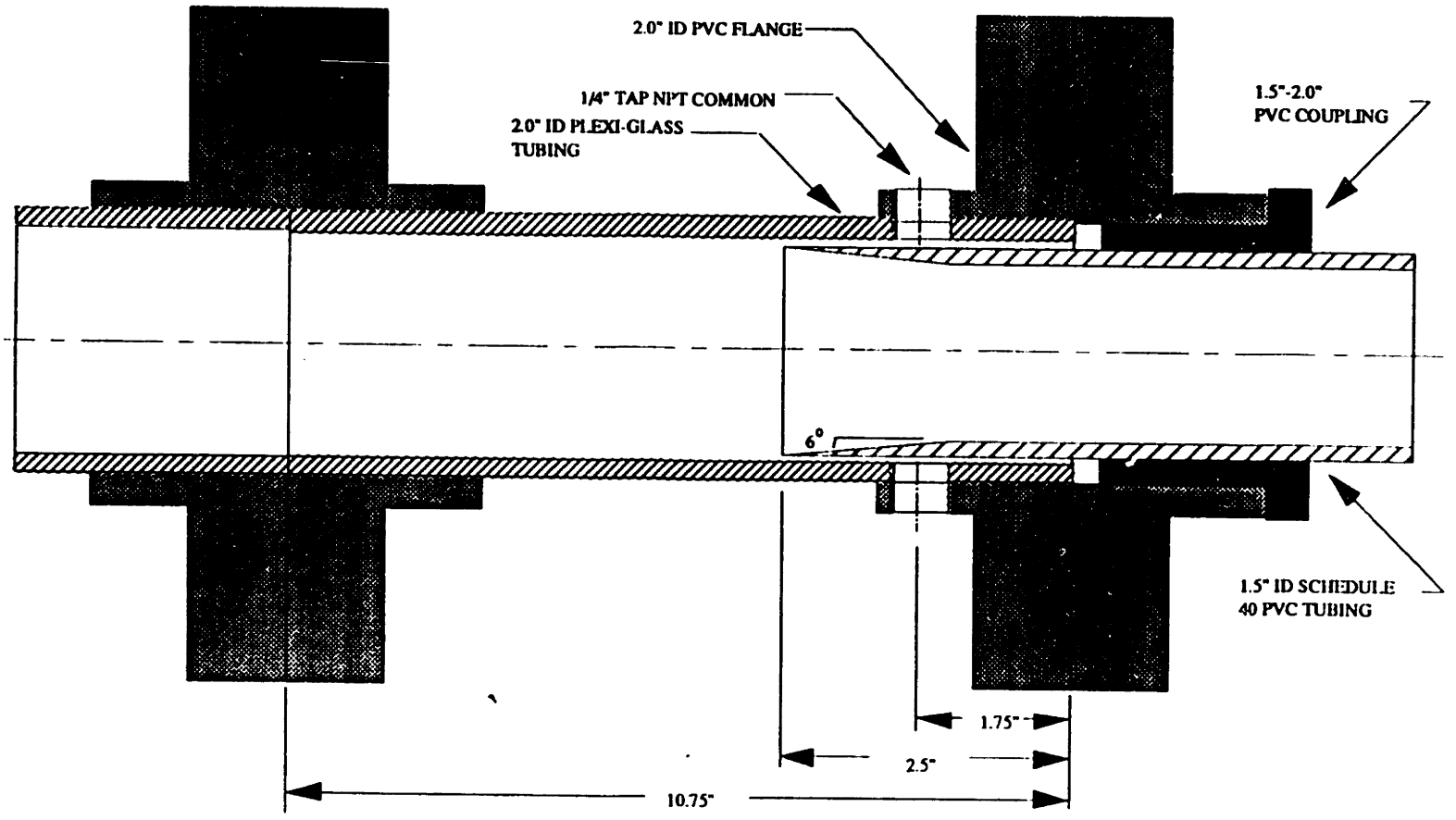

Figure 2-2: Inlet Configuration

velocity coordinates along with Mandhane's and Laurinat's experimental limits as well as Taitel and Dukler's theoretical boundaries for 2" tubes (see Figure 2-3) (Mandhane p.537)(Laurinat p.93)(Dukler & Taitel p.47).

The dryout limit from the present experiment falls to the right of both Mandhane's and Taitel and Dukler's stratified/annular flow boundaries by a small increment, but is very close to the limit given by Laurinat. This discrepancy, although not large, was probably due to the authors' different interpretations of annular flow. The dryout limit found in this experiment, as mentioned earlier, was discovered through visual wetting criteria at the point where the top cross-section of the tube no longer maintained a liquid annulus. Despite the small differences between the various limits, the theories and all the measurements behaved in essentially the same way.

There are several possible mechanisms which may control dryout in annular flow. Without some type of force holding the liquid on the tube's wall's or constantly replenishing the film, gravity would force the annular pattern into stratified flow. Several authors have suggested possible mechanisms for maintaining the thin film on the tube's upper cross-section. These include entrainment/ deposition, wave spreading and pumping, and secondary flow.

The entrainment / deposition theory suggests that a percentage of liquid droplets is entrained or picked up from the bottom half of the tube and deposited on the upper half of the tube. Thus, a constant replenishing of the film occurs from the bottom to the top of the tube.

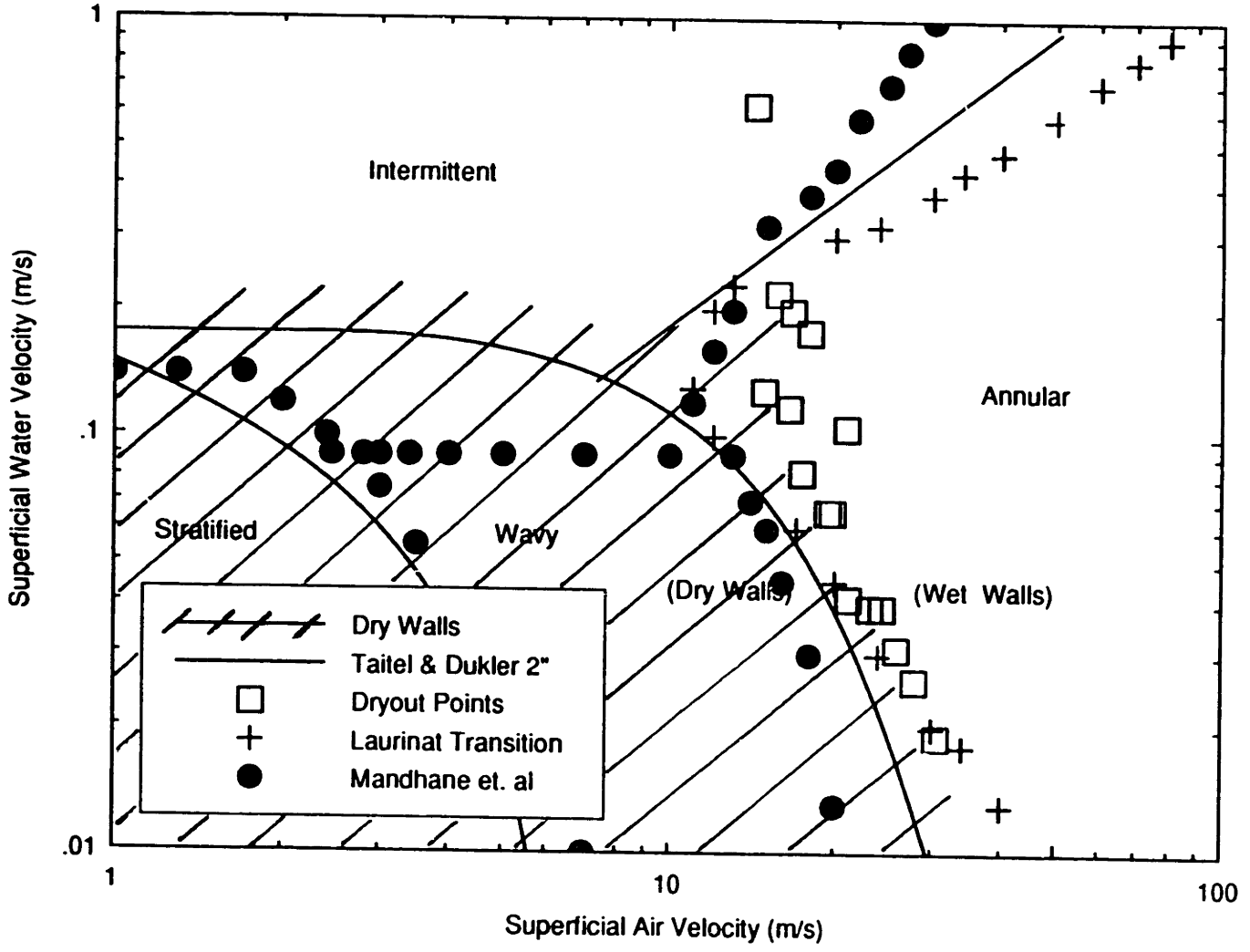

Figure 2-3: Adiabatic Dryout Boundary in .0508m Diameter Tube

In the wave spreading idea, the film is maintained by waves induced on the bottom half of the tube traveling to the top of the tube where the flow is much lower. The wave spreading mechanism is comprised of several different hypotheses including wave pumping, wave curvatures, and hydrostatic pressure differences.

Lastly , in the secondary flow model, a circumferential variation in roughness and shape factors within the tube's cross-section gives rise to a secondary flow in gas core that lifts the film up the tube's walls. The remainder of this investigation will separately cover each theory in an attempt to reveal which mechanism is dominant near the dryout limit.

Chapter 3

Entrainment/Deposition

Net entrainment from the bottom half and net deposition on the top half of the tube's cross-section is, historically, one of the many mechanisms thought to maintain the film and its distribution around a tube's periphery in annular flow. Many investigators have looked at this mechanism in detail and their major points and conclusions will be briefly reviewed. In light of these facts the entrainment/deposition mechanism's significance with respect to dryout will be discussed.

Entrainment is a common occurrence in two-phase flows. When two fluids are traveling in a channel their relative velocity gives rise to shear (see Figure 3-1). More specifically, in horizontal gas-fluid flows, the shear causes waves to form in the pool of liquid in the bottom of the tube. As the waves grow larger, the crests reach a critical point. This critical state occurs when the wave juts into the gas high enough that the drag, which is dependent on the gas's axial velocity, shears off the wave's crest forming a spray of liquid droplets. The droplets remain entrained in the lighter fluid until they are deposited back to the liquid film or expelled from the tube (Hewitt & Taylor pp.136-141).

The onset of entrainment has been correlated through many experiments. Steen (1964) suggests the following correlation:

$$\frac{V_g \mu_g}{\sigma}\left(\frac{\rho_g}{\rho_f}\right)^{1/2} \geq 2.46\text{x}10^{-4} \qquad (3\text{-}1)$$

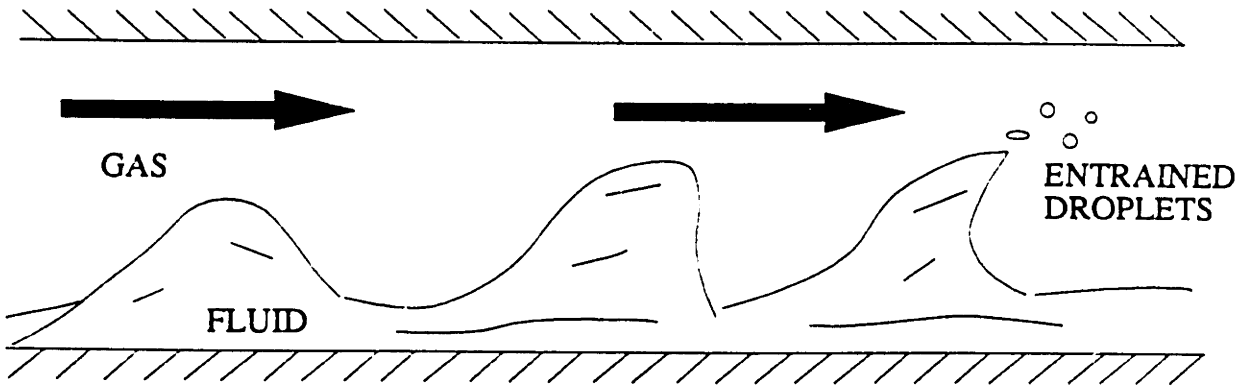

Figure 3-1: Entrainment Mechanism

for the onset of entrainment. It was later suggested the constant, 2.46, on the right hand side be changed to 1.5 (Collier p.84). In the present air -water system eq.(3-1) gives a gas velocity for the onset of entrainment to occur at approximately 36m/s. Collier's value for the constant in eq.(3-1) gives a critical gas velocity of approximately 22 m/s for the onset of entrainment. Hewitt later places the onset of entrainment in air-water flow to occur at approximately 18m/s (Hewitt & Taylor p.143). Regardless of which value one chooses, the onset of entrainment occurs in the center of the dryout limit (See Figure 2- 3). Therefore, the entrainment/deposition mechanism can only effect dryout in a portion of the dryout boundary. To measure its relative effect in this region, experimental data must be analyzed.

After the onset of entrainment has been reached, one can deduce more about the entrainment/deposition mechanism's effect on the liquid film by exploring the experimental evidence. For instance, since a greater amount of fluid travels in the lower portion of the tube, it follows that there might be liquid transported by entrainment from the bottom half to the top half of the tube. Experiments verify this happened, but give experimental values for entrainment that are only 10% of the magnitude required to support a film in annular flow on the top half of the tube (Butterworth p.247). Thus, after the onset of entrainment has been reached, the mechanism contributes very little toward maintaining a liquid annulus on the tube's walls. Experiments have also shown that, in high quality annular flows, gravity becomes less important giving rise to a flow situation in which little or no net entrainment or deposition from bottom to top exists (Hewitt & Taylor pp.74-75).

The present experimental results point toward the fact that the entrainment/deposition mechanism plays a small part in setting the dryout limit in annular

flow. At the lower quality dryout limit, in particular, the entrainment velocity has not yet been reached, and is therefore, totally eliminated as a possible mechanism. Experimental data also shows that the amounts of entrainment and deposition are an order of magnitude smaller than required to support the liquid films alone. At the other extreme, the very high quality dryout limit gives an almost symmetrical annular flow where net deposition and entrainment values are even smaller. Although this mechanism does not seem to control dryout, experimental evidence points towards its affecting circumferential film thicknesses beyond the entrainment limit.

Chapter 4

Literature Review of Wave Liquid Transport Mechanisms

There are two types of wave phenomena which may account for bringing fluid to the tube's top near dryout. These mechanisms are known as wave spreading and wave pumping. A literature review and experiments were carried out to study the significance of these mechanisms near dryout. The relevant features of both the literature and experiments are then discussed with respect to dryout.

One type of wave spreading is caused by larger waves being formed in the middle of the tube's cross-section due to shear from the gas flow (see Figure 4-1). The waves in the tube's middle then have a greater hydrostatic head than the fluid at the same vertical position at the tube's sides. This discontinuity in pressure causes a circumferential flux of fluid up the sides of the tube (Butterworth & Pulling p.11).

The second form of wave spreading is caused by the curvature of the waves. As the waves travel axially down the tube, the center of the wave protrudes ahead of the portions near the tube's walls. Since waves travel normal to their fronts, the curvature gives rise to a circumferential flux up the walls of the tube (see Figure 4-1)(Butterworth and Pulling p.12).

The pumping of disturbance waves is caused by pressure gradients in the gas . The liquid film is thought to consist of a base film and disturbance waves. Due to pressure

differences between the waves' front and back, the disturbance waves move axially down the tube. The waves' heights are higher at the bottom and decrease toward the top of the tube, creating a static pressure gradient behind each wave height. Due to the circumferential wave height differences, a negative pressure gradient forms in the circumferential direction. This pressure gradient tends to suck liquid up the tube's walls (see Figure 4-2)(Fukano & Ousaka pp.405-407).

Hewitt also studied wave and film behavior as a function of time in order to further explore the wave mechanisms. Wave frequencies were measured in different qualities within annular flow. At low gas flow rates or qualities within annular flow (which accounts for a large portion of our dryout region) disturbance waves were discovered to be absent in the upper half (past 90 degrees) of the tube. In other words, the tube's upper perimeter experiences only an occasional wave, which is most likely due to the wave spreading mechanism. However, as the gas flow rate is increased, the disturbance waves appear higher up the walls of the tube. At very high qualities, the waves are circumferentially coherent as they travel axially down the tube. Hewitt's experiments also showed that waves all the way around the tube's circumference travel at approximately the same speed (Hewitt, Jayanti, & White pp.1097-1116).

Dye Experiment

A series of dye experiments were performed in an attempt to capture visual proof of the near dryout wave mechanisms in the liquid film. The dryout set-up was also used on the dye experiment with the addition of a dye injector (see Figure 4-3). The dye injector was similar to the one used by Butterworth (Butterworth & Pulling p.15). The dye used was potassium permanganate. A .1" diameter glass tube was inserted into a 1"

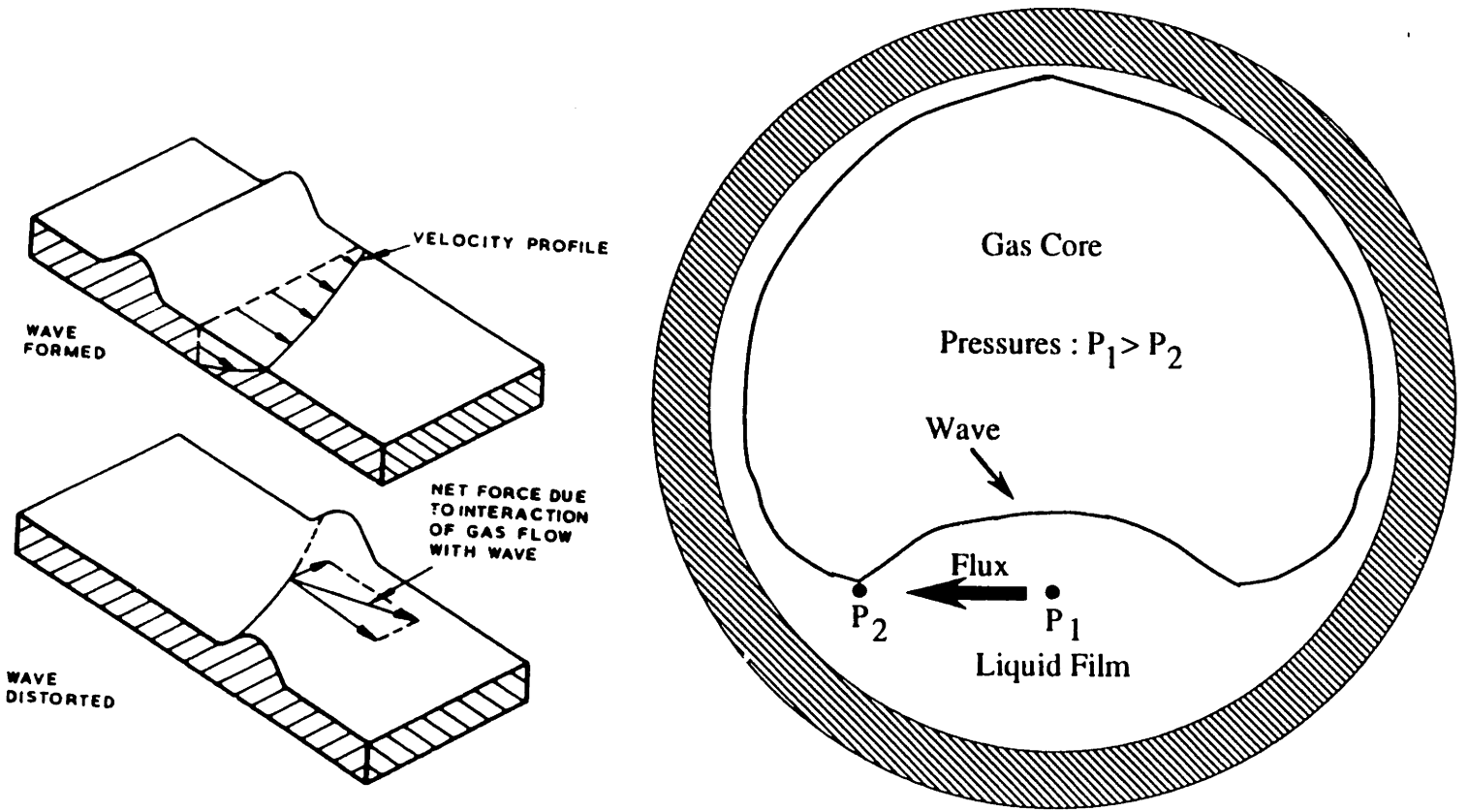

Figure 4-1: Wave Spreading Mechanisms

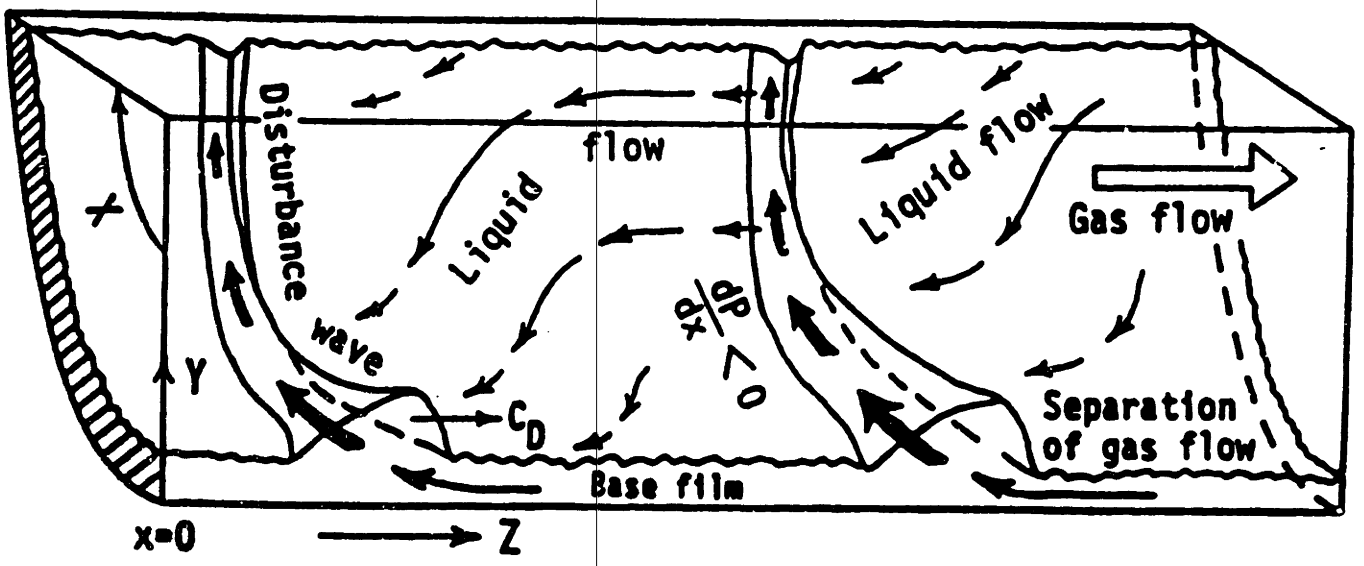

Figure 4-2: Pumping Action of Disturbance Waves

by 1" by 1" clear plastic holder which was then mounted on the tube. The tube contained a .036" hole through which the dye was injected into the liquid film. The dye's flow rate was controlled by a small valve which sat below a large container of dye solution several feet above the tube. The system was brought to the desired flow state and the dye was injected into the film. Careful control of the dye's flow permitted injection only into the film. By rotating the tube, the angle at which the dye was injected relative to the vertical axis was also varied throughout the upper half of the cross-section. Once the dye and flow were regulated to the desired steady state, pictures were taken. A 35mm camera was used along with black and white film at shutter speeds of 1/500-1/2000 of a sec. Several pictures were taken near and past the dryout limits and are shown in Figure 4-4 through 4-8. Interestingly, many of the pictures were taken on the dryout limit and can be distinguished by small dryout patches in the film.

The photographs display several important and common characteristics (see Figure 4-4). All the different injection angles showed almost instant circumferential mixing of the liquid film. The circumferential mixing leaves the injection point at angles that widen as gas flowrates increase. The majority of the dye solution travels toward the tube's bottom. However, some of the solution travels slightly upwards and remains at the same vertical location for several diameters downstream . Only in two instances were wave spreading effects witnessed. These two cases both occurred below the entrainment limit and at very high liquid flowrates (see Figure 4-8). Small waves are visible in the liquid film that appear to be traveling at the same velocity and wavelength throughout the entire upper half of the tube (see Figure 4-4-4-8). The distance between the waves shortens as the gas velocity is increased. Many of the pictures display a horizontal line in the middle of the tube. This line is due to a reflection of light when the photographs were

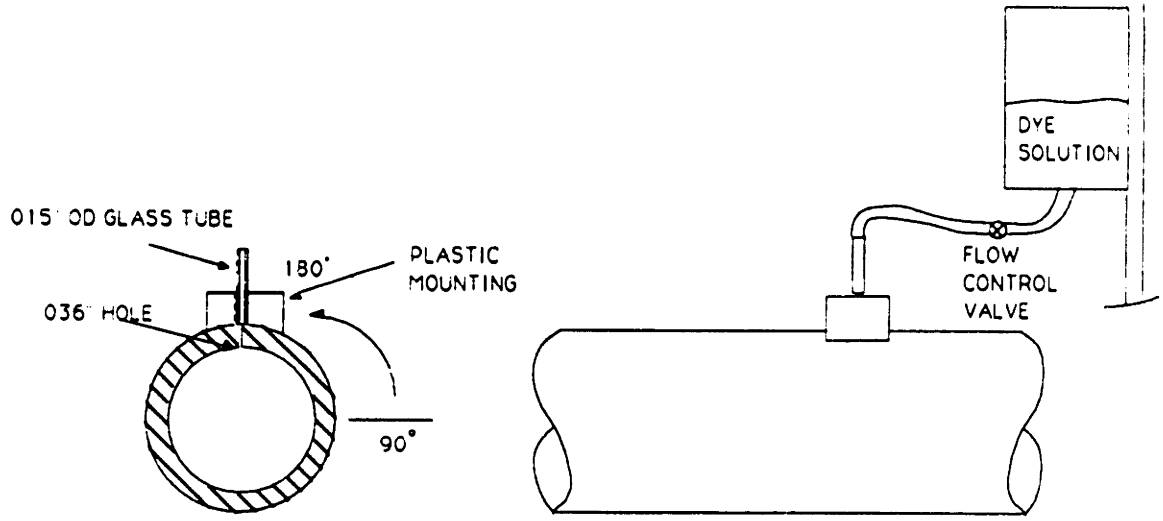

Figure 4-3 : Dye Injector Set-up

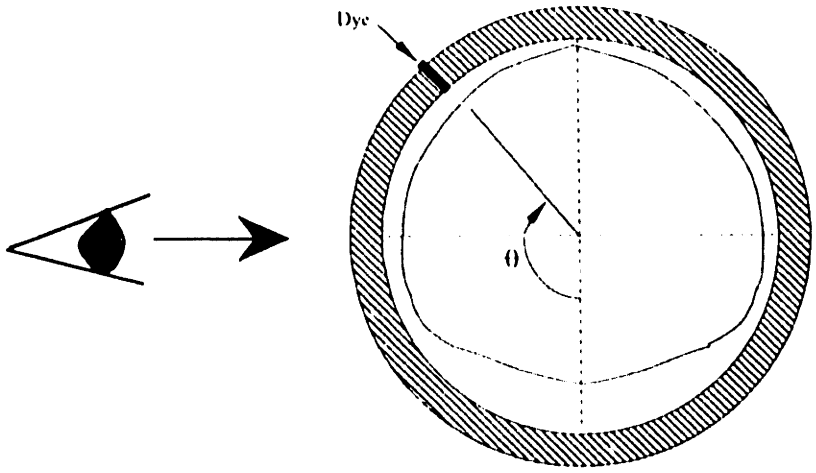

Viewing Position/Injection Angle Relationship

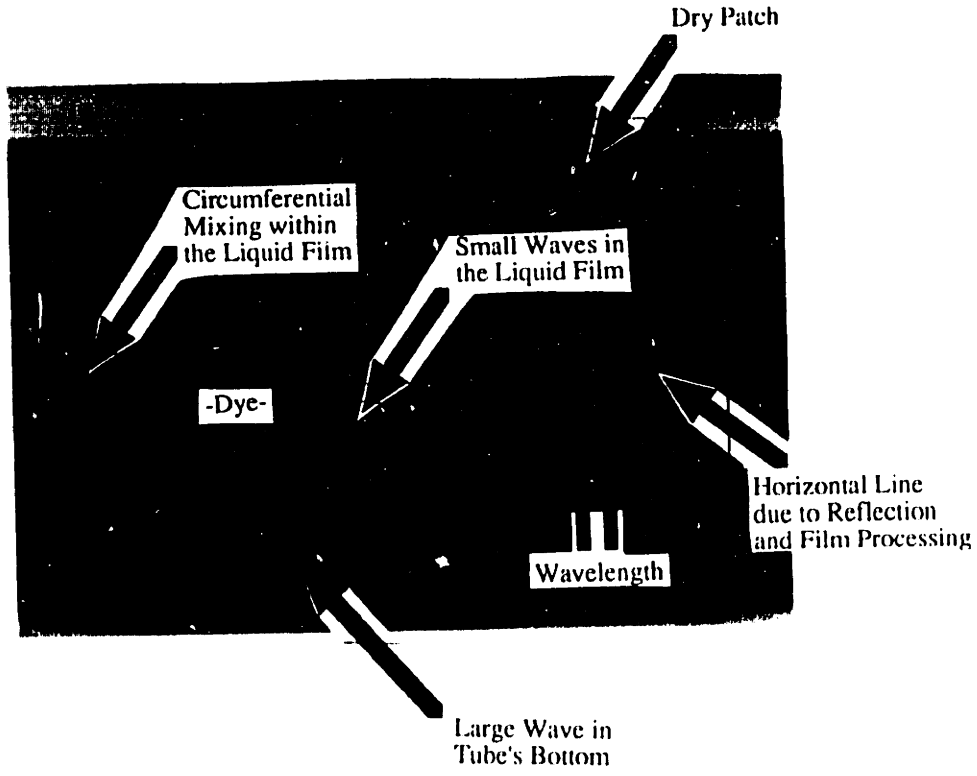

Important Film/Picture Characteristics

Figure 4-4: Dye Experimental Results

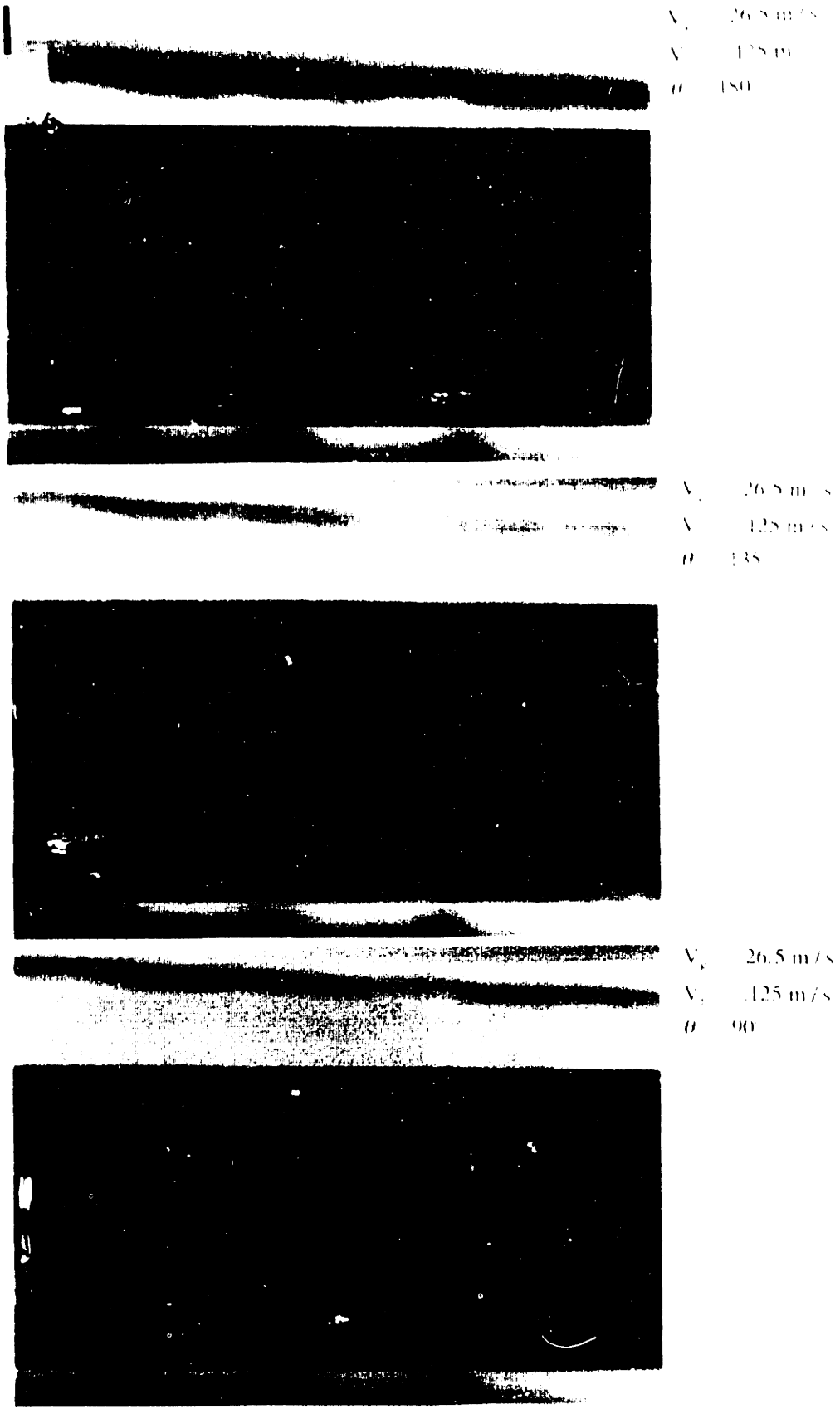

Figure 4.5: Dye Experimental Results

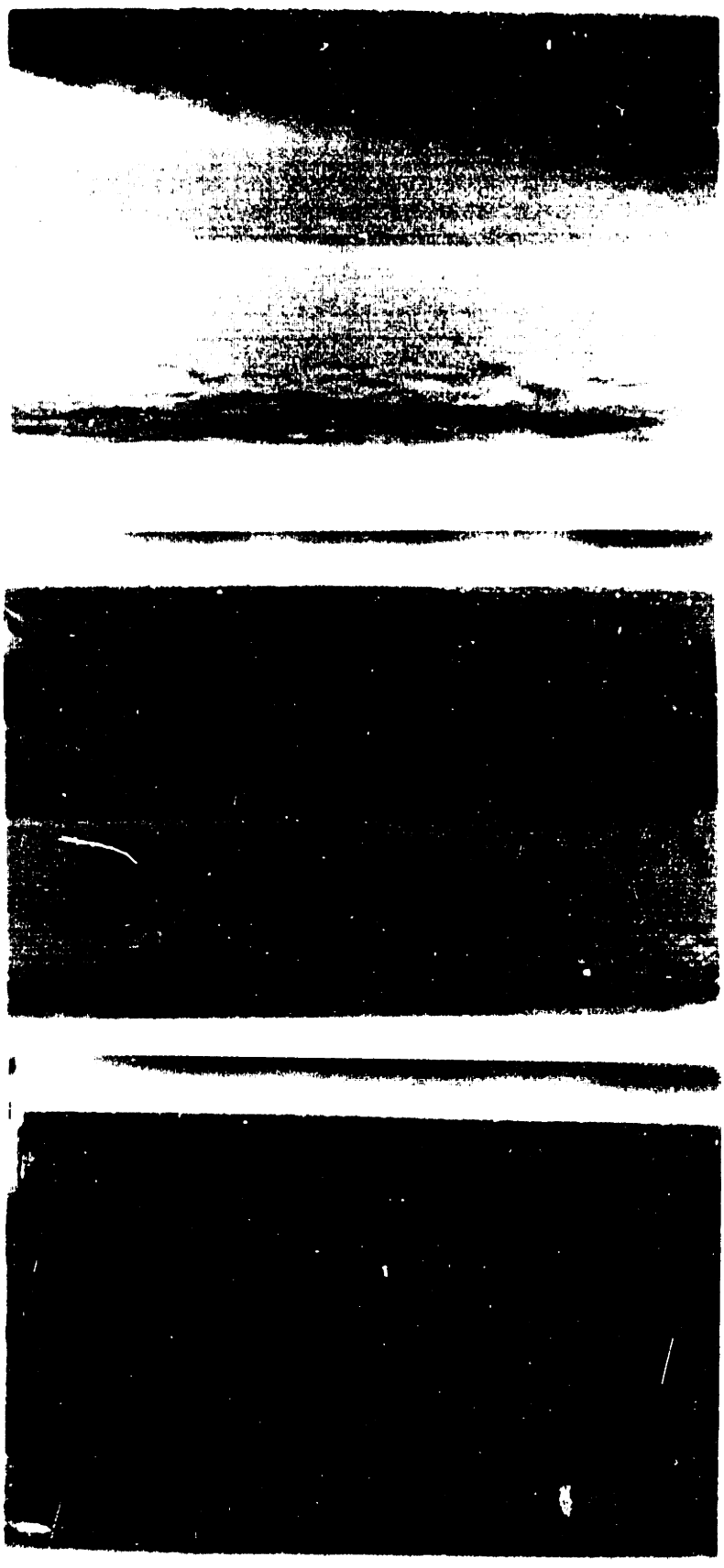

Figure 4.6 Dye Experimental Results

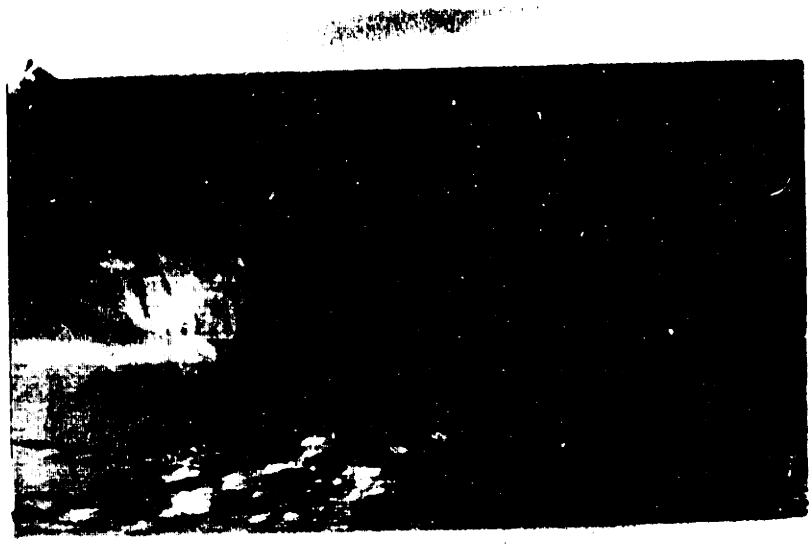

V_g = 31.5 m / s
V_f = .016 m / s
θ = 180°

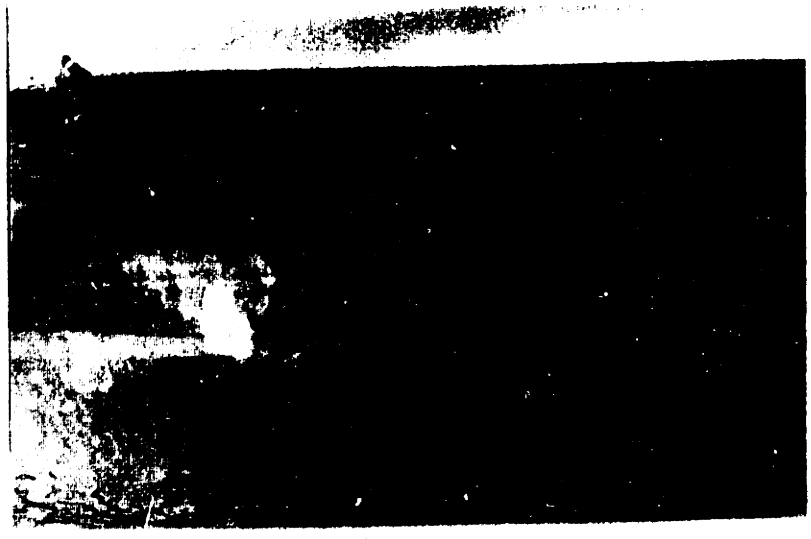

V_g = 35.0 m / s
V_f = .030 m / s
θ = 180°

Figure 4-7: Dye Experimental Results

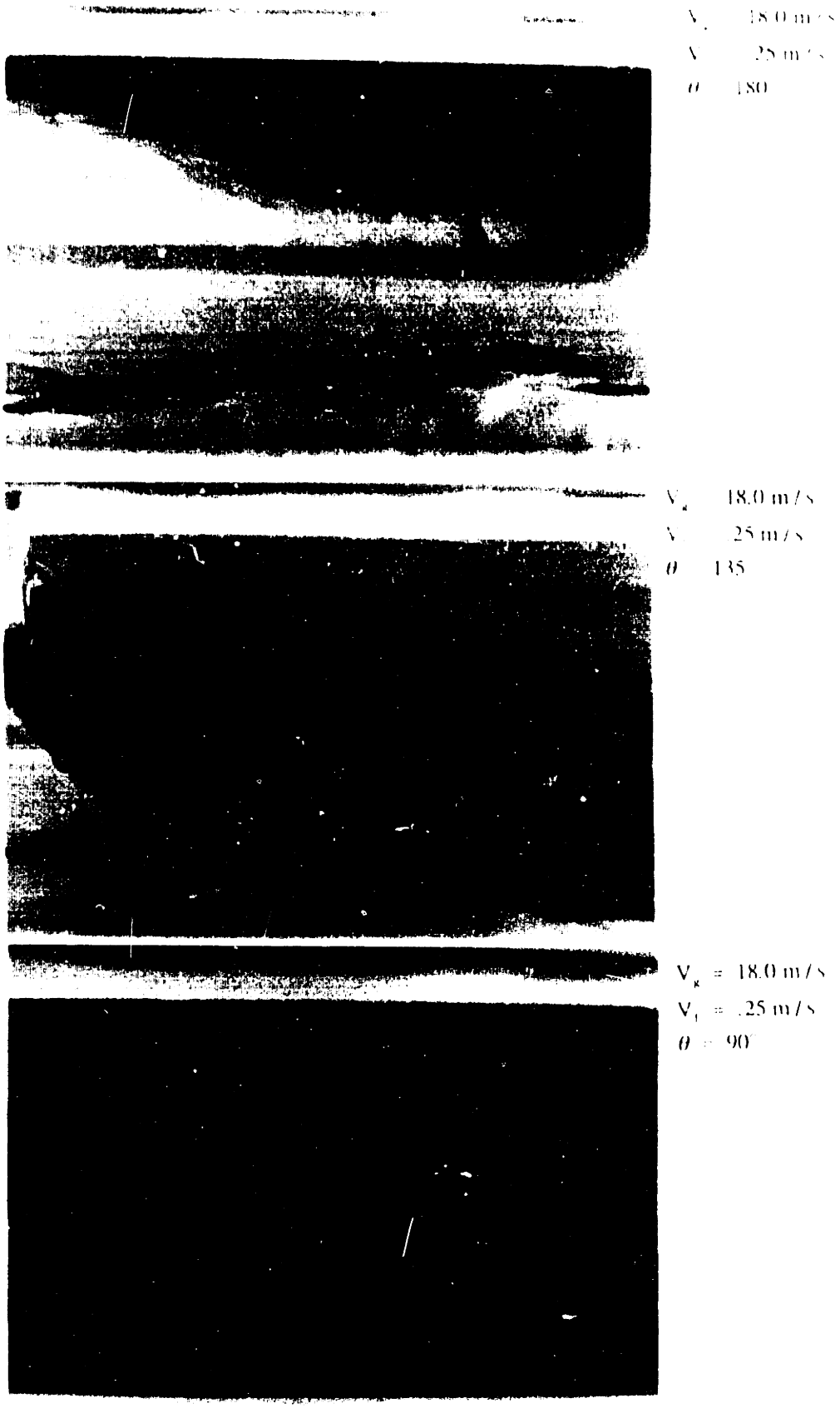

Figure 4-8: Dye Experimental Results

taken and should not be confused with the dye or waves. No wave pumping actions near the dryout limit were ever seen in the experiments or the photographs.

The importance of the wave mechanisms seems small near the dryout limit in annular flow. The almost instantaneous circumferential mixing witnessed in the experiments contradicts the wave mechanisms prescribed behavior. It appears that wave spreading plays a part only in the dryout region near the slug to annular flow boundary and is not seen past the onset of entrainment. The pumping of disturbance waves as described by Ousaka did not exist at all in these experiments. This author believes that the two wave mechanisms do not play a major part in carrying liquid up the top half of the tube's walls near the dryout region. Though the wave action may be important for spreading liquid when the film is thick, it does not appear to be important near the dryout limit where the film is very thin (near .0004m thick). However, since the experiments only dealt in angles greater than or equal to 90 degrees, the phenomenon may have been missed altogether in the tube's bottom. Hewitt noted that in similar circumstances the wave spreading effects were not seen past this angle (Hewitt, Jayanti, & White pp.1097-1116). In annular flows with substantial film thicknesses and flowrates however, the two wave spreading mechanisms may have important effects on film thickness and distributions around the tube's circumference. Since the experiments did not show a clear unsteady flux from top to bottom, they seem to indicate a force, other than waves, mixing and slightly pulling the liquid up the tube's sides near dryout.

Chapter 5

Secondary Flow

Secondary flows in the annular flow regime can be caused by both a circumferential variation of roughness on the gas/liquid interface and the asymmetric shape of the gas core. The secondary flows are thought to consist of two counter-rotating vortices that shear the liquid film upward against the force of gravity (see Figure 5-1). This investigation's first goal is to prove the existence and direction of secondary flow. In the following portion of the investigation we will attempt to take quantitative measurements of secondary flow versus various flow parameters.

Existence of Secondary Flow Experiment

With the previously stated goals in mind, an experiment was constructed. The dryout tests' set-up was also used in this experiment (see Figure 2-1). To visibly capture the secondary flow mechanism, vortex meters were constructed and set into the cross-section of the tube (see Figure 5-2). Rotors were attached to an almost frictionless frame via needle bearings and teflon couplings. The .75" diameter and location of the vortex meters were designed to keep them within the gas core. Thus, the liquid film during annular flow would neither be touched nor affect the rotation of the rotors (see Figure 5-3). The rotors were held into place by two sets of three-pronged, threaded positioners (see Figure 5-4).

After the vortex meters were placed in the tube's cross-section, the system was brought to the annular flow regime. The meters reacted by spinning in constant counter rotations as described by Figure 5-1. The phenomenon was also captured on video tape (Appendix) and after slow-motion review, revealed angular rotations on the order of 6 rev/s.

The counter rotation of the paddle wheels give a visual insight into secondary flow. Both rotors move upward near the liquid /film interface and downward at the center of the gas core. This rotation presents the visual pattern hypothesized previously. Through analysis, both a potential vortex or a solid body rotation flow pattern on either side of the transverse centerline would give the same paddle wheel behavior. By definition, these two flow patterns also display velocity as a linear function of angular rotation (Gerhart & Gross p.201). From this experiment, however, it is impossible to define specifics about the secondary flow pattern. The overall pattern of secondary flow, seen through the paddle wheel experiment, proves the existence of a flow that is favorable to the hypothesis of shearing liquid up the walls of the tube.

The circumferential variation of roughness in the tube's cross section is believed to be the main factor causing secondary flow in the gas core. Near dryout, in annular flow the top half of the gas/liquid interface contains a much thinner and smoother film than that on the bottom half (see Figure 5-5)(Laurinat p.159). Because it contains a greater depth of fluid, the bottom half of the interface tends to have a "rougher" surface of waves and ripples. On average, the film travels at approximately 15% of the gas velocity and thus, for all practical purposes, is stationary in comparison to the gas (Wallis p.363). Therefore, traveling axially down the tube, the gas sees a rougher surface on the lower

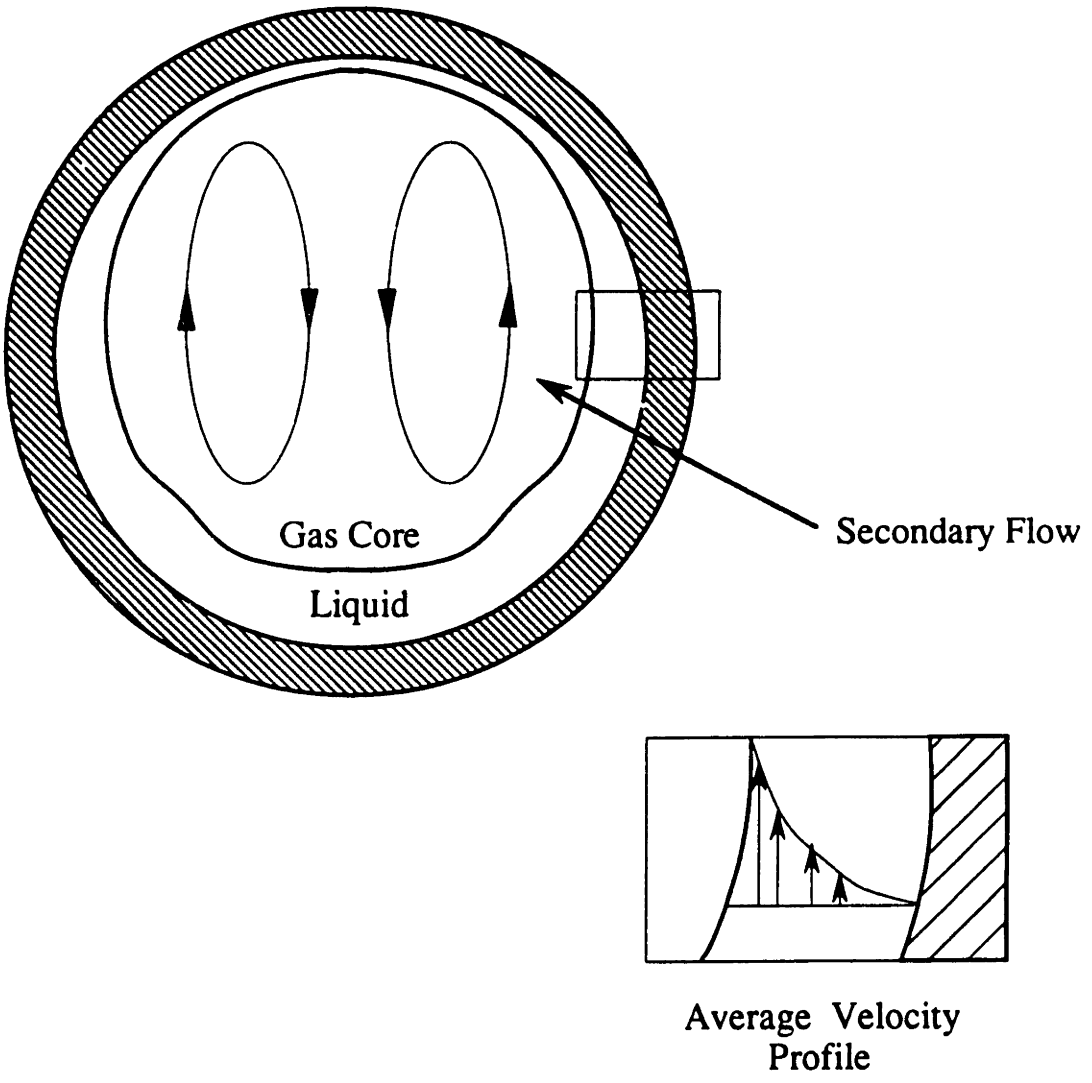

Figure 5-1: Secondary Flow Visualization

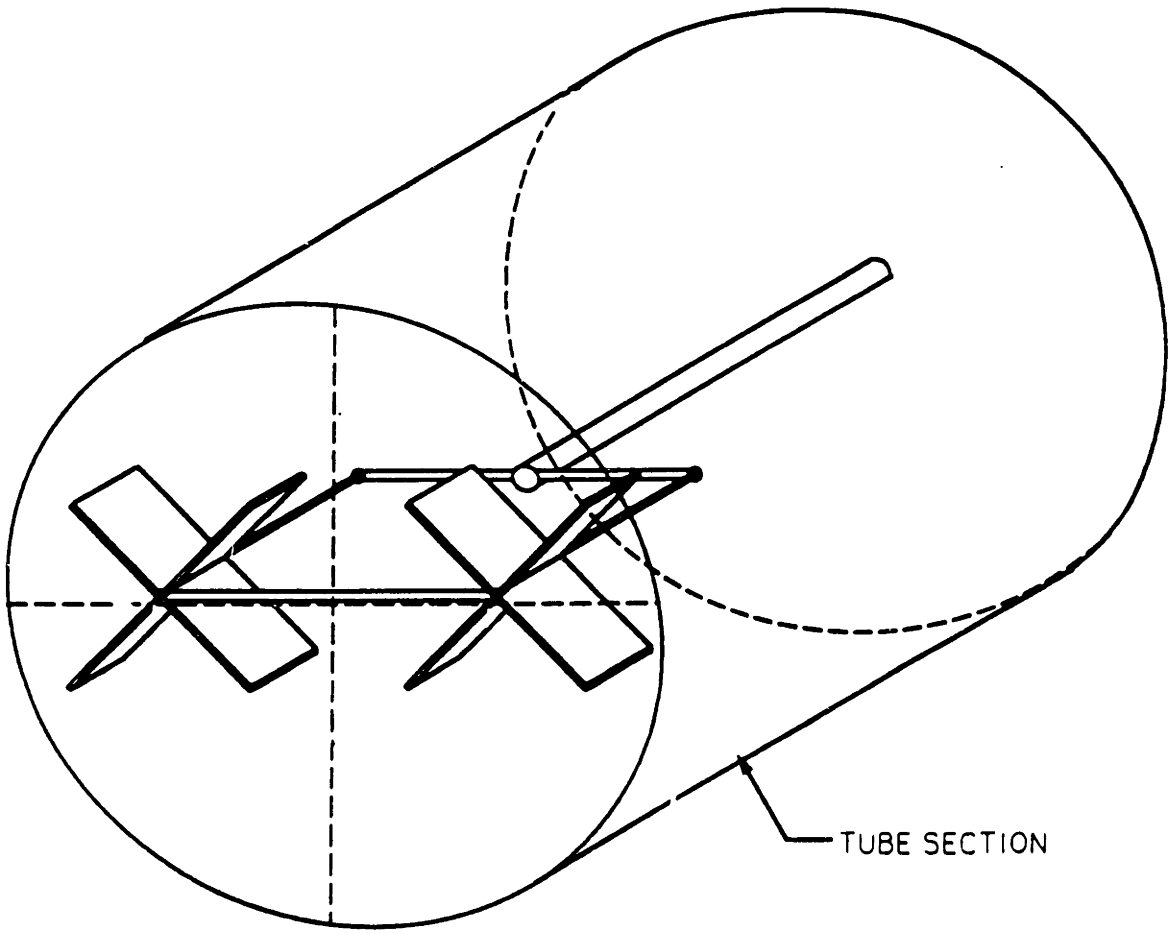

Figure 5-2: Vortex Meter Configuration

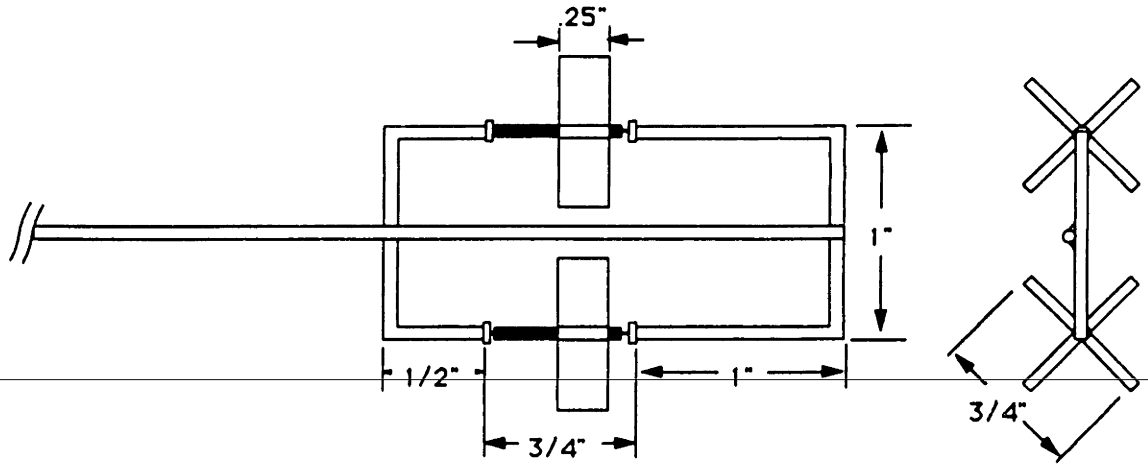

NOTE: 1/16" COPPER ROD: COMMON

Figure 5-3: Vortex Meter Dimensions

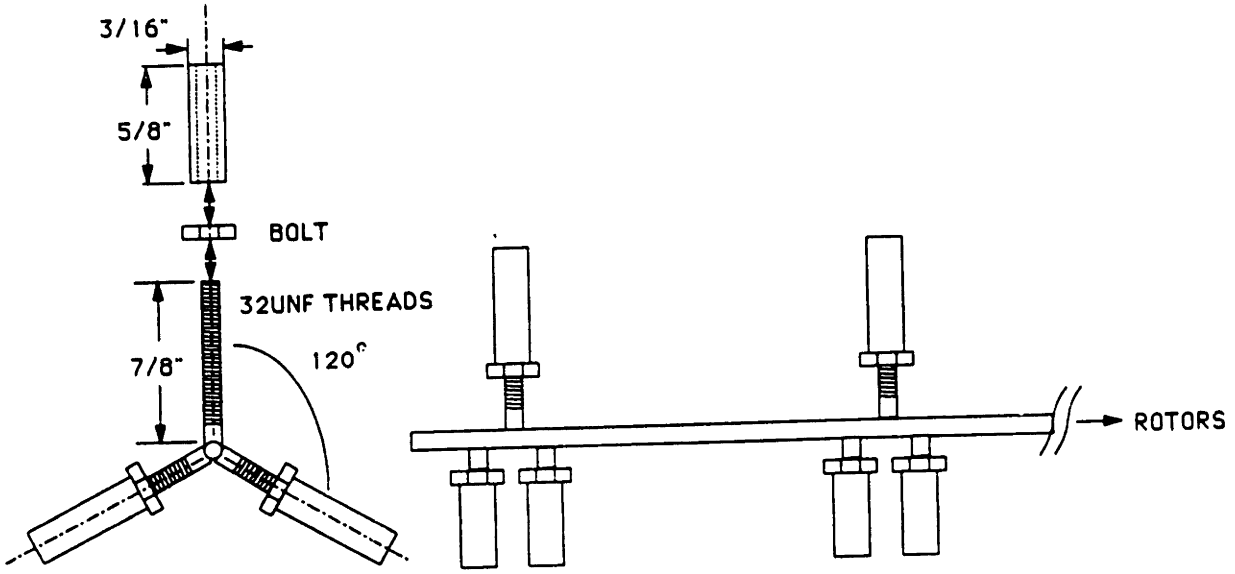

Figure 5-4: Vortex Meter Positioner

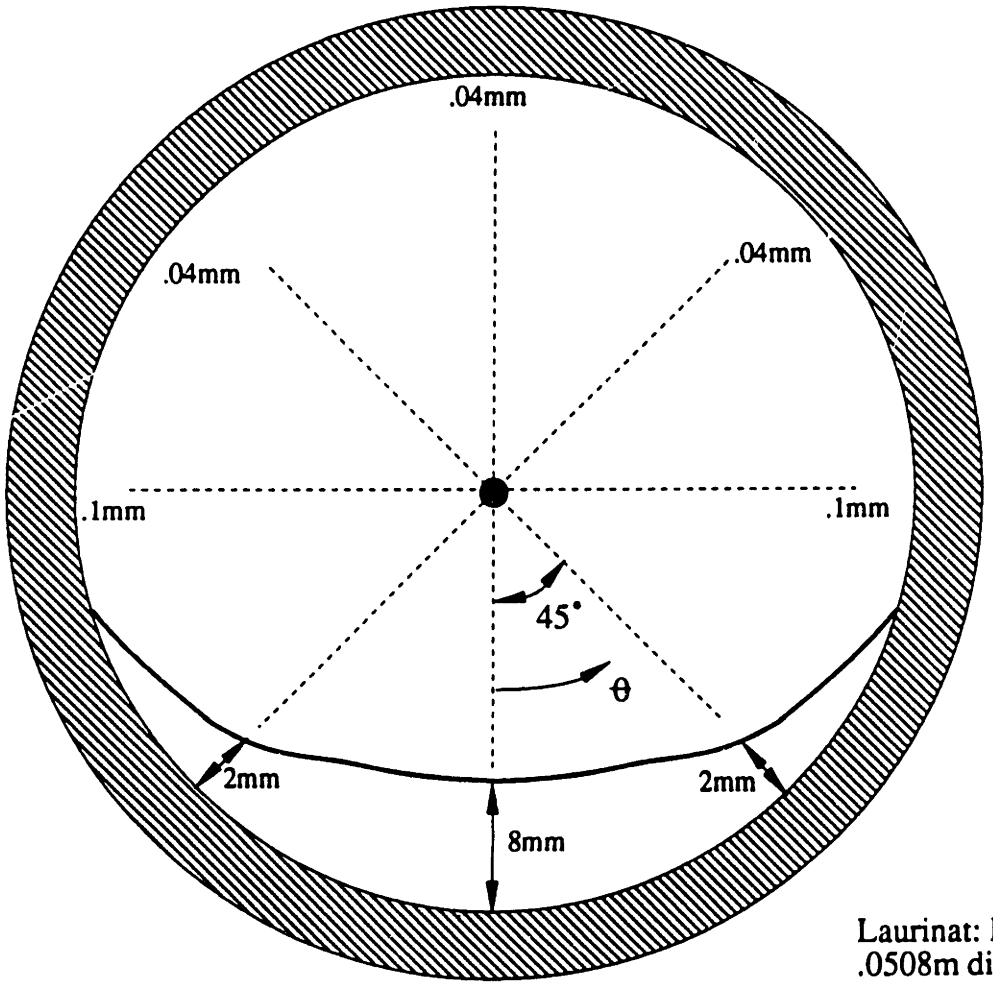

Figure 5-5: Laurinat's (1982) Air-Water, Film Thickness Profile for Annular Flow in a .0508m Diameter Tube near Dryout

half of the tube than on that of the upper. This variation in the roughness is believed to be the major cause of the secondary flow pattern.

Quantitative Investigation of Secondary Flow

To better understand secondary flow and its causes, another experiment was constructed. This experiment's goal was to relate the gas-liquid flow to that of only a single phase with varying roughnesses. In other words, to capture the two-phase secondary flow in a single-phase experiment by varying sand roughnesses around the tube(see Figures 5-6 & 5-7). Instead of the wavy surface causing a variation in the roughness, various sand roughnesses were used. The final result of the experiment was to determine the relationship between axial gas velocity, roughness, and the rotors' angular velocities.

This experiment again used the dryout tests' set-up with a few modifications. The water inlets were closed and only air entered the tube. The last 4' section of 2" tubing was cut into equal bottom and top halves. Various roughnesses were glued to the bottom half of the tube while the top half remained smooth. As in the original experiment, the vortex meters were placed in the tube's cross-section (Figure 5-7). When the gas entered this new system, the paddle wheels began rotating up at the wall and down at the center as seen for annular flow. Thus, validity was given to the roughness hypothesis. For each roughness in the bottom half of the tube, the paddle wheel's angular rate of rotation was measured as a function of axial velocity.

Two methods were used to create the various roughnesses. The two smaller roughnesses were made from 60 and 36 grit sandpaper. The grit readings converted to

.310 mm. and .544 mm. roughness heights, respectively (Malkin pp.20-21). The larger roughnesses were made from spherical beads and their roughness values were taken to be equal to their diameter. In the case of the 3 mm diameter beads, however, they were so closely packed that a value of roughness equal to the radius was assigned. Therefore, the four roughness heights ranged from .310 mm. to 2 mm..

The angular velocity measurements on the rotors were made by sending a laser beam through the clear PVC onto a receiver on the opposite side of the tube. Each time one of the paddle's four vanes turned past a certain point, they intercepted the laser and its receiver. These interactions were then counted through a data acquisition system as a function of time (see Figure 5-8). The laser employed in this experiment was a 1.0 mW LaserMed laser pointer. The receiver used was a Newport Research Model 818-SL Photosensor. The data acquisition system included Notebook Version 4.3 and an IBM AT PC. A pitot probe and manometer measured axial velocity within the tube. Three calibrations were performed on the experimental set-up in order to clarify the tests' results. Following the calibrations, angular velocities were measured for four different roughnesses.

The first calibration consisted of putting a paddle wheel into a known swirl or solid body rotation and measuring its angular velocity. Accordingly, a single paddle wheel was constructed and placed in a 1" diameter clear PVC tube 1.25" from the exit of a swirler (see Figure 5-9). The swirler was a 1/32" thick aluminum strip, 9" long and 1" wide, and twisted a full 360 degrees equally over its length. Gas was forced through the swirler and past the paddle wheel exiting in a presumed solid body rotation. The paddle wheel's angular velocity was then measured along with the axial velocity of the gas. The angular velocity measurement of the paddle wheel could then be calibrated to the actual

amount of rotation present in the flow (see Figure 5-10). Knowing the swirl length, amount of twist and the axial velocity of the gas, the true rotation in the gas was determined. The paddle wheel's angular velocity lags an almost constant 13.8 rad/s behind the actual rotation in the gas. This value is assumed to be the slip due to bearing friction and is added to all angular velocities measured in the following experiments.

To clarify gravity's lack of effect on the secondary flow pattern, a second calibration was performed. In other words, unlike the two-phase flow, gravity should not affect the single-phase flow patterns. In this test, the paddle wheels were placed in the 2" diameter set-up with the smooth half of the pipe placed on the bottom and the rough half placed on the top. Gas was forced through the tube and the paddle wheels rotated in exactly the same manner as they had in the original set-up with the outer vanes(closest to the tube's walls) rotating from the rough portions to the smooth. Therefore, as expected, gravity did not affect the single-phase secondary flow pattern.

The third calibration was performed to give a sense of robustness to the measurement technique. Due to various roughness heights and human error, it was impossible for the rotors to be placed in the exact same location within the tube's cross-section for each test. In addition, small misalignments from the horizontal were bound to occur at some point in the experiments. Therefore, a series of tests were performed to find the effects of these potential deviations. A special set of positioners were designed to position the vortex meter over a wide area within the tube's cross-section (see Figure 5-11). With a constant gas velocity in the tube, the vortex meter was moved to several different cross-sectional locations within the tube at which the angular velocities were measured. The dimensionless results are plotted in Figure 5-12 at their individual

locations. The largest deviation in measurements was approximately 25% showing there is a certain level of robustness to the experimental technique.

The calibrated results of the experiment are given in Figure 5-13. Angular rotation is plotted versus axial gas velocity for the four different roughnesses. For both axial velocity and roughness the angular velocity of the rotors increases. The increments of angular velocity between the different roughnesses appear to follow a similar pattern.

An experimental correlation was developed relating the three parameters. Average gas velocity, roughness and angular velocity were put into a single correlation using the experimental data. From Figure 5-13 it appeared that axial gas velocity scaled linearly with the angular velocity of the rotors. A logarithmic relationship captured the effect of roughness by plotting the angular velocity of the rotors over the axial gas velocity versus the roughness height (see Figure 5-14). The final relationship was given by:

$$\omega \approx 1.07 V_g \log\left(\frac{1000\varepsilon}{.03}\right) + 5.03. \qquad (5\text{-}1)$$

This correlation fit the majority of the data with only a small offset from the origin (see Figure 5-15) . The offset was assumed to be a slight calibration error in the data due to bearing friction. With this in mind, the offset constant was subtracted from both the data and the correlation leaving the fit seen in Figure 5-16 where

$$\omega \approx 1.07 V_g \log\left(\frac{1000\varepsilon}{.03}\right). \qquad (5\text{-}2)$$

Thus, all experimental angular velocity data was then corrected by adding 8.8 rad/s instead of 13.8 rad/s determined in the single rotor calibration. Although the data was

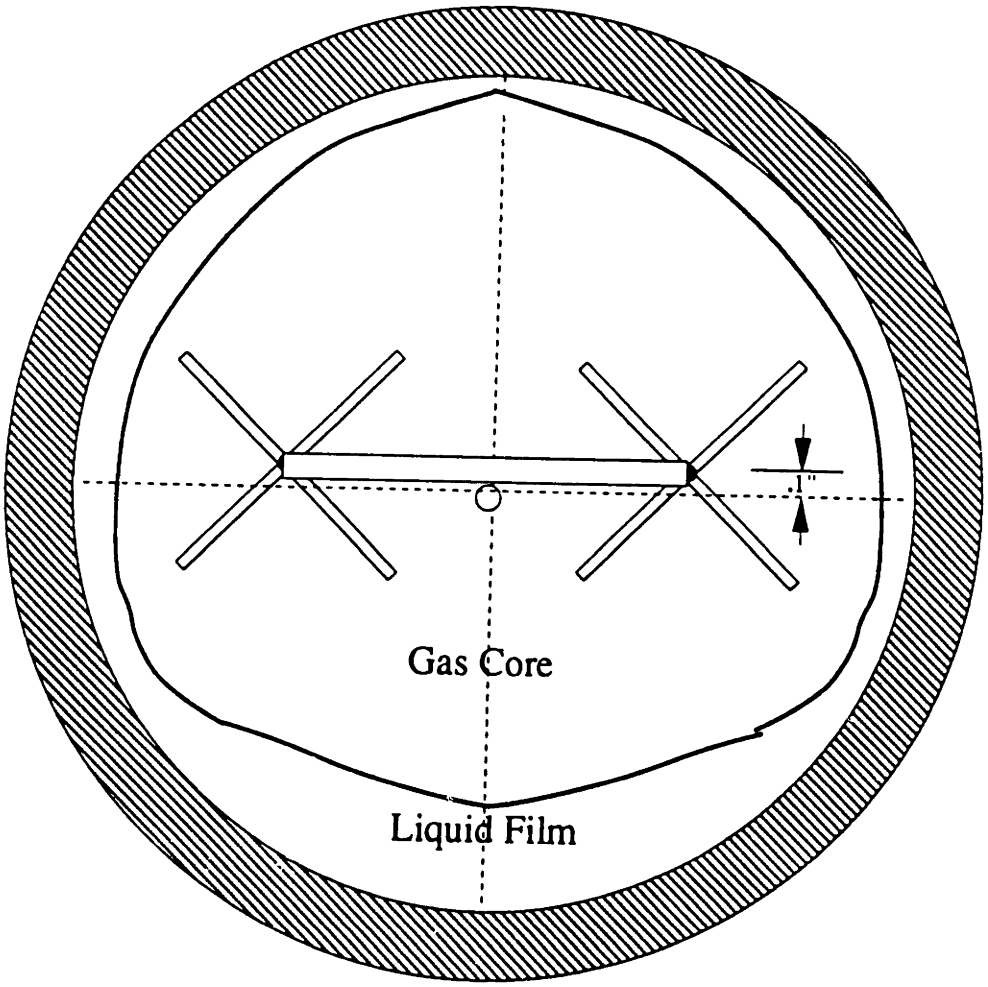

Figure 5-6: Vortex Meter Placement in Annular Flow

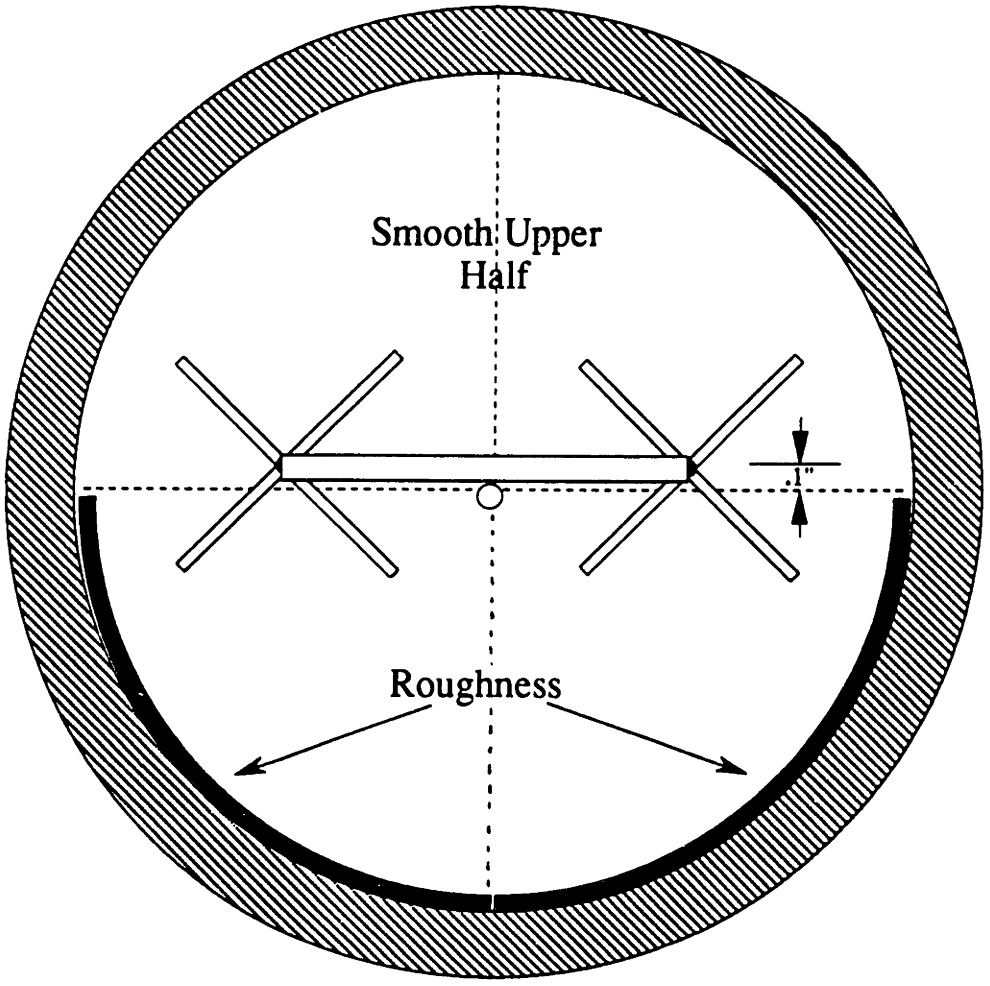

Figure 5-7: Vortex Meter Placement in Single-Phase Flow with Varying Roughnesses

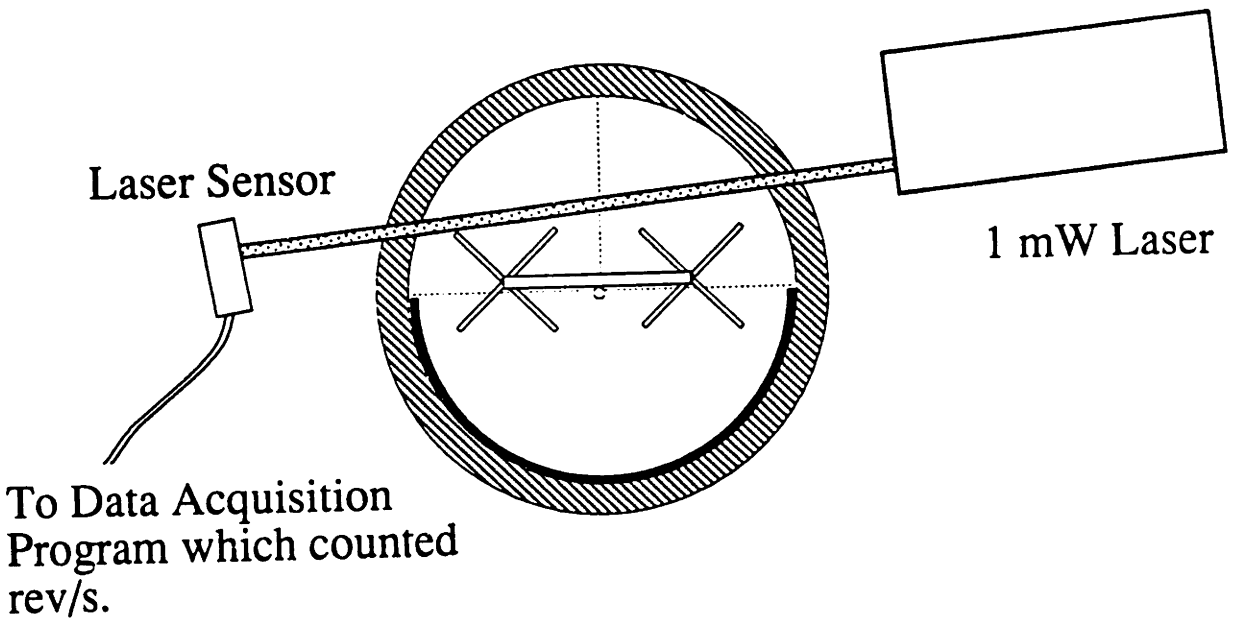

Figure 5-8: Secondary Flow Data Acquisition Set-Up

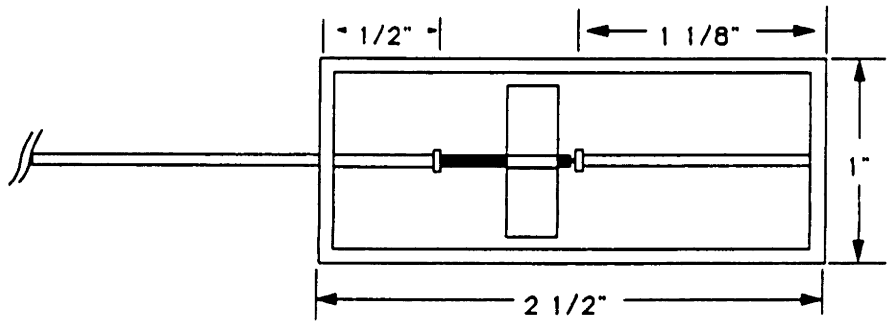

NOTE: 1/16" COPPER ROD: COMMON

Figure 5-9: Vortex Meter Calibrator Dimensions

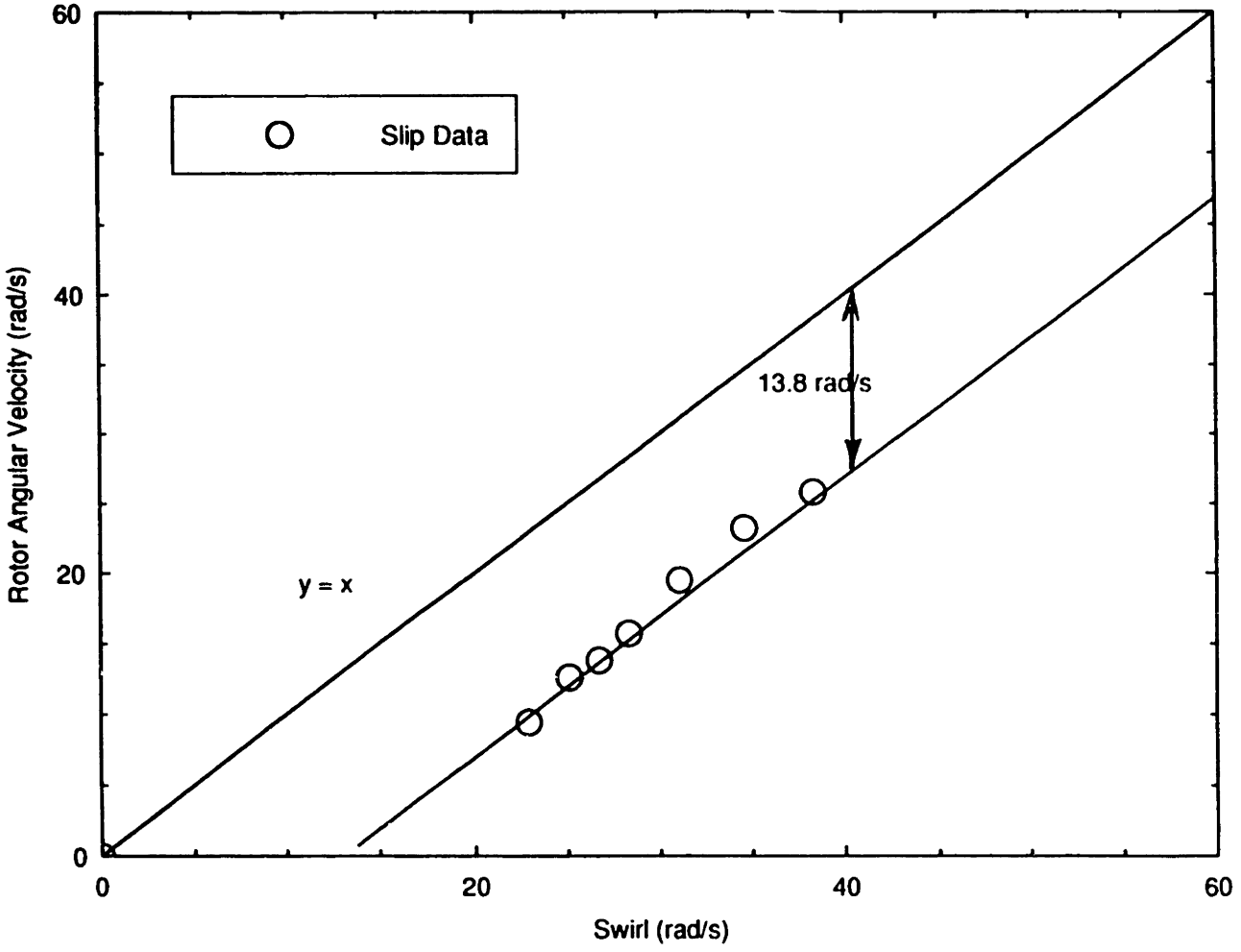

Figure 5-10: Vortex Meter Calibration Results

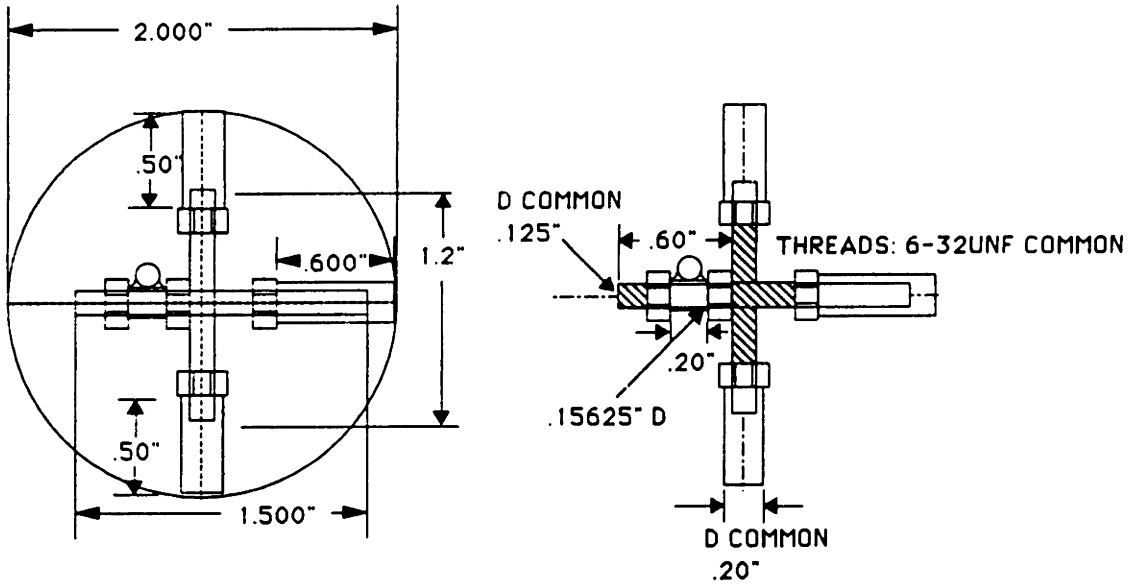

Figure 5-11: Vortex Meter Position Calibration Set-Up

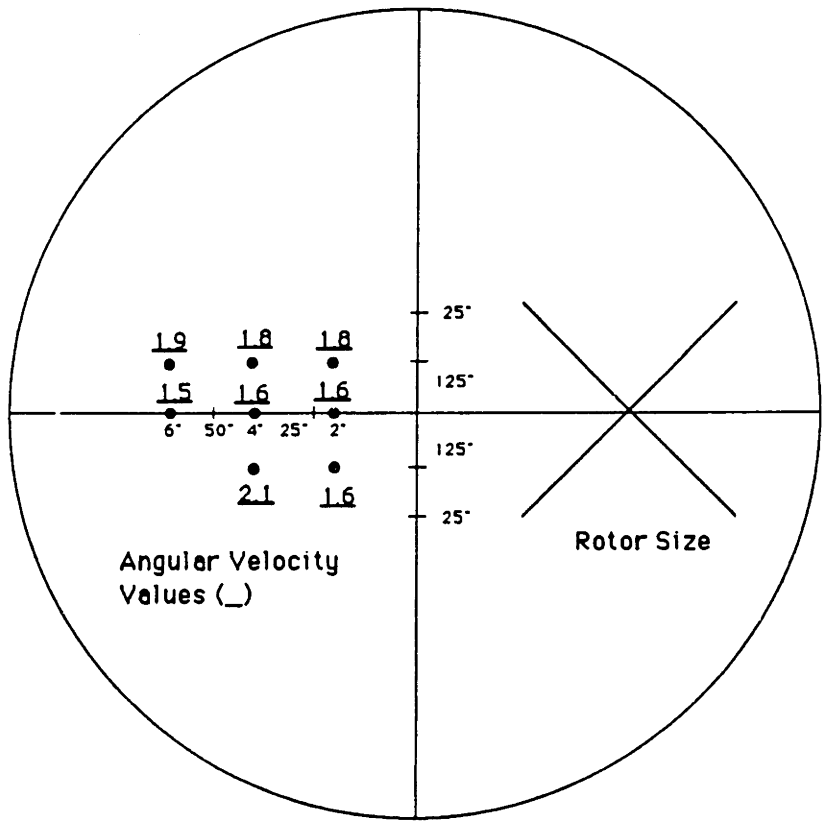

Tube Cross-Section

Figure 5-12: Position Calibration Results

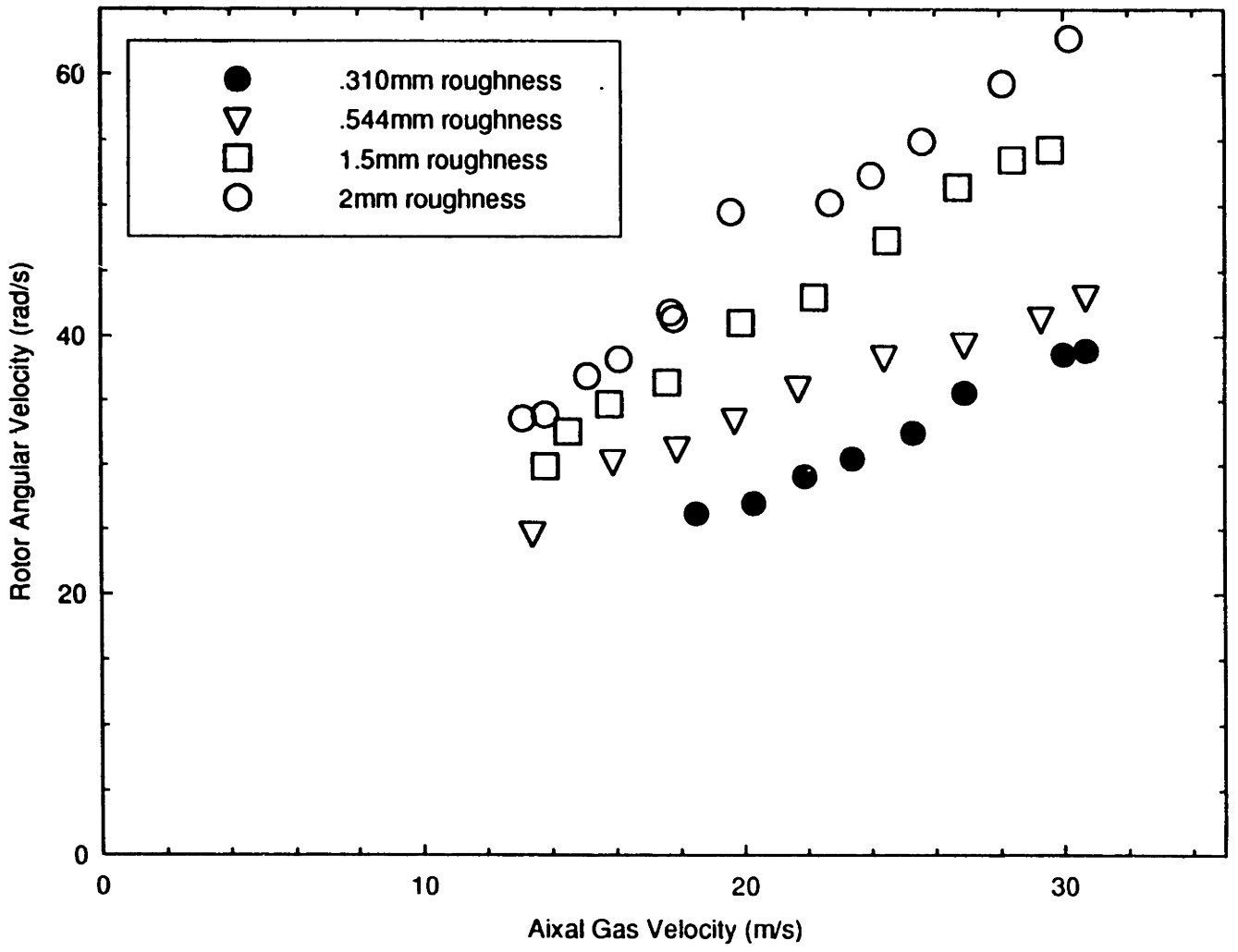

Figure 5-13: Secondary Flow vs. Gas Velocities and Roughness

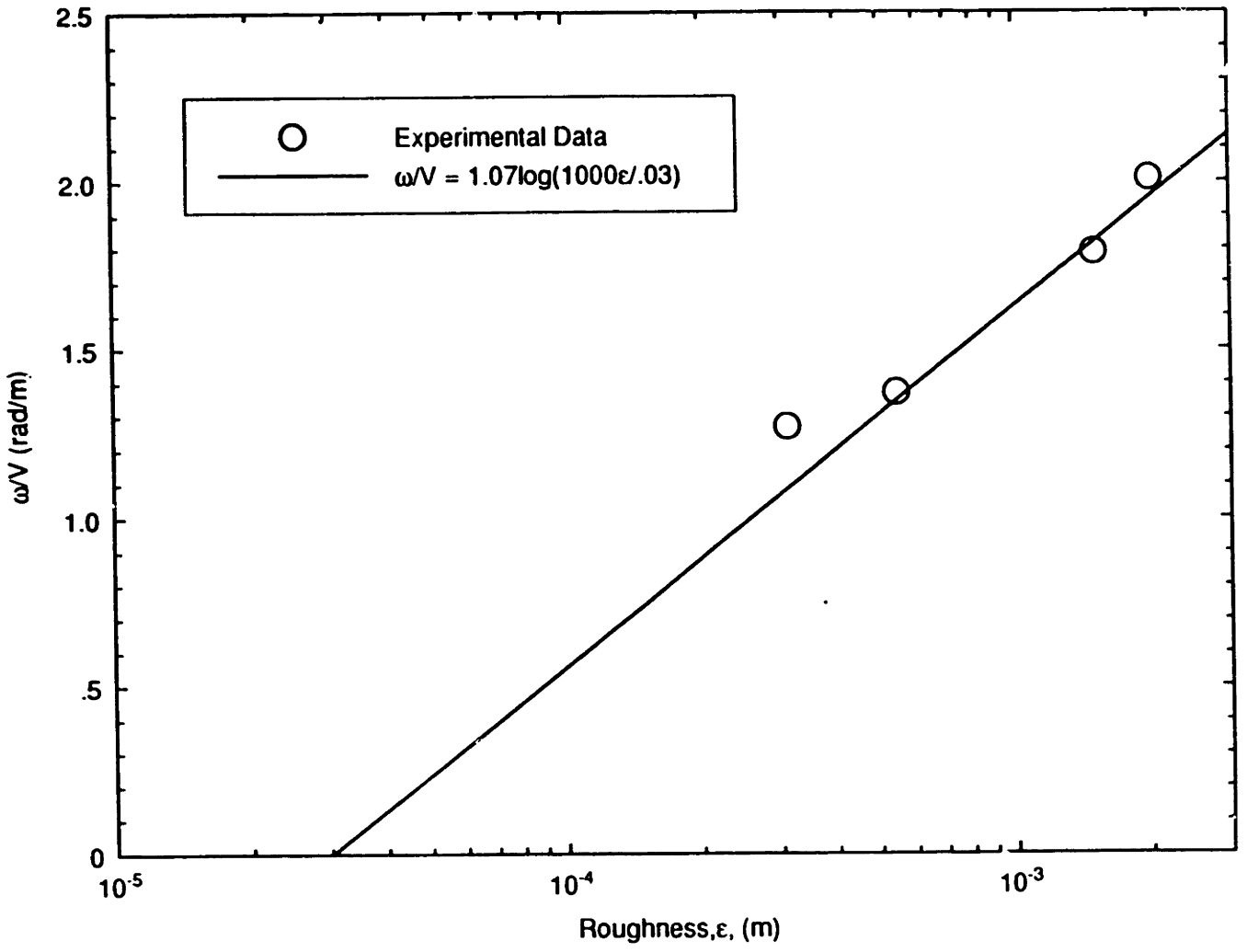

Figure 5-14: Data Correlation

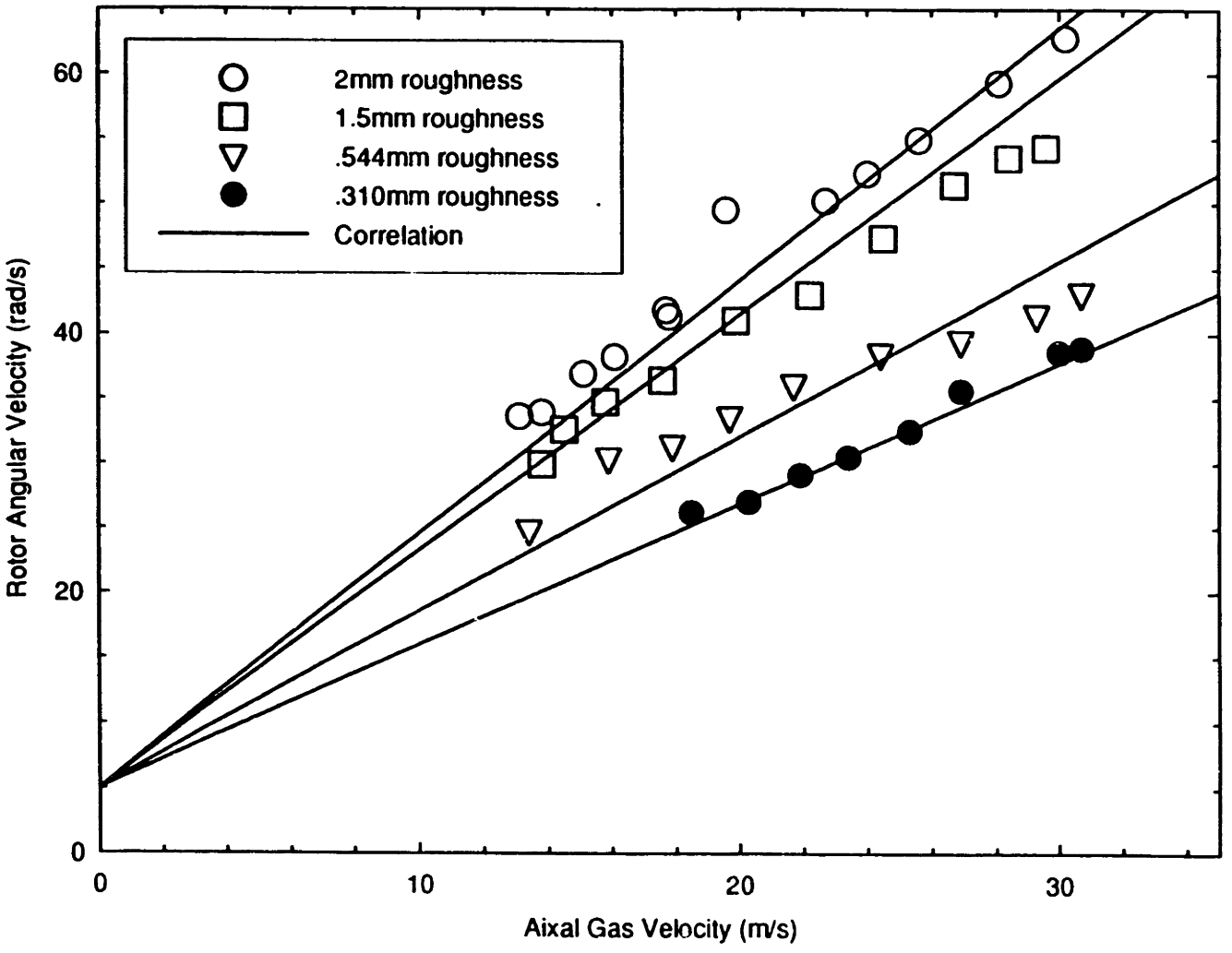

Figure 5-15: Secondary Flow Correlation and Data

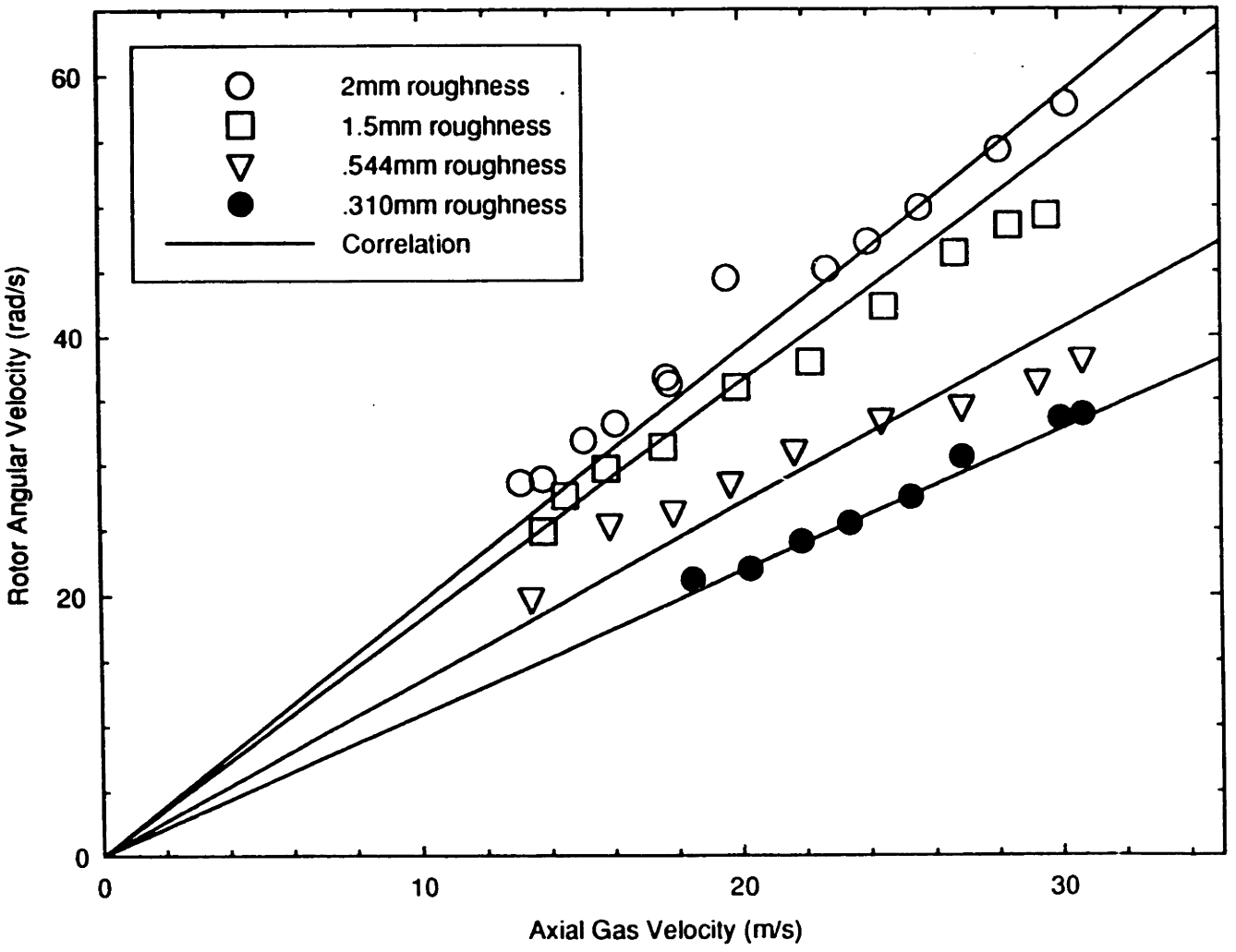

Figure 5-16: Recalibrated Secondary Flow Correlation and Data

slightly manipulated, it was only through a constant. Thus, the behavior of the data was retained and believed to be of much greater significance.

Pressure Differential Experiment

To further reinforce the existence of secondary flow, pressure measurements were made in the single phase half rough/smooth tubes. The differential pressures were measured between the top and bottom of the tube's cross-section in an attempt to detect the secondary flow's pressure effect.

The differential pressure experiments were performed on the same single-phase set-up used in the secondary flow tests. Both the 2mm and .544mm roughnesses were used to gather data. The .042" diameter square -edged taps were placed on both the top and bottom of the tube's cross-section using several different geometries (see Figure 5-17). To accurately measure pressures down to .5 Pa, a high precision Dwyer model 1430 manometer was used. A pitot probe and manometer were again used to measure the axial gas velocity. The various taps were arranged from the top to bottom of the tube (see Figure 5-18) and the differential pressures were measured as a function of gas velocities. Several tap geometries were used in an attempt to disprove their effects on the pressure measurements due to disrupted streamlines over individual roughnesses.

The results for both roughnesses, along with their corresponding tap geometries, are shown in figures 5-19 to 5-20. Positive pressures represent higher pressures at the bottom of a given cross-section. The cumulative data for both roughnesses is shown in Figure 5-21.

Although the data displays a large amount of scatter, much can still be inferred from the results. The 2mm roughness data is comprised of five different tap geometries, but it still all falls within an order of magnitude and displays squared polynomial behavior. The .544mm roughness data, which is comprised of two different tap geometries, also gives similar magnitude and behavior. These characteristics tend to verify that the taps only have small scale effects on the data. It was expected that the larger roughnesses would create greater scatter in the data due to the bending of streamlines around each individual roughness. This was verified with the cumulative data from both roughnesses in Figure 5- 21. However, the average behavior and magnitude of the data should give a good approximation to the real case. The cumulative data for both roughnesses was averaged and fit to second order polynomials (see Figure 5-22).

To prove the consistency of the pressure behavior from top to bottom, pressure measurements were also taken one tube diameter downstream of the roughness. The taps were arranged one tube diameter downstream of the roughnesses to capture the pressure differential before it vanished in a turbulent mixing length. The data for the .544mm roughness displayed the expected behavior and gave pressure differences slightly less than those found within the roughness (see Figure 5-23). The 2mm roughness measurements show a large amount of scatter with no particular pressure differential bias either way (see Figure 5-24). The difference in the data's behavior is attributed to the larger roughness' individual wake effects continuing one tube diameter downstream. The smaller roughness' wake effects are believed to disappear before one tube diameter downstream giving pressure behavior consistent with that found in the roughness. In light of the actual data however, these measurements are inconclusive.

Although there are additional pressure measurement errors caused by tap burrs and misalignments, they are small. When constructing the taps, small misalignments between the top and bottom on the order of .125" most likely occurred and their resulting errors can be calculated analytically. First, the gas flow must be defined as compressible or incompressible using the Mach number. The Mach number is simply the velocity of the fluid divided by the speed of sound (300m/s). The experiment's Mach numbers ranged from 0 to approximately .1. Using the ideal gas law and standard manipulations the largest Mach number causes the fluid's density and temperature to change by less than 1% (Gerhart & Gross p.681). The flow is therefore, assumed incompressible. For steady, incompressible, turbulent flow in rough pipes , the Moody diagram or Colebrook formula can be used to find pressure gradients between various points. For simplicity and an upper bound, the entire cross-section of the tube is assumed to be rough. The Colebrook formula relates the tube's roughness to a friction factor with the following:

$$\frac{1}{\sqrt{f}} = -2.0\log\left(\frac{\varepsilon/D}{3.7}\right) \qquad (5\text{-}3)$$

The friction factor can then be related to the shear at the pipe's walls by the following:

$$\tau_w = \frac{f}{8}\rho_g V_g^2 \qquad (5\text{-}4)$$

By multiplying (5-4) by the tube's circumference and the distance between the taps (delta x) and dividing by the tube's cross-sectional area , the pressure drop at a given tap geometry can be found. The relationship is given by:

$$\Delta P = \frac{\rho_g V_g^{\,2}(\Delta x)}{16R\left[\log\left(\frac{\varepsilon / 2R}{3.7}\right)\right]^2} \qquad (5\text{-}5)$$

Using the fluid properties, greatest velocity of 40 m/s and the largest roughness of 3mm, a tap displacement of .0032m or 1/8", a pressure drop of less than 4 Pa occurs. As an upper bound this pressure drop is approximately 10% of the measured values. Because the upper bound error due to tap misalignments for the roughest and greatest flow rate in the experiments is less than 10% the measured values, the error is considered quite acceptable and will not significantly affect the overall results of the experiments (Gerhart & Gross p.681).

Assuming a secondary flow pattern exists as previously described, pressure differentials can be derived analytically from the tubes top to bottom. Figure 5-25 gives the hypothesized flow at the pipe's midplane. The shears which give rise to the pressure differential are described in Figure 5-26. The velocity in the tube's midsection consists of an axial and a secondary vertical component. The shears are functions of the velocity squared :

$$\tau \propto \frac{1}{2}\rho V^{\,2} \qquad (5\text{-}6)$$

However, they still retain the same geometric relationship with one another as the component velocities. Therefore, the pressure differential between the top and bottom is :

$$\Delta P \,\alpha\, \frac{1}{2}\rho_g V_g^{\,2}\sin\theta \qquad (5\text{-}7)$$

where

$$\sin\theta \approx V_s / V_g. \qquad (5\text{-}8)$$

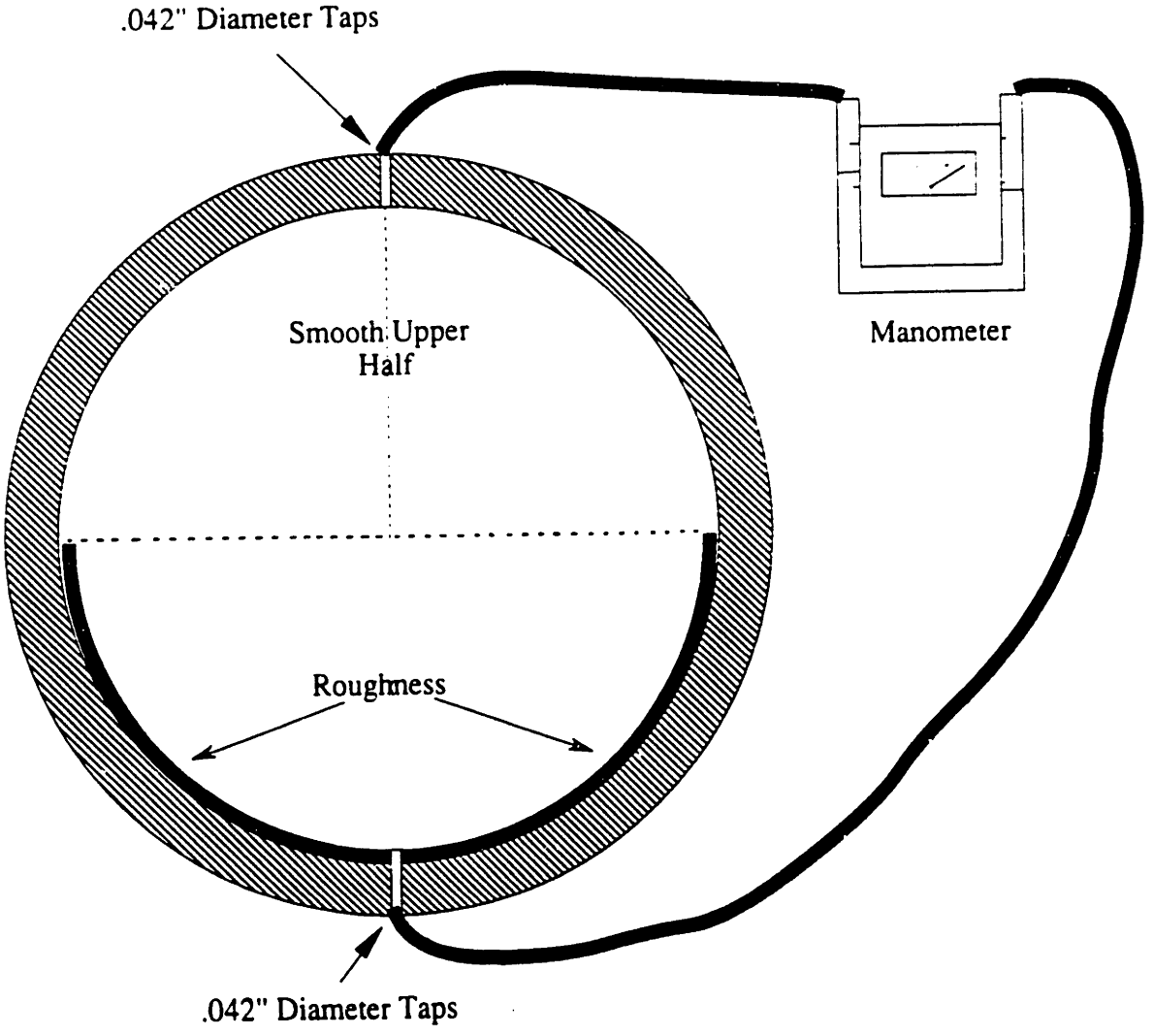

Figure 5-17: Differential Pressure Set-Up

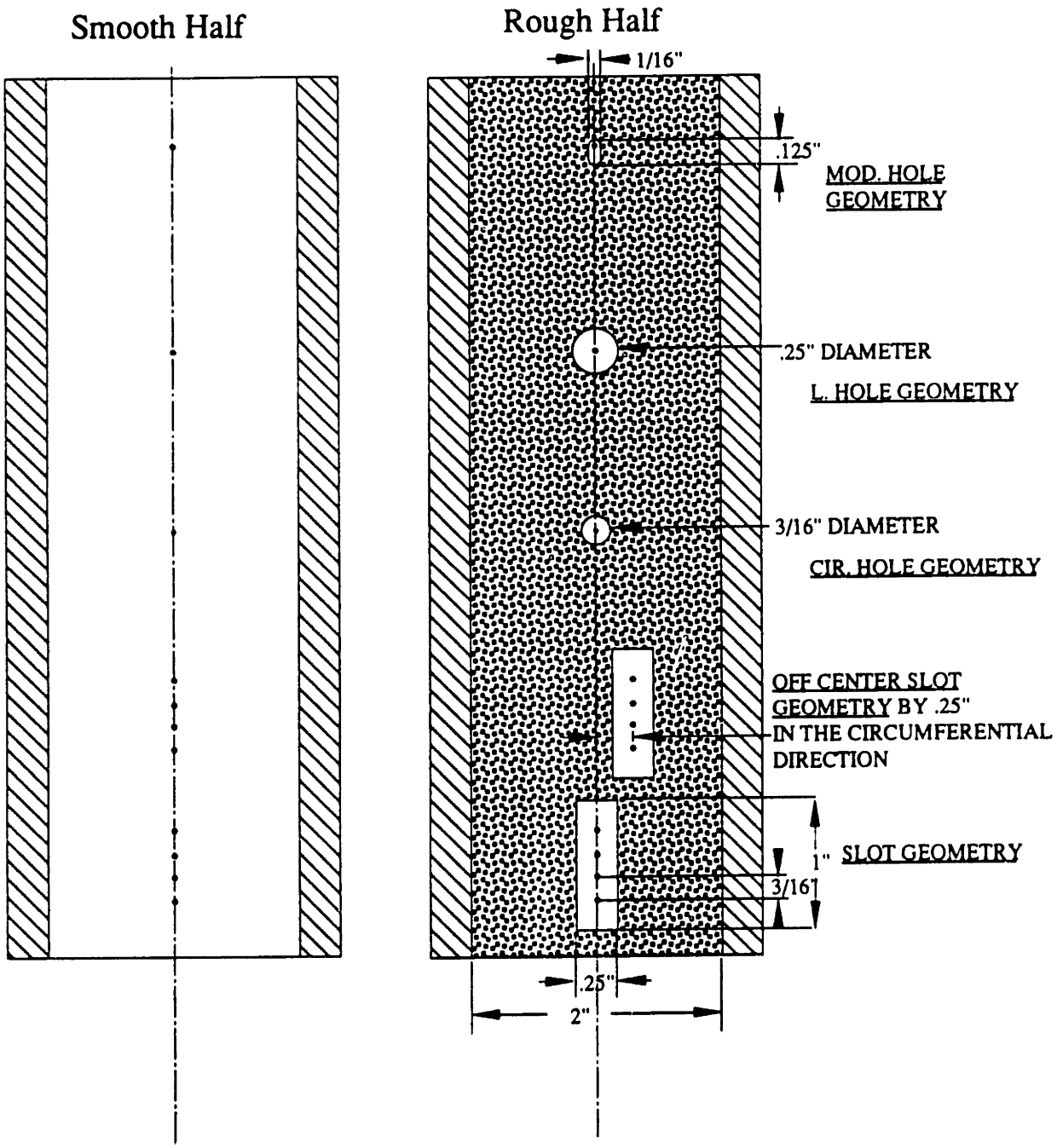

Figure 5-18: Tap Geometries

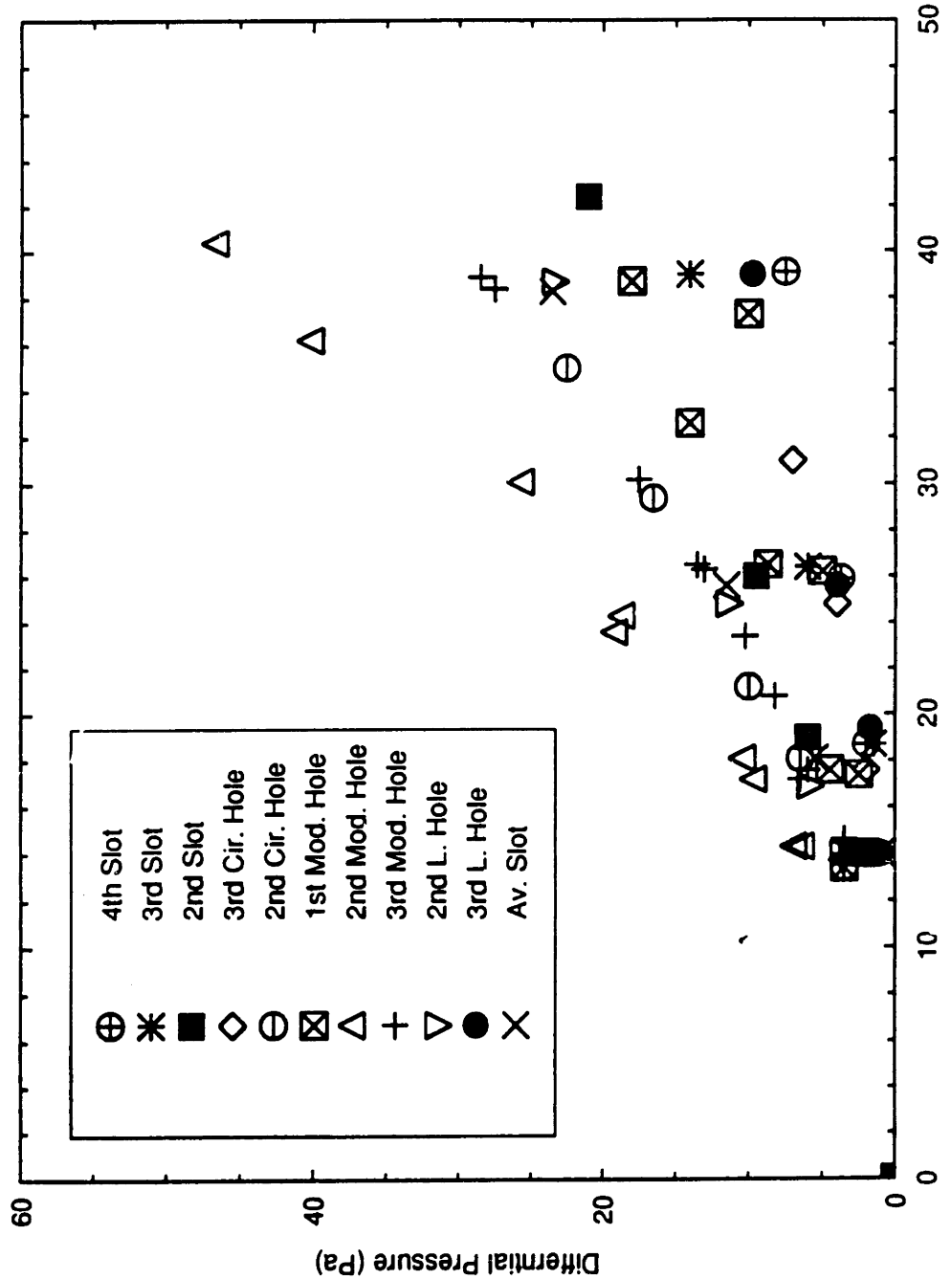

Figure 5-19: 2mm Roughness Differential Pressure Data

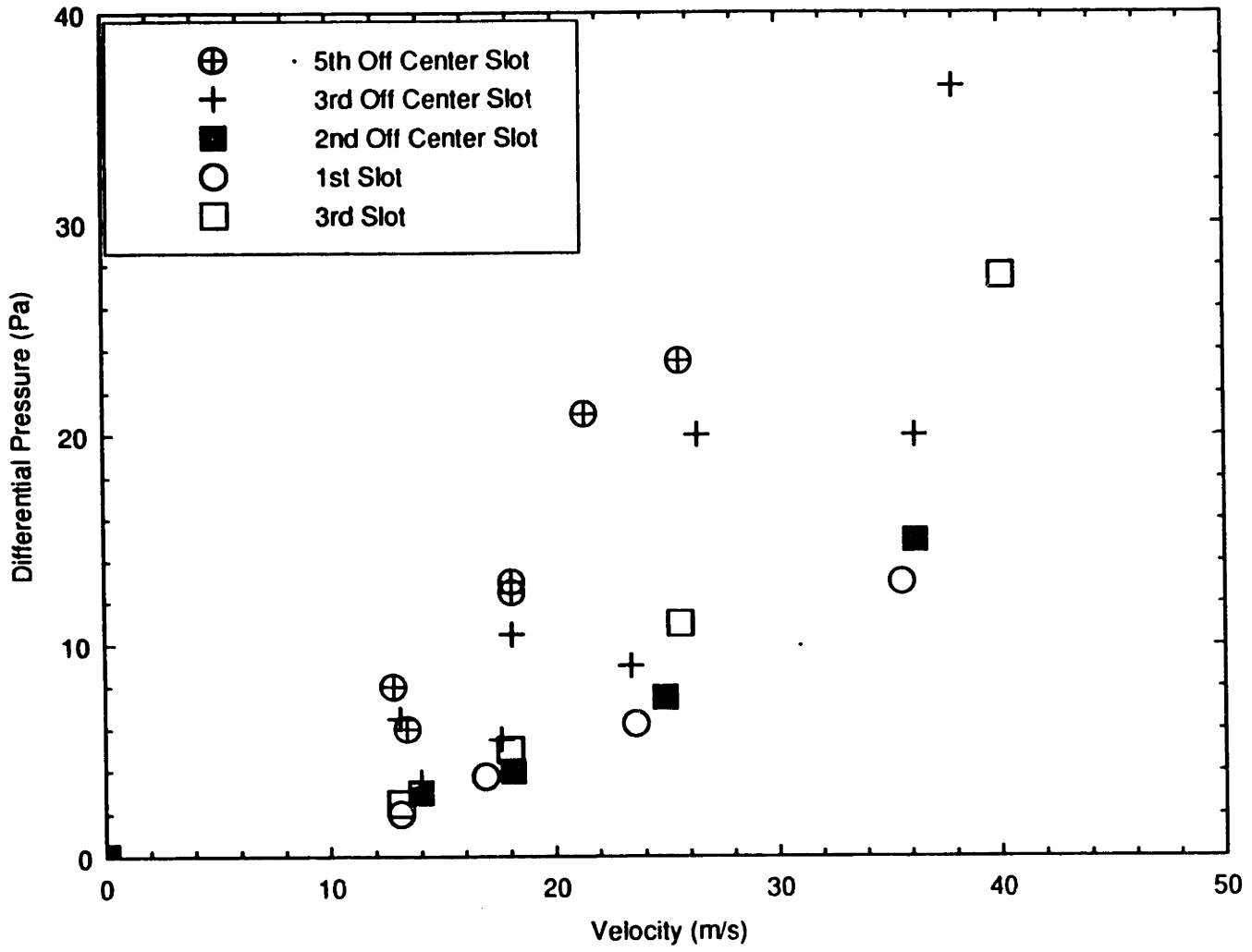

Figure 5-20: .544mm Roughness Differential Pressure Data

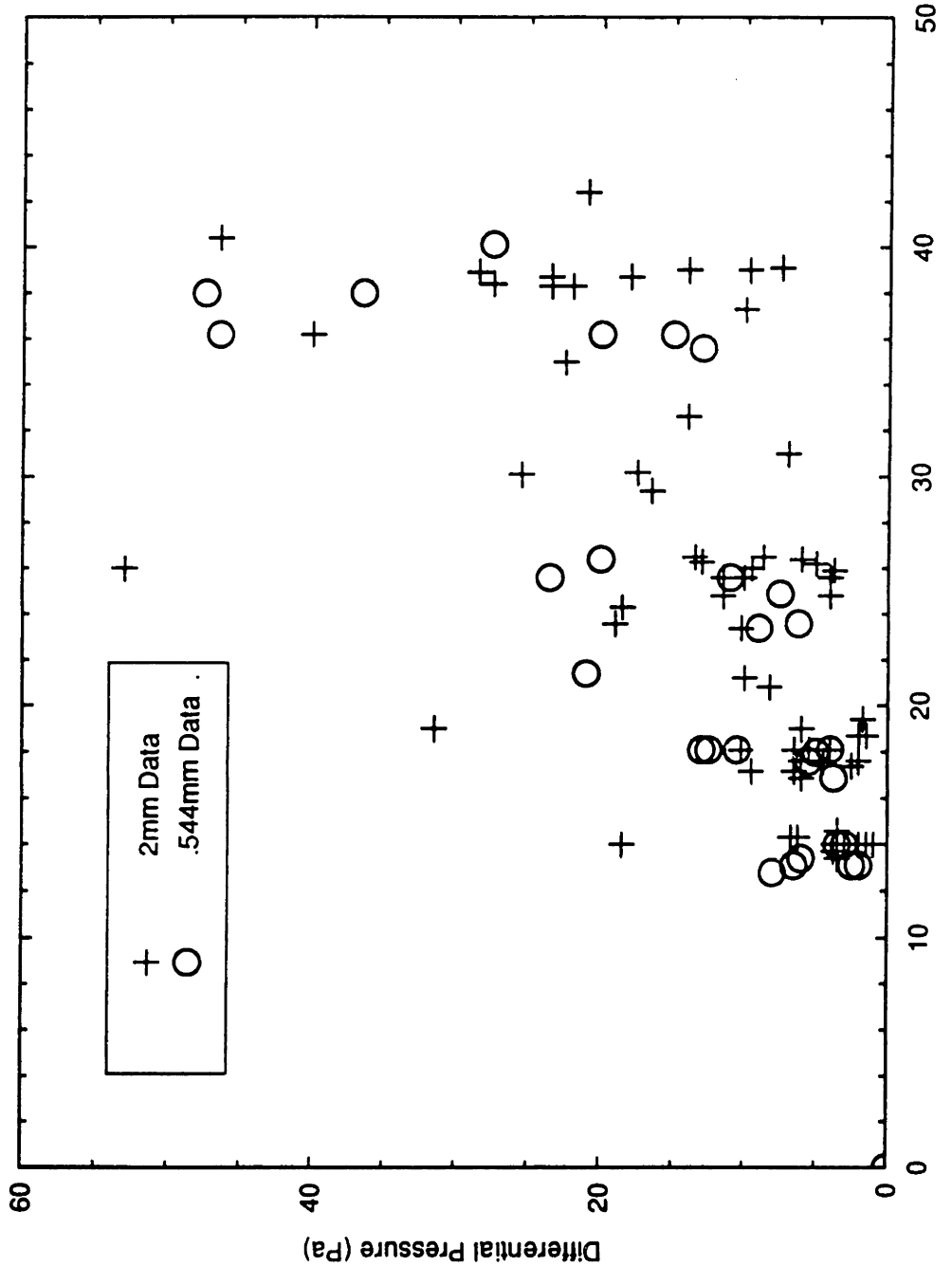

Figure 5-21: Cumulative Differential Pressure Data for both Roughnesses

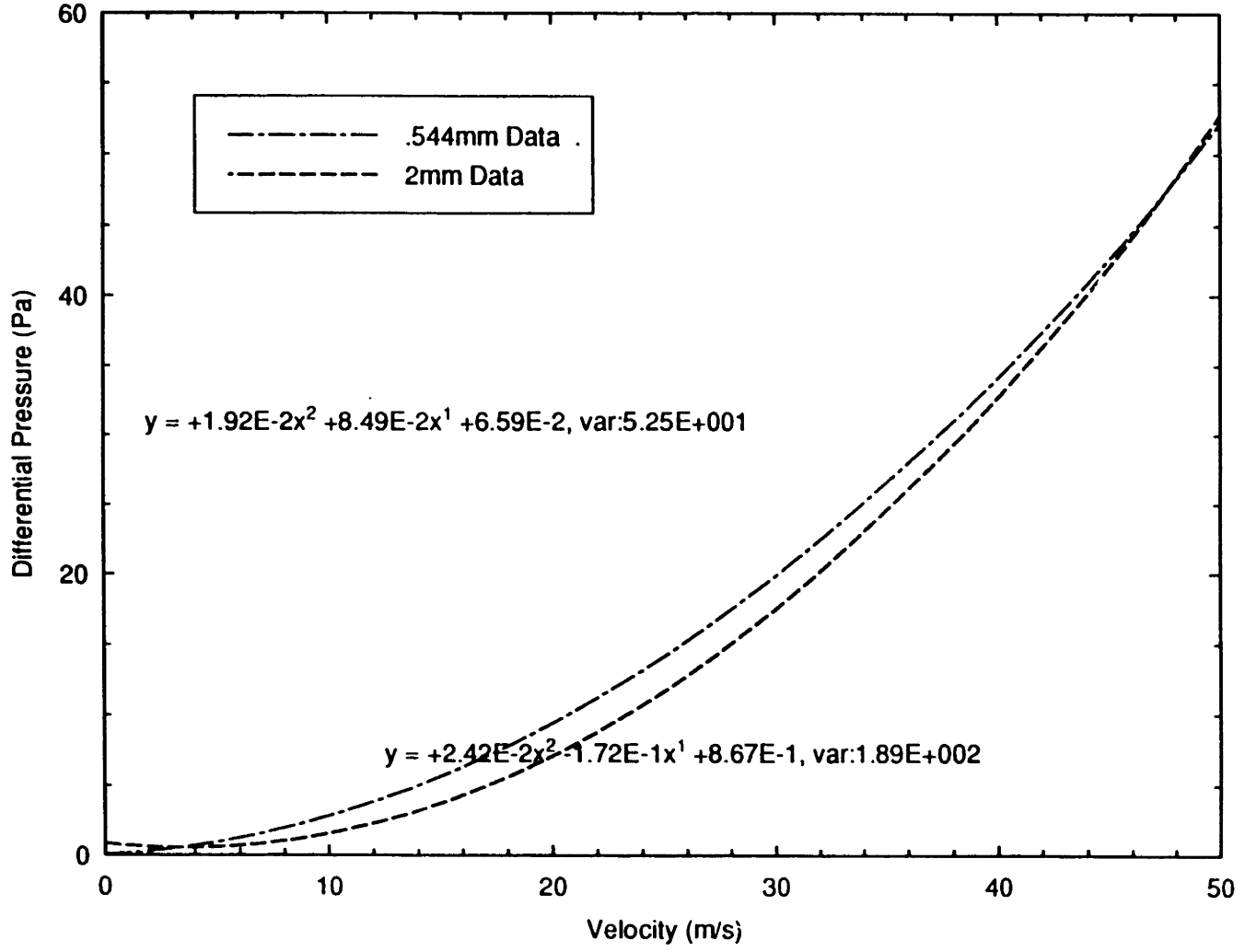

Figure 5-22: Differential Pressure Curve Fits

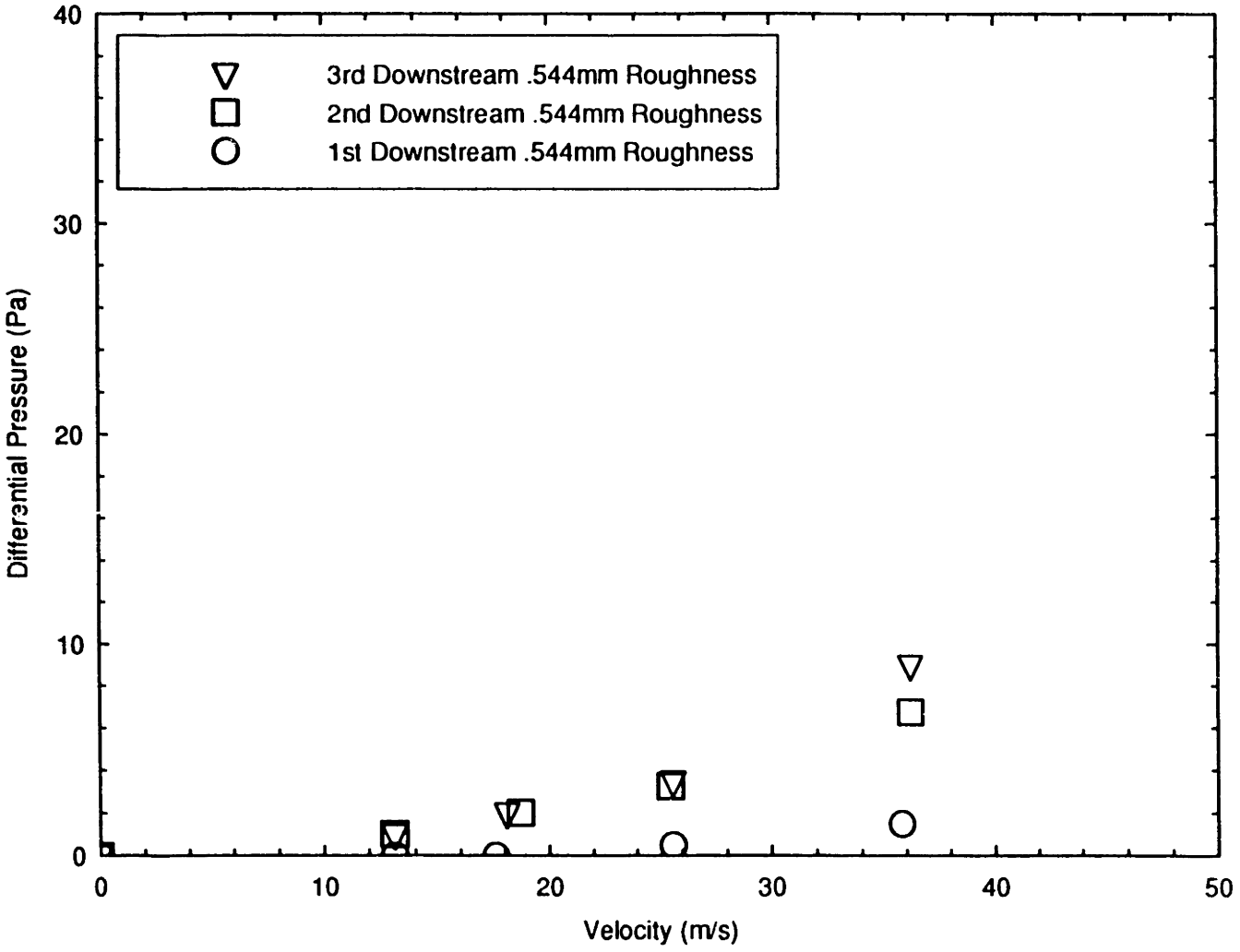

Figure 5-23: .544mm Roughness Differential Pressure Data 1L/D Downstream of Roughness

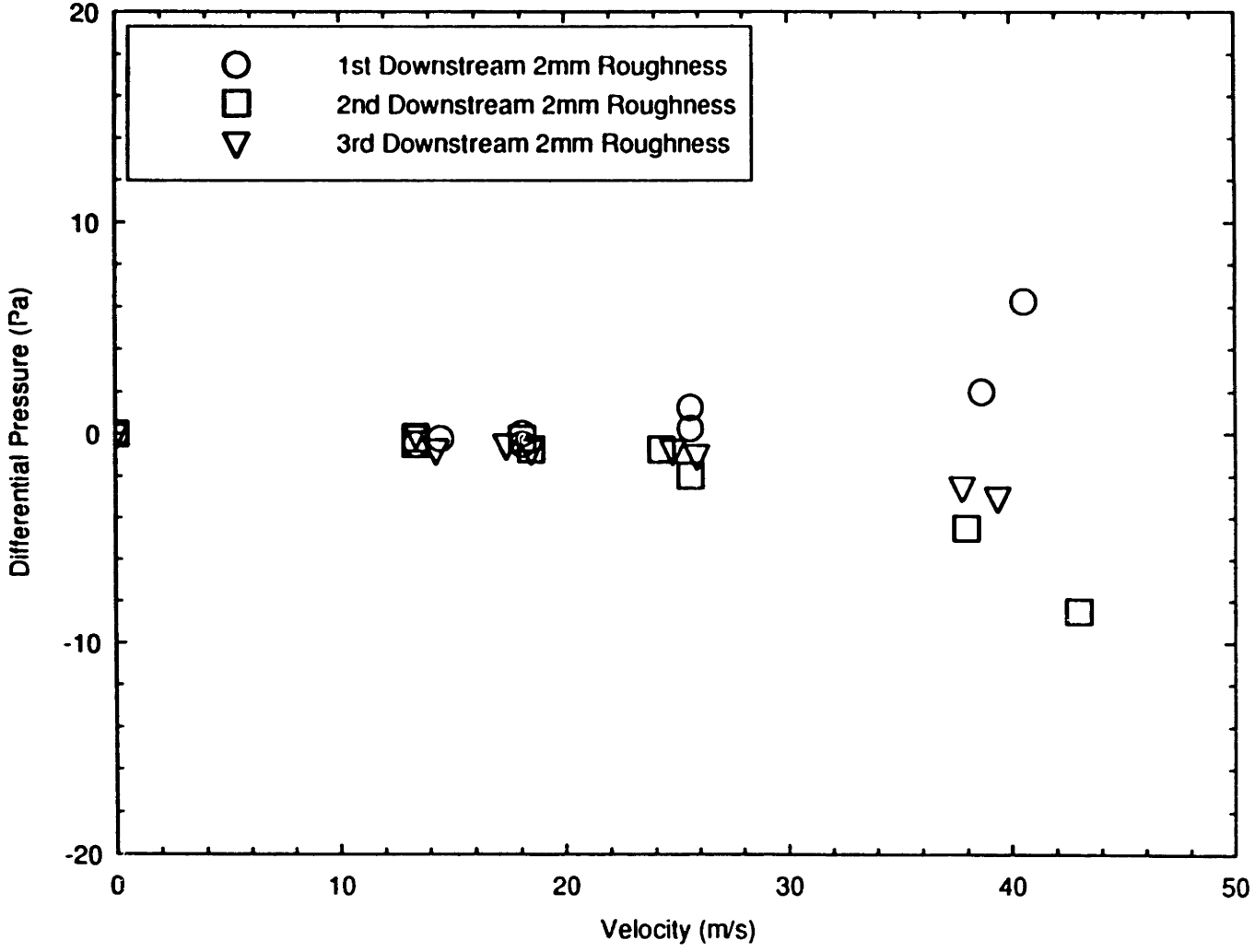

Figure 5-24: 2mm Roughness Differential Pressure Data 1L/D Downstream of Roughness

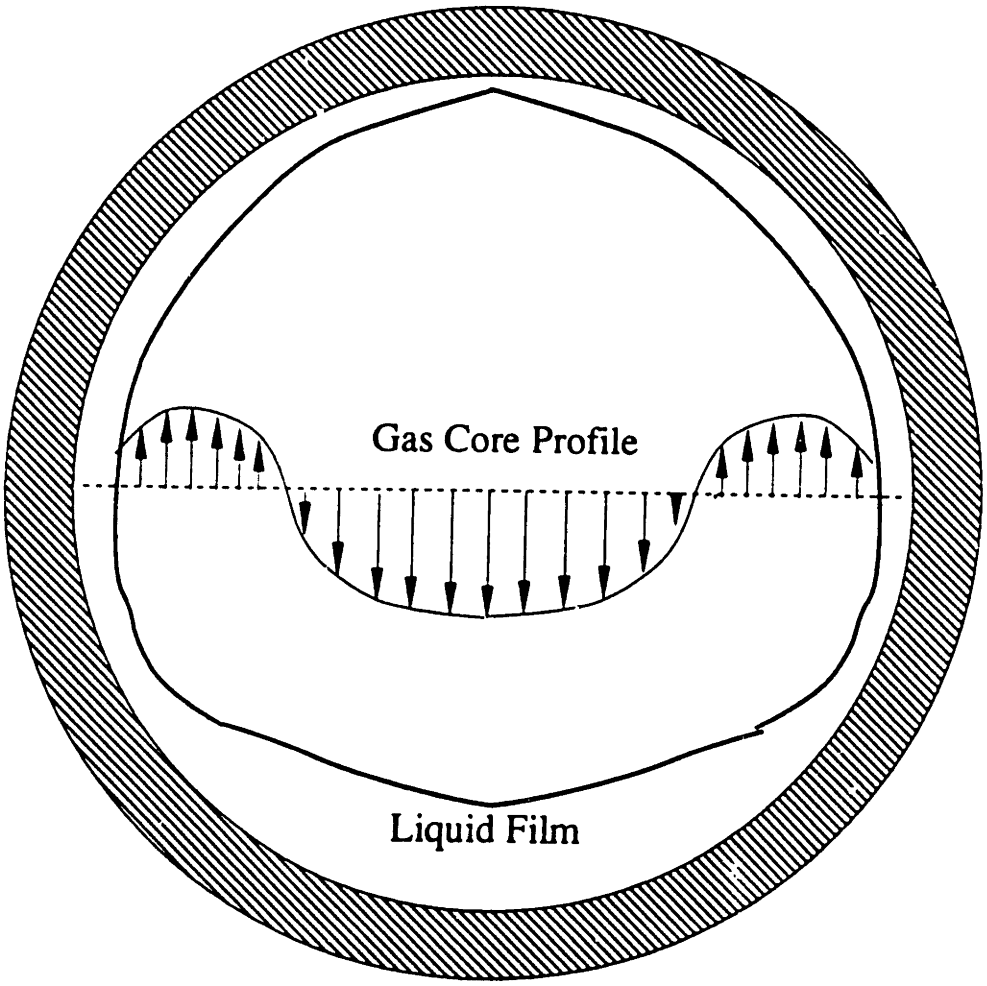

Figure 5-25: Cross-Sectional Visualization of Secondary Flow in the Gas Core

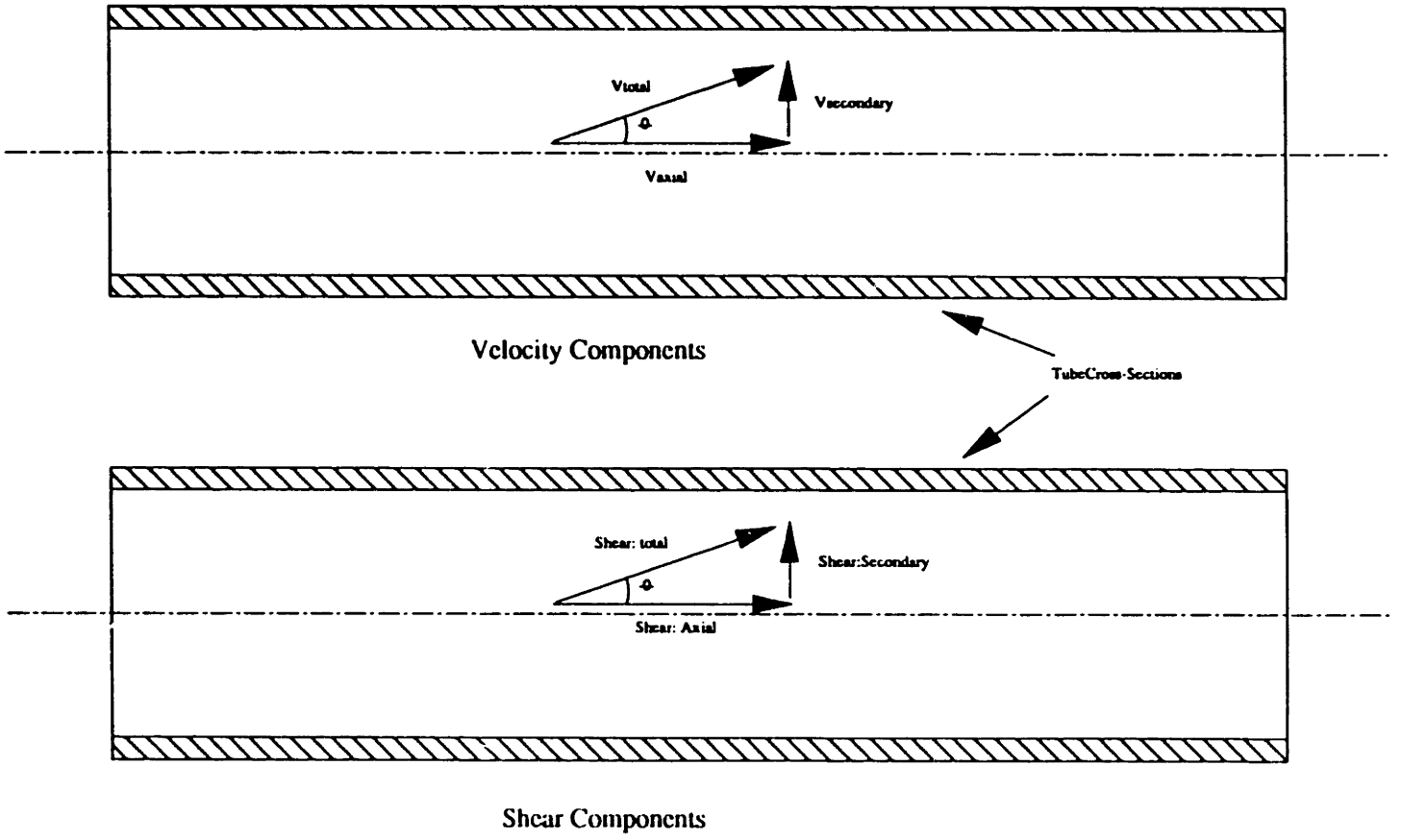

Figure 5-26: Secondary Flow, Axial Velocity, and Shear Geometrical Relationships

The pressure differential is then given by:

$$\Delta P \alpha \frac{1}{2}\rho_g V_g V_s \tag{5-9}$$

An approximate value for the secondary velocity of 4% of the axial velocity is assumed as given by the experiments of Darling and MacManus (Darling & MacManus p.159) and Crowe, Flores and Griffith (Crowe, Flores, & Griffith p.7). The resultant pressure differential from this assumption in air - water flow gives:

$$\Delta P \alpha .02 V_g^2 \tag{5-10}$$

Equation (5-10) is plotted, along with the best fit lines of the cumulative data for both roughnesses, in Figure 5- 27. The three lines fall within a few Pascals of one another. Therefore, through the averaged data an approximate magnitude and behavior of secondary flow and its resultant pressure differential has been confirmed to the preselected hypothesis.

Shape Factor Experiment

At the annular flow /stratified flow dryout boundary, the liquid at the tube's bottom forms an asymmetric shape through which the gas flows. Many have speculated that this asymmetric path may induce secondary flows in the gas phase. However, the induced secondary flows have always been assumed to be very small and consequently, neglected. An experiment was performed that displayed shape factor induced secondary flows on the same magnitude as those in the roughness experiments.

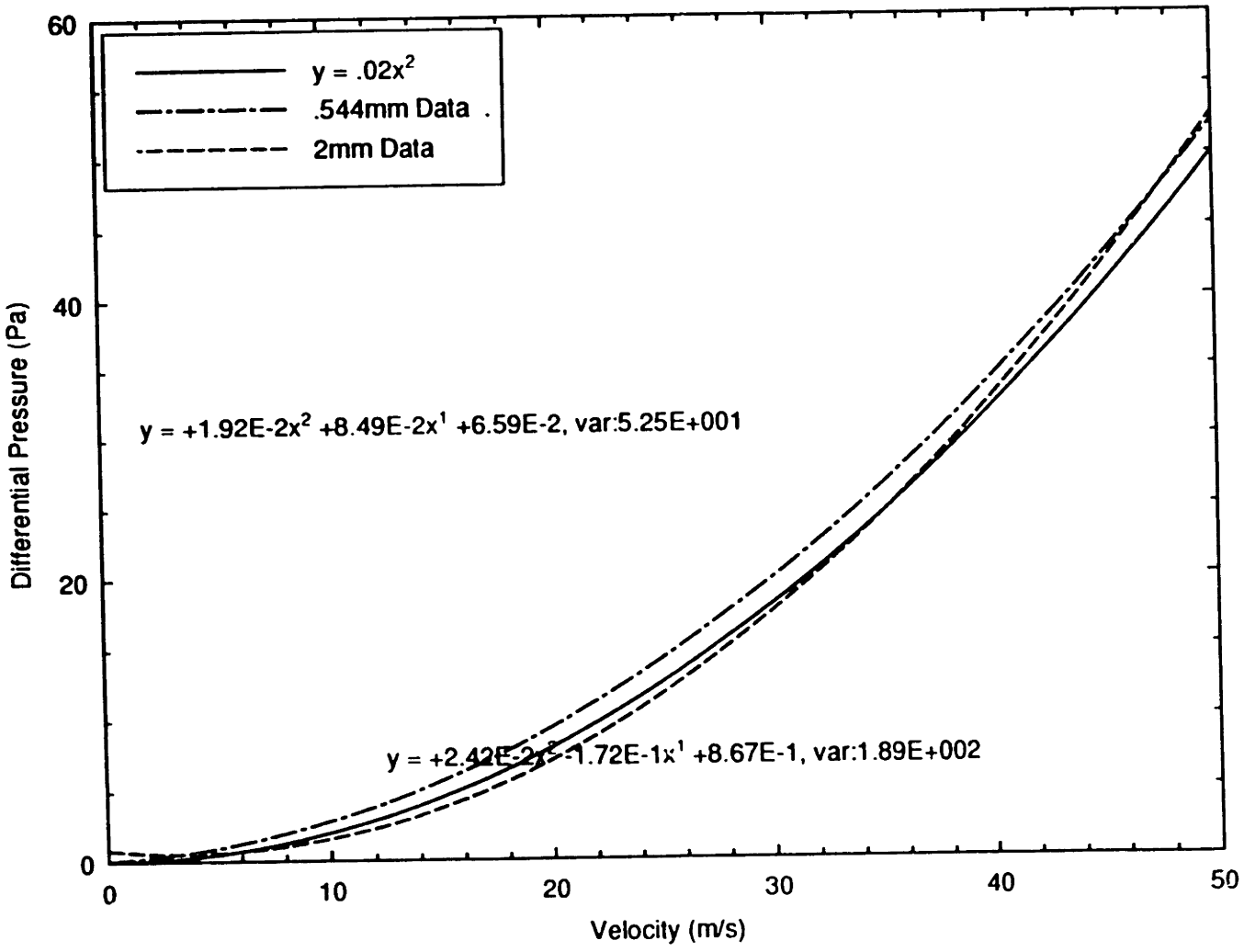

Figure 5-27: Differential Pressure Curve Fits with Theory

Film thickness dimensions in 2 in. tubes as measured by Laurinat were mimicked with molds (Laurinat p.159). Plaster of Paris was molded into the average smooth shape formed by the film distributions in air-water annular flow experiments and inserted 20 diameters into a 2 in tube (See Figure 5-5). Gas was forced through the tube over the asymmetric shape, and vortex meters were placed near the tube's exit. The angular speeds of the meters were measured as a function of axial gas velocity in the same manner as the roughness experiments.

The results of the shape factor tests are shown in Figure 5-28 . The results are also plotted along with those of the roughness tests in Figure 5-29 .

Figure 5-29 shows that the shape factor induced secondary flows are on the same order of magnitude as those created by roughness. This proves that shape factors can and do produce significant secondary flows in the gas core. Thus, when estimating secondary flow in the gas, the void fraction or amount of liquid in the tube's lower half is important. Since both roughness and shape factor vary together, what we have been calling a roughness effect might actually be a result of a combination of roughness and shape.

Entrance Effects Experiment

The entire set of secondary flow experiments have been performed at 4 feet or 20 diameters downstream of the first roughness or shape factor. To prove that the flow at those points was fully developed and not a result of entrance effects, the same type of experiments were performed at longer lengths of roughness and shape disturbance. The experiments showed that the roughness induced secondary flows remained constant with tube length while those of the shape factor completely vanished after 60 L/D's.

Two tests were performed in which 10 feet or 60 diameters of roughness or shape disturbance were used. The roughness tested was .310mm and the same shape factor was used from the previous experiment. It was hypothesized that the larger roughnesses would become fully developed faster than .310 mm which was the smallest roughness previously tested.

The results of the roughness tests are plotted in Figure 5-29 along with those found in the 20 diameter experiment while the shape factor tests produced no measurable secondary flow. The roughness induced secondary flow showed no decay or additional strength between the 20 and 60 diameter sections. This leads to the conclusion that the flow in both cases was fully developed. The shape factor, however, completely decayed by 60 diameters. This shows that the shape factor induced secondary flow is purely an entrance condition that can be created and dissipated along with new waves and shapes. It is important to note that the annular flow is in a developing state from entrance to exit in which new waves and shapes are continually generated. Therefore, shape factor and effective roughness are surely related in two-phase flows and can be defined in a single roughness term related to the liquid void fraction.

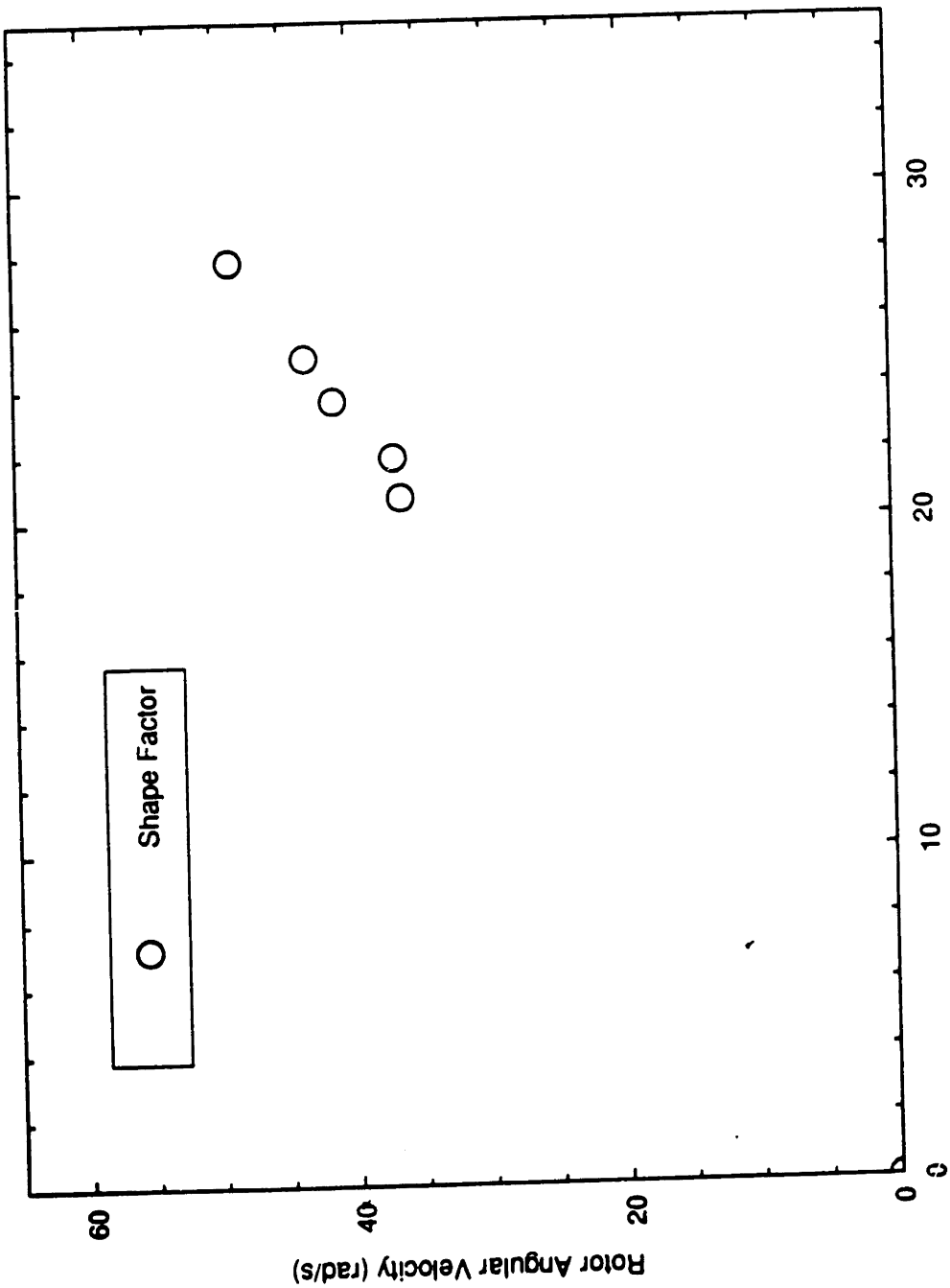

Figure 5-28: Secondary Flows Due to a Shape Factor

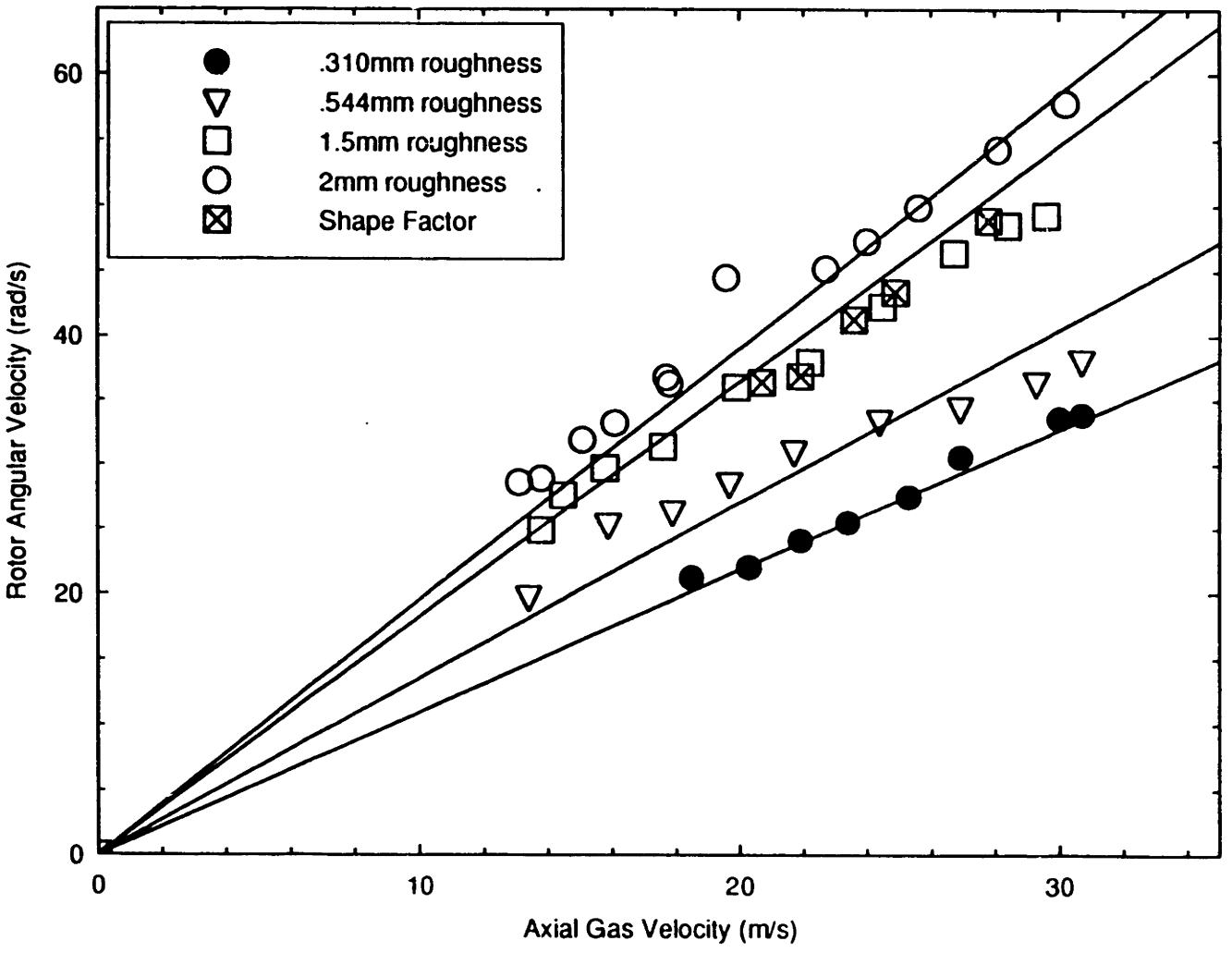

Figure 5-29: Secondary Flows Due to Shape Factors and Various Roughnesses

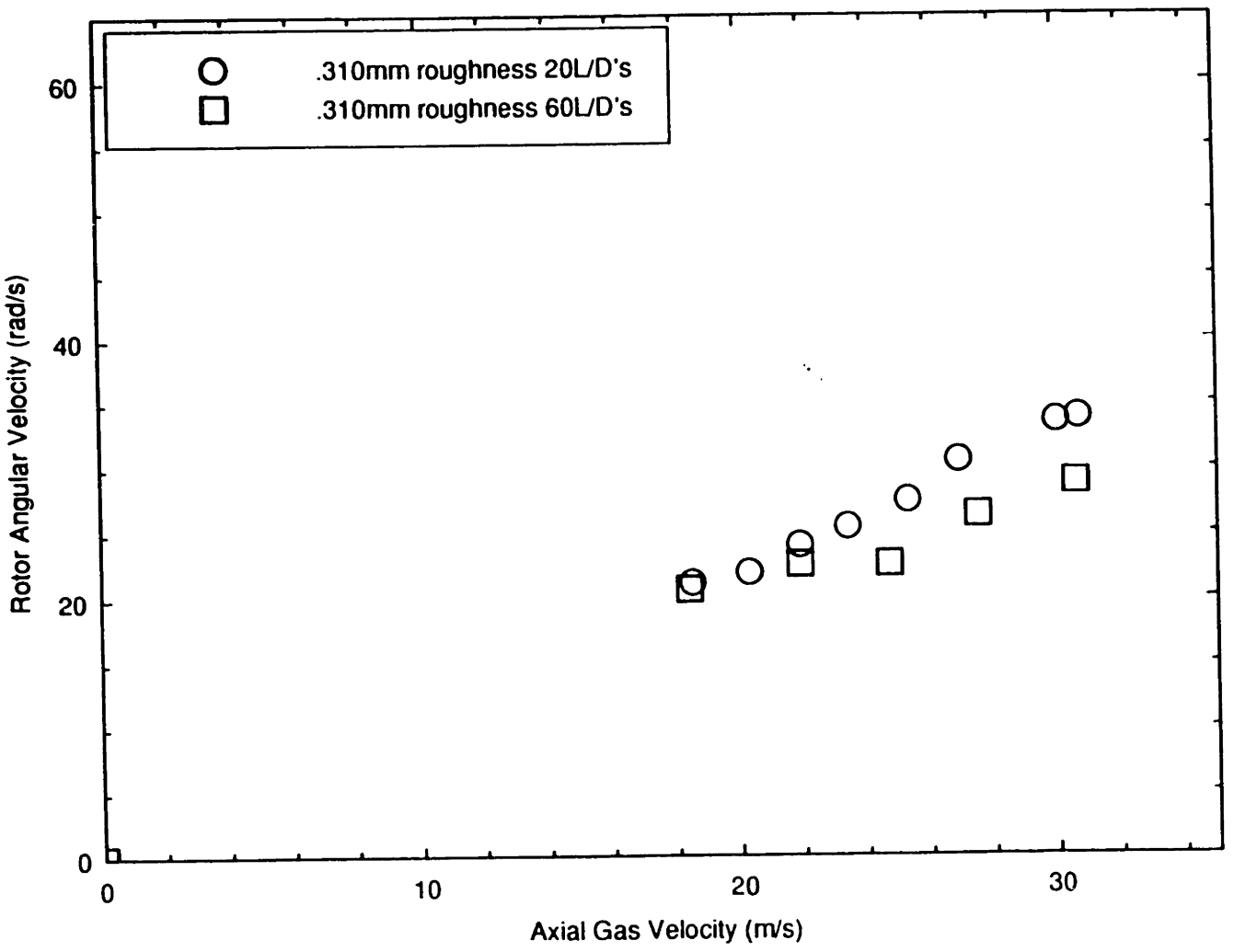

Figure 5-30: Secondary Flows caused by .310mm Roughness at 20 and 60 L/D's

Chapter 6

In chapters 1-5 the potential causes of liquid film transport up the tube's walls near the dryout boundary in horizontal annular flow were experimentally and analytically explored. From these investigations, it is apparent that the secondary velocities in the gas core constitute the only liquid transport mechanism that exists throughout the entire dryout region. Thus, between the stratified and fully wet annular flow regimes, secondary flows in the gas core are assumed to be the dominant parameter controlling dryout . In order to predict the dryout boundary in similar two-phase flows, a model must be formulated that utilizes both the proper dynamics and experimental characteristics of the secondary velocity/film transport phenomena.

Dryout Modeling Instructions

With the previously developed correlations and some analytical modeling the high quality annular dryout boundaries can be found for gas -liquid flows in horizontal tubes of approximately 2" in diameter. The modeling instructions consist of several parts. The first step includes defining the amount of shear induced by the secondary flow of the gas in a given two-phase flow situation. This secondary shear acts to force liquid up the tubes walls and ultimately controls film thickness, flowrate, and dryout. Once the secondary shear is determined, the liquid film's fluid characteristics must be modeled. The liquid film model will determine the relationship between film thicknesses, mass flowrates and the secondary shear. With the experimental dryout data from chapter 2, the critical secondary shear at dryout and the critical film thickness can then be found and are

assumed to be the limit for adiabatic flows . Knowing the magnitude of the critical secondary shear, dryout limits can be found for similar two -phase flows by substituting their respective fluid, gas, and heat transfer properties into the established model.

Secondary Shear

The secondary shears are found using both experimental data and correlations. In chapter 5 it was shown that (also see Figure 5- 25):

$$\tau_s \approx \tau_* \frac{V_s}{V_g} \quad . \tag{6-1}$$

Wallis gives a friction factor for axial interfacial shear in annular flow as (Wallis p.320):

$$C_f \approx .005(1 + 300\frac{\delta_{av}}{D}) \tag{6-2}$$

which results in an axial shear of:

$$\tau_a \approx .0025(1 + 300\frac{\delta_{av}}{D})\rho_g V_g^2. \tag{6-3}$$

Since the liquid velocities and flowrates are very small in most annular flows , the actual and superficial gas velocities are assumed to be approximately equal. Substituting eq.(6-3) into eq.(6-1) gives:

$$\tau_s \approx .0025(1 + 300\frac{\delta_{av}}{D})\rho_g V_g V_s. \tag{6-4}$$

The secondary velocity correlation developed in chapter 5 gives angular speed of the rotors vs. axial velocity and roughness. Assuming solid body rotation in the vortices,

the angular speeds of the correlation can be transformed to velocities. The conversion is performed by multiplying the angular velocity by a reasonable radius value (Gerhart & Gross p.201). The value is chosen as 1/4 the diameter of the tube, which is the largest possible vortex radius (see Figure 5-1). The secondary velocity correlation then becomes:

$$V_s \approx .268 D \rho_g^{.5} V_g \log(\frac{1000\varepsilon}{.03}). \quad (6\text{-}5)$$

In annular flows with thin films, Wallis equates roughness to approximately 4 times the circumferentially averaged film thickness changing eq.(6-5) to (Wallis p.321):

$$V_s \approx .268 D \rho_g^{.5} V_g \log(1.33 \times 10^5 D \frac{\delta_{av}}{D}). \quad (6\text{-}6)$$

Substituting eq. (6-6) back into eq.(6-4) gives:

$$\tau_s \approx 6.7 \times 10^{-4} D \rho_g^{1.5} V_g^2 (1 + 300 \frac{\delta_{av}}{D}) \log(1.33 \times 10^5 D \frac{\delta_{av}}{D}). \quad (6\text{-}7)$$

Wallis also states that for annular flows (Wallis p.320):

$$4 \frac{\delta_{av}}{D} \approx (1 - \alpha). \quad (6\text{-}8)$$

Substituting eq.(6-8) into eq.(6-7) gives:

$$\tau_s \approx 6.7 \times 10^{-4} D \rho_g^{1.5} V_g^2 [1 + 75(1 - \alpha)] \log[3.33 \times 10^4 D(1 - \alpha)]. \quad (6\text{-}9)$$

With eq.(6-9) secondary shears can be found for any set of two-phase flow parameters near the annular flow regime using the Martinelli parameter's relationship to void fraction (see Figure 6-1). The Martinelli parameter X is defined as the square root of

the fluid pressure drop divided by the air pressure drop if each phase were flowing alone in the tube (Martinelli p.39):

$$X^2 = \frac{\frac{dP_f}{dx}}{\frac{dP_g}{dx}}. \qquad (6\text{-}10)$$

In annular flow the majority of the flows are turbulent - turbulent and eq.(6-10) simplifies to (Wallis p.321):

$$X^2 = \frac{\rho_f V_f^2}{\rho_g V_g^2}. \qquad (6\text{-}11)$$

With eq.(6-11) secondary shears can be found for any set of flow parameters by looking at Figure 6-1 and matching the proper X value with the given void fraction or visa versa. An approximate equation for Figure 6-1 is given by (Wallis p.321):

$$X^2 = \frac{(1-\alpha)^2[1 + 75(1-\alpha)]}{\alpha^{5/2}}. \qquad (6\text{-}12)$$

Thus, with eq.'s (6-9), (6-11) and (6-12) the secondary shears created in two-phase flows near the annular regime can be found in closed form with the superficial gas and liquid velocities.

Liquid Film Model

When modeling the liquid film several facts must be considered. First, the secondary shear pattern and tube geometry must be modeled. Second, the type of flow must be determined, i.e. laminar or turbulent. Lastly, certain two-phase phenomena must be applied to the model such as flooding and wall shear stress limits.

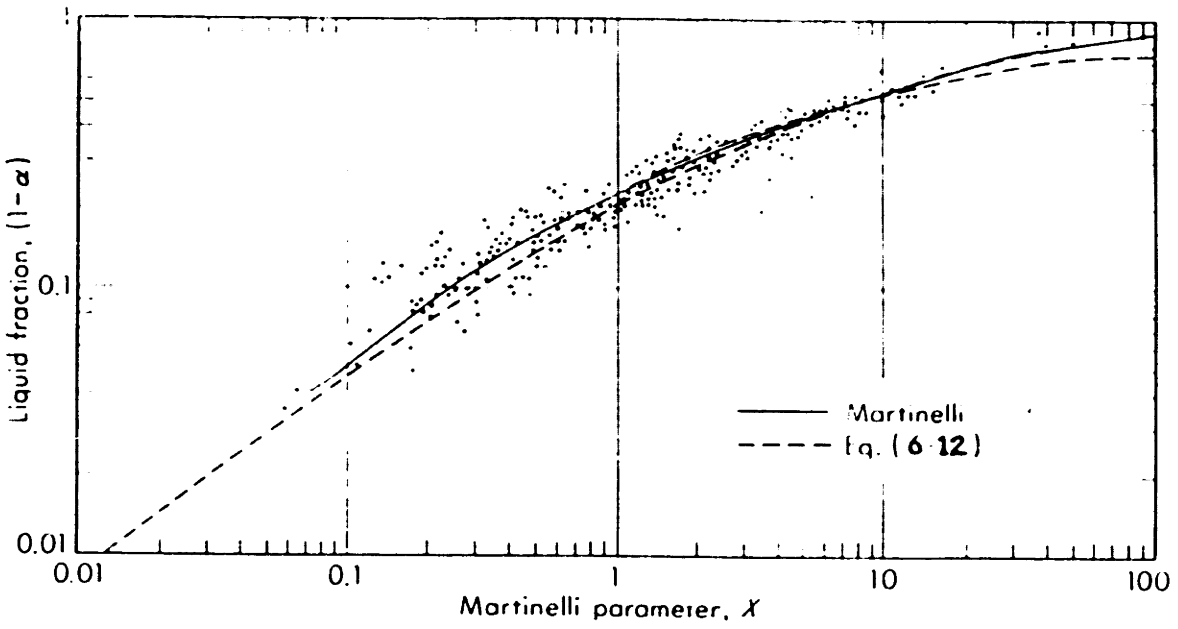

Figure 6-1: Liquid Void Fraction vs. Martinelli Parameter

Near dryout, the liquid film's thickness is assumed to be approximately equal throughout the top half of the tube. The film thickness data from Laurinat near the dryout limit verifies this assumption to within a few percent (Laurinat p.159). The data from Darling and McManus also gives that the strength of the secondary velocities and induced shears, varies with the sine of the angular position at which the bottom of the tube corresponds to 0 degrees (Darling & McManus p.161). In other words, halfway up the tube, or at 90 degrees the secondary velocity is at its greatest value. From a force balance on the liquid film, it is obvious that the force required to hold the film up the walls of the tube also varies with sine of the angular position. Thus, near the dryout limit, the decay of secondary shear and the required shear are assumed to cancel resulting in approximately the same film thicknesses throughout the upper half of the tube (see Figure 6-2). With this in mind, the film thickness model simplifies to that of the liquid film at 90 degrees (i.e. a vertical wall with gravity acting downwards and the secondary shear acting upwards) (see Figure 6-3).

The type of flow in the film is determined by the axial film flow characteristics. Due to the high gas and fluid velocities present in annular flow, the film is assumed to always meet the turbulent gas and turbulent film criteria given (Lockart & Martinelli p.42):

$$\text{Re} = \frac{VD}{\nu} \geq 2000 \text{ for one phase,}$$
$$\text{then the other phase's Re} \geq 1000. \qquad (6\text{-}13)$$

Thus, if one phase's Re number is turbulent (greater than 2000), then the other phase's critical Re number for turbulence must only be 1000.

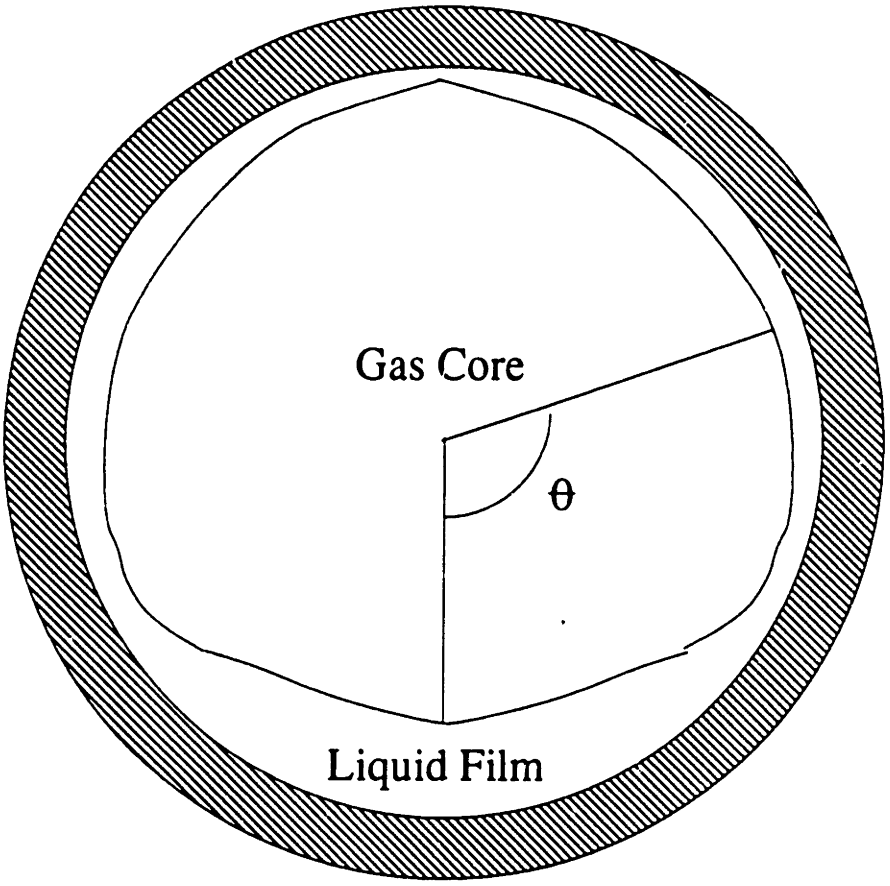

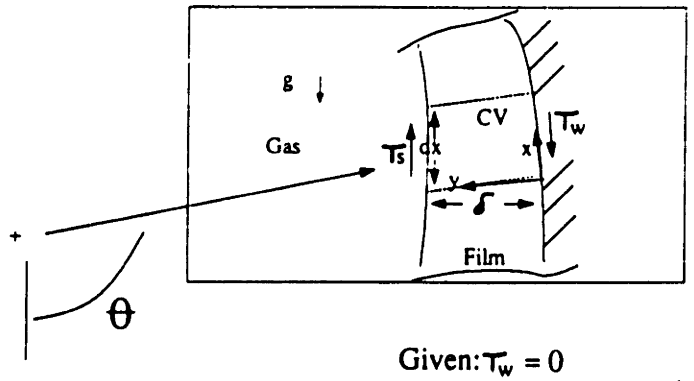

Given: $\tau_w = 0$

$\therefore \tau_s = (p_f - p_g)g\sin\theta$

Given: $\tau_s \sim \sin\theta$

$\therefore \tau_{s_{90°}} \sim (p_f - p_g)g$

Figure 6-2: Film Thickness and Secondary Shear Relationship

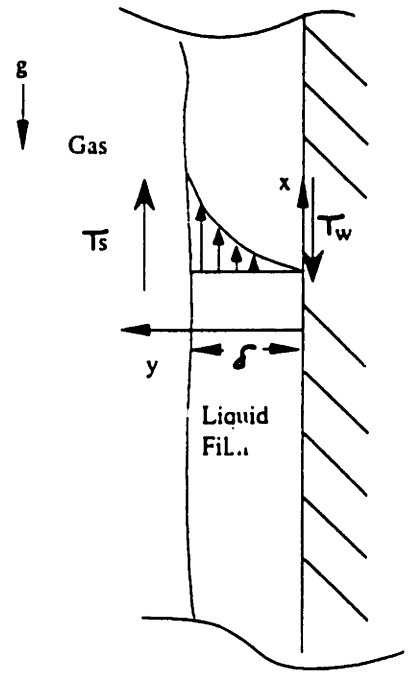

Figure 6-3: Uniform Film Thickness and Secondary Shear Relationship

Since the film is turbulent, it must have turbulent characteristics such as eddy diffusivities and a viscous sublayer near the tube's walls. The turbulent friction velocity is defined by:

$$u_* = \sqrt{\frac{\tau_w}{\rho_f}}. \tag{6-14}$$

The shears used to determine the friction velocity in the film should be taken from the axial flow in the tube since it is much greater than the shears associated with the secondary flows as given by eq.(6-1). Thus, the axial film flow determines the amount and magnitude of turbulence. In a given annular flow, the axial film flow can be assumed fully - developed with little or no significant pressure gradient . Therefore, in the axial direction the wall shear stress is equal to the interfacial shear stress on the film given by eq.(6-3). In turbulent flows near walls, the viscous sublayer is approximately 5y* thick, where y* is given by (see Figure 6-4)(Tennekes & Lumley p.160):

$$y^* = \frac{\nu_f}{u_*}. \tag{6-15}$$

Laurinat gives a film thickness in the upper half of the tube on the order of .00004m near dryout (Laurinat p.159). In an air-water flow with a gas velocity of 30 m/s and a film thickness of approximately .00004m the viscous sublayer would go out to .00009m. Thus, the entire film is approximated to be within the viscous sublayer and behaves in a statistically laminar fashion. With this in mind, the film near the dryout limit in the upper half of the tube is approximated as being within the viscous sublayer for all annular flows.

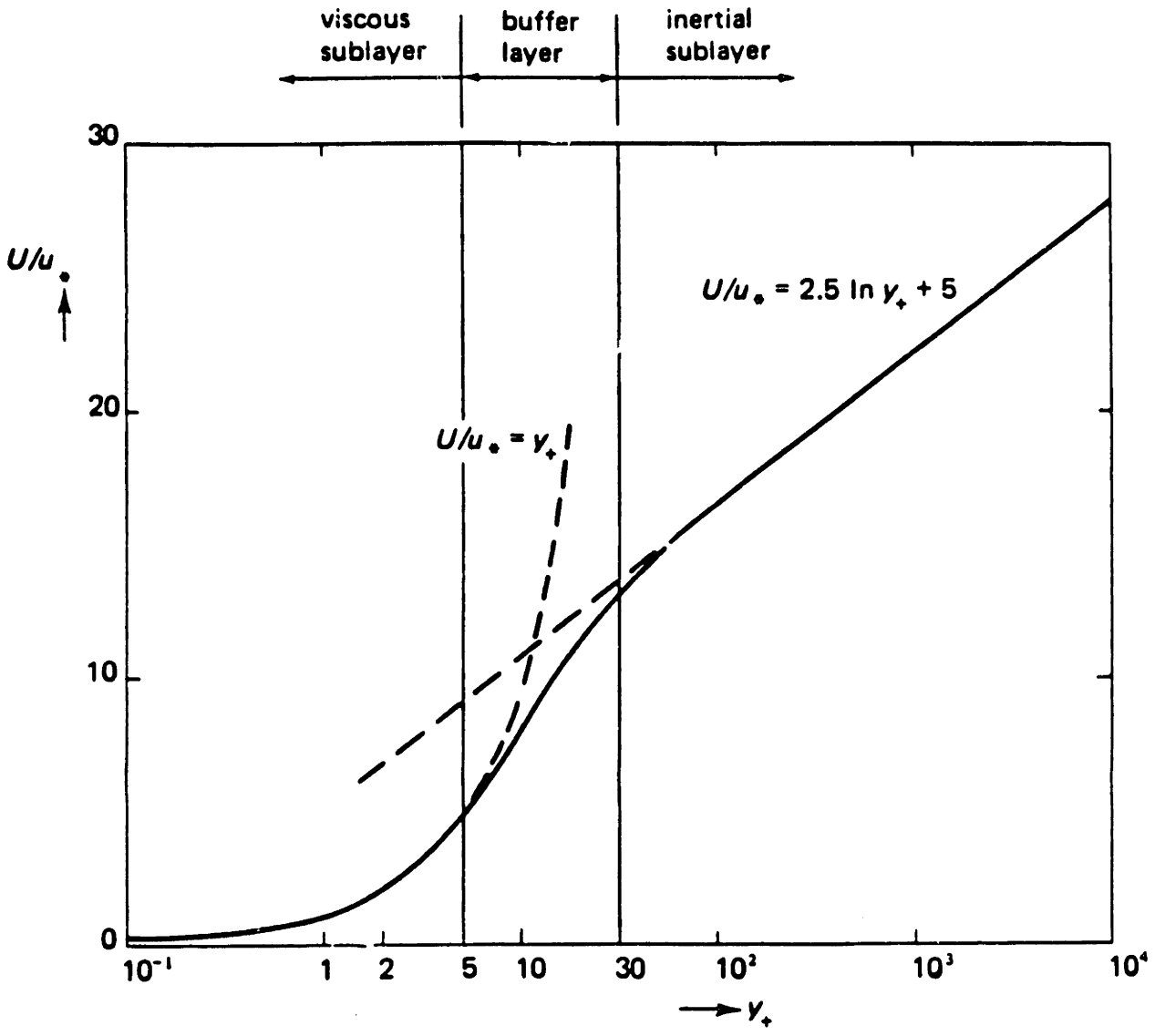

Figure 6-4: Turbulent Characteristics Near a Wall

When dealing with gravity driven films as the model in figure 6-3 displays, certain empirical facts must be taken into account. Using the analogy of film flooding in gas - liquid flows in vertical tubes, the film's velocity profile must be either all going upwards or all going downwards for a stable film thickness to exist (Hewitt & Taylor pp. 68-74). In other words, for any fluid to travel up the tube's walls in a stable fashion, the shear at the film's interface must be great enough to push the entire film upward against gravity. If fluid flows both up and down within the film, it is unstable and eventually all floods down. At the limit of a stable vertical film flowing upwards, the shear at the wall equals zero. The dryout model will use this limit to relate shears and film thicknesses.

The previous assumptions define all the variables required to model the liquid film /secondary shear relationship. Using figure 6-3 a force balance is performed on the film assuming the shear at the wall is equal to zero giving:

$$\tau_s = (\rho_f - \rho_g)g\delta \ . \qquad (6\text{-}16)$$

With the boundary conditions of no slip at the wall and zero wall shear stress, the Navier Stokes equations reduce to simple terms and result in:

$$\bar{u}(y) = \frac{(\rho_f - \rho_g)gy^2}{2\mu_f} \qquad (6\text{-}17)$$

and

$$Q' = \frac{(\rho_f - \rho_g)g\delta^3}{6\mu_f} \ . \qquad (6\text{-}18)$$

The model describing the film displays a net mass flux up the sides of the tube near the dryout boundary in adiabatic systems. This net mass flux in the film could account for a certain robustness of the dryout limit with respect to a range of heat fluxes in two-phase flows involving heat transfer. In other words, there may exist in the film an abundance of

net mass flux up the walls of the tube to account for the amount of liquid being evaporated into vapor. Since the flow is assumed to be fully -developed, the net mass flux in the film traveling up the tube's walls must either collect at the tube's top and drop down due to gravity into the liquid in the tube's bottom, be entrained in the gas core, or evaporate due to the boiling and heat transfer in the upper half of the tube.

Dryout Limit

With the previously described model and secondary shear correlation, the air-water dryout data from chapter 2 can be used to find a critical secondary shear and film thickness associated with dryout in adiabatic systems. Superficial gas and fluid velocities equal to 30 m/s and .018 m/s respectively, are arbitrarily chosen from the dryout points of chapter 2. Using eq.(6-11) gives a Martinelli parameter value of .019 which corresponds to a liquid void fraction of .015 (see Figure 6-1). Substituting the liquid void fraction into eq.(6-9) results in a critical shear of .11Pa. The corresponding film thickness in the upper half of the tube is equal to .00001m using eq.(6-16). It is interesting to note that this value is on the order of the film thicknesses measured by Laurinat just preceding dryout in the same flow situation (Luarinat p.159). Setting the critical shear value equal to .11Pa and solving eq.(6-9) for all the possible superficial gas and liquid velocities displays the correlated dryout boundary between the stratified and annular flow regimes. This boundary is plotted along with the actual air-water dryout points in Figure 6-5. The critical film thickness of .00001m is taken as the universal limit for adiabatic two-phase flows in 2" pipes. The boundaries are almost identical and give validity to the model's behavior.

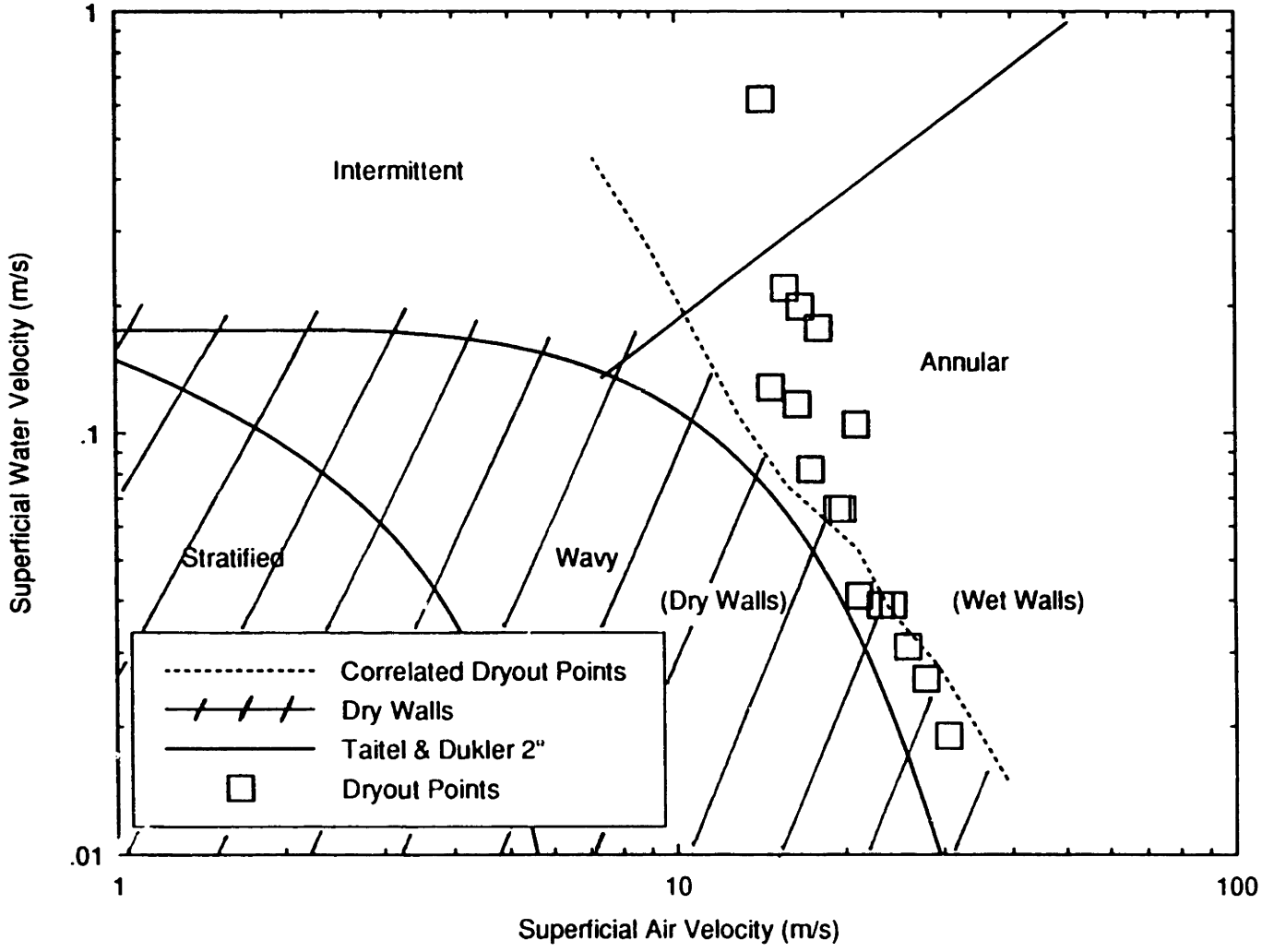

Figure 6-5: Adiabatic Air-Water Experimental and Correlated Dryout Boundaries

The model can also be used to find dryout boundaries in similar systems where heat transfer exists. At dryout in systems with heat transfer, it is assumed that the liquid film's mass flux up the sides of the tube's walls given by eq.(6-18) is evaporated into vapor to account for the heat flux in the upper half of the tube (see Figure 6-6).The relationship between heat flux and the critical Q' is given by:

$$Q' = \frac{q' \pi D}{4 \rho_f h_{fg}} \tag{6-19}$$

The critical film thickness and secondary shears then become:

$$\delta = \left(\frac{3q' \pi D \mu_f}{2 \rho_f h_{fg} (\rho_f - \rho_g) g}\right)^{1/3} \tag{6-20}$$

and

$$\tau_s = (\rho_f - \rho_g)^{2/3} \left(\frac{3q' \pi D \mu_f}{2 \rho_f h_{fg} g}\right)^{1/3} \tag{6-21}$$

Using the critical secondary shear from eq.(6-21), the dryout boundary's gas and fluid superficial velocities can be found from eq.(6-9).

The dryout data of Crowe (1992) of steam - water flows at atmospheric pressure in .057m diameter tubes displays little variation in the dryout boundary due to differences in heat flux (see Figure 6-7). Since mass flux or Q' varies with the cube of secondary shear and critical film thickness, this behavior also tends to verify the model's behavior. Thus, a change in required film mass flux due to different heat fluxes would result in a very small critical film thickness variation, and the resulting dryout boundaries would only slightly differ from one another. Crowe's experimental heat flux values fell in the range of 30-150 kw/m^2. Although this independence of heat flux behavior will change at

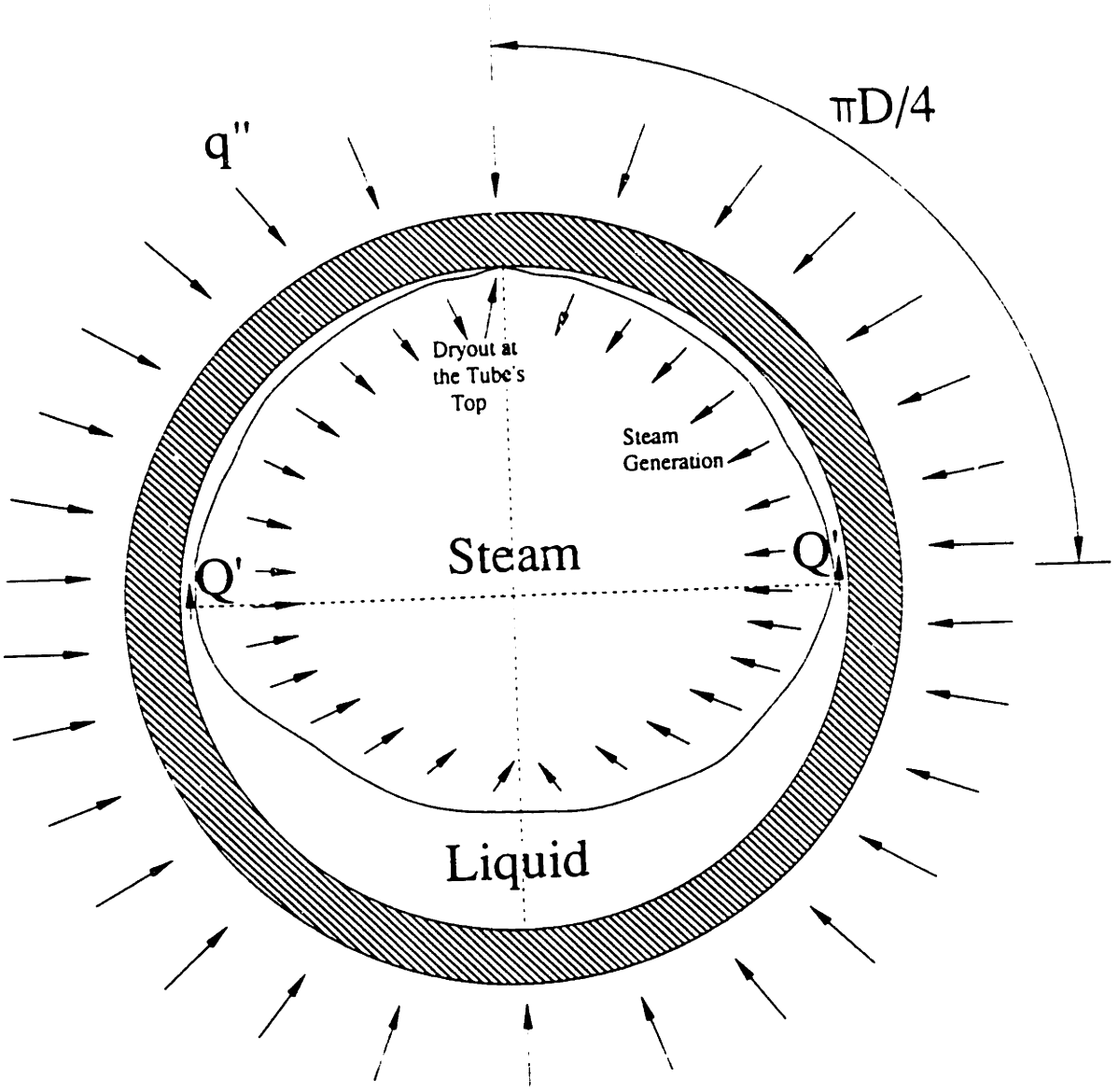

Figure 6-6: Heat Transfer and Liquid Film Relationship

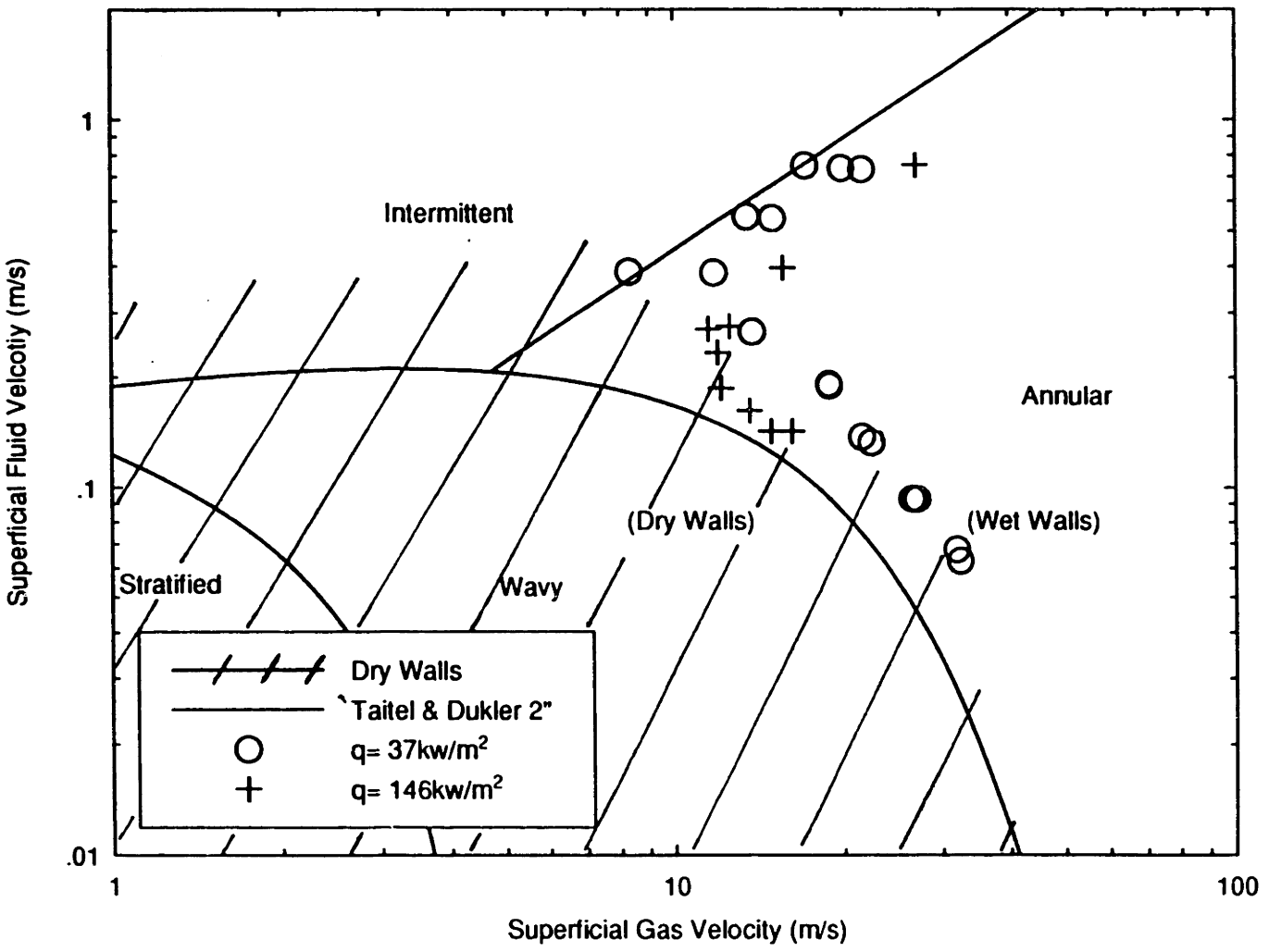

Figure 6-7: Steam-Water Dryout Data at 1Atm. for Various Heat Fluxes

extremely high heat fluxes, most designs of boilers, and heat exchangers also fall in the 30-150 kW/m^2 heat flux range. Solving for the required secondary shears and dryout boundaries for the experimental system properties of Figure 6-7, the model and experimental dryout boundaries can be compared (see Figure 6-8). The actual and correlated boundaries basically lie on the same line again proving the validity of the correlation.

To further investigate the correlation's behavior, a simple analysis was performed. The dryout correlation in essence takes a "snapshot" of the system at given flowrates. If it was assumed that the flowrates were moderately different, the correlation would result in slightly different secondary shears. For instance, in a flow with heat transfer, just preceding dryout in a wet tube, the system would contain greater fluid and less gas flowrates than at the dryout limit. However, the secondary shears should be greater than that at the dryout limit because the tubes walls contain a liquid film. Consequently, for values of 5% less gas flowrate and the corresponding addition in liquid flowrate associated with adiabatic dryout points, the secondary shears were found. The average value was approximately .14Pa or 18% greater than the dryout secondary shear. The correlation, therefore, behaves in conjunction with both two-phase flow theory and heat transfer considerations.

Specific Modeling Instructions

The dryout boundary can be found using the following modeling scheme:

Step 1) Determine the critical film thickness:

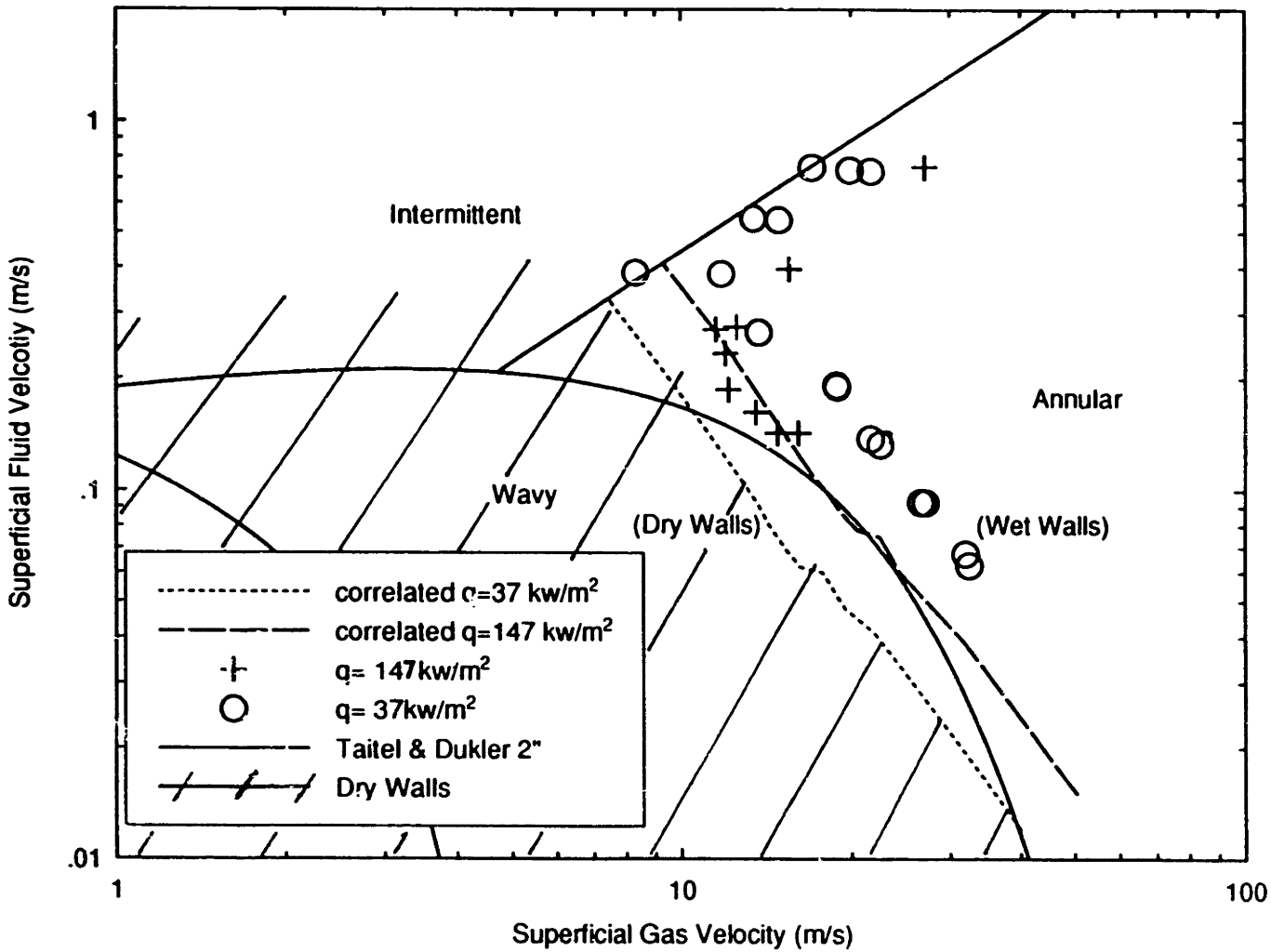

Figure 6-8: Steam -Water Experimental and Correlated Dryout Points at 1 Atm for Various Heat Fluxes

a) In a system with no heat transfer, use the critical film thickness of .00001m.

b) If the system has heat flux find the critical film thickness with eq.(6-20) and the system properties. Use the critical film thickness if it is greater than .00001m. Take .00001m as the critical film thickness if the value from eq.(6-20) is smaller than .00001m.

Step 2) With the critical film thicknesses found in Step 1 determine a critical shear with eq.(6-16).

Step 3) Knowing the critical shear from step 2, solve for gas velocity vs. void fraction using eq(6-9).

Step 4) Take a void fraction value from step 3 and find the corresponding Martinelli Parameter (X) with Figure 6-1 or eq(6-12). With the gas velocity corresponding to the void fraction from step 3 and the Martinelli Parameter from step 4, solve eq.(6-11) for the fluid velocity. The fluid and gas velocities developed through this process define a dryout boundary point. Continue this process for a wide range of void fraction/gas velocity combinations from step 3 to define the entire boundary.

Chapter 7

Conclusion

The experimental and analytical investigations in this thesis proved many new insights regarding the cause of the annular/stratified flow regime dryout boundary and liquid film transport in high quality, annular flows in horizontal tubes. Several potential mechanisms related to film transport in annular flow were investigated both experimentally and analytically in order to find the most dominant near dryout. The major results of this study are as follows:

- The secondary flows in the gas core were the dominant mechanism controlling film thickness and transport near dryout. These secondary flows consisted of two counter-rotating vorticies that sheared a liquid film up the walls of the tube.

- The magnitude of the secondary flows were found to be driven by the circumferential variation of effective roughness in the liquid film at each cross-section of the tube.

- The mechanisms of entrainment and deposition, wave spreading, and wave pumping were not found to be significant contributors to the transport of liquid on the wall to the upper half of the tube where dryout first appears.

- Direct measurements of the swirl in the flow and pressure differences between the top and bottom of the tube confirm the presence of the two counter -rotating vorticies.

- The mechanism of this secondary flow is proposed and used to determine its magnitude. This mechanism is also present in any non-circular passage passing a two-phase flow and helps to account for liquid film thickness variations around the tube.

References

1) Butterworth, D.," Air - Water, Annular Flow in a Horizontal Tube", *Progress in Heat and Mass Transfer*, 6, 235, 1972.

2) Butterworth, D., and D. J. Pulling, " A Visual Study of Mechanisms in Horizontal Annular, Air-Water Flow", *Atomic Energy Research Establishment*, 1972.

3) Collier, John G., *Convective Boiling and Condensation*, New York, McGraw-Hill, 1972.

4) Crowe, Keith E., Ph.D. Thesis, MIT, Cambidge, Ma, 1992.

5) Crowe, Keith E., Aaron Flores, and Peter Griffith," Dryout Limits in Two-Phase Flow in Heated Horizontal Pipes", *Proceedings of the Ninth Symposium on Energy Engineering Sciences*, 1991.

6) Darling, R.S., and McManus, H.N.," Flow Patterns in Circular Ducts with Circumferential Variation of Roughness: A Two-Phase Analog", *Developments in Mechanics*, Vol. 5, pp. 153-170, 1969.

7) Fukano, T., and A. Ousaka," Prediction of the Circumferential Distribution of Film Thickness in Horizontal and Near-Horizontal Gas-Liquid Flows", *Int. J. Multiphase Flow*, Vol. 15, No. 3, pp. 403-419, 1989.

8) Gerhart, Philip M., and Richard J. Gross, *Fundamentals of Fluid Mechanics*, Reading, Ma., 1985.

9) Hewitt, G. F., S. Jayanti, and S.P. White," Time-Dependent Behavior of the Liquid Film in Horizontal Annular Flow", *Int. J. Multiphase Flow*, Vol. 16, No. 6, pp. 1097-1116, 1990.

10) Hewitt, G.F., and N.S. Hall Taylor, *Annular Two-Phase Flow*, New York, Pergamon Press, 1970.

11) Laurinat, James Edwin," Studies of the Effects of Pipe Size on Horizontal Annular Two-Phase Flows", Ph.D. Thesis, University of Illinois at Urbana-Champaign, 1982.

12) Lockhart, R. W., and R. C. Martinelli, "Proposed Correlation of Data for Isothermal Two-Phase, Two-Component Flow in Pipes", *Chem. Eng. Progress*, Vol. 45, p.39, 1949.

13) Lumley, J. L., and H. Tennekes, *A First Course in Turbulence*, Cambridge, Ma. MIT Press, 1972.

14) Malkin, S., *Grinding Technology: Theory and Applications of Machining with Abrasives*, New York, Halsted Press, 1989.

15) Mandhane, J. M., G. A. Gregory, and K. Aziz," A Flow Pattern Map for Gas-Liquid Flow in Horizontal Pipes", *Int. J. Multiphase Flow*, 3, p.537, 1974.

16) Pitts, Donald R., and Leighton E. Sissom, *Heat Transfer*, New York, McGraw-Hill, Inc., 1977.

17) Steen, D. A., M.S. Thesis, Dartmouth College, Hanover, N.H., 1964.

18) Taitel, y., and A.E. Dukler," A Model for Predicting Flow Regime Transitions in Horizontal and Near Horizontal Gas-Liquid Flow", *A.I.Ch.E.J.*, 22(1), 47, 1976.

19) Wallis, Graham B., *One-Dimensional Two-Phase Flow*, New York, McGraw-Hill, 1969.